

12-2012

# Plasmonic and Photonic Designs for Light Trapping in Thin Film Solar Cells

Liming Ji

*University of Arkansas, Fayetteville*

Follow this and additional works at: <http://scholarworks.uark.edu/etd>



Part of the [Electromagnetics and Photonics Commons](#), and the [Plasma and Beam Physics Commons](#)

---

## Recommended Citation

Ji, Liming, "Plasmonic and Photonic Designs for Light Trapping in Thin Film Solar Cells" (2012). *Theses and Dissertations*. 587.  
<http://scholarworks.uark.edu/etd/587>

This Dissertation is brought to you for free and open access by ScholarWorks@UARK. It has been accepted for inclusion in Theses and Dissertations by an authorized administrator of ScholarWorks@UARK. For more information, please contact [scholar@uark.edu](mailto:scholar@uark.edu), [ccmiddle@uark.edu](mailto:ccmiddle@uark.edu).

PLASMONIC AND PHOTONIC DESIGNS FOR LIGHT TRAPPING IN THIN FILM SOLAR  
CELLS

PLASMONIC AND PHOTONIC DESIGNS FOR LIGHT TRAPPING IN THIN FILM SOLAR  
CELLS

A dissertation submitted in partial fulfillment  
of the requirements for the degree of  
Doctor of Philosophy in Electrical Engineering

By

Liming Ji  
Nanjing University of Science and Technology  
Bachelor of Science in Electrical Engineering, 2007

December 2012  
University of Arkansas

## **ABSTRACT**

Thin film solar cells are promising to realize cheap solar energy. Compared to conventional wafer cells, they can reduce the use of semiconductor material by 90%. The efficiency of thin film solar cells, however, is limited due to insufficient light absorption. Sufficient light absorption at the bandgap of semiconductor requires a light path more than 10x the thickness of the semiconductor. Advanced designs for light trapping are necessary for solar cells to absorb sufficient light within a limited volume of semiconductor. The goal is to convert the incident light into a trapped mode in the semiconductor layer.

In this dissertation, a critical review of currently used methods for light trapping in solar cells is presented. The disadvantage of each design is pointed out including insufficient enhancement, undesired optical loss and undesired loss in carrier transport. The focus of the dissertation is light trapping by plasmonic and photonic structures in thin film Si solar cells. The performance of light trapping by plasmonic structures is dependent on the efficiency of photon radiation from plasmonic structures. The theory of antenna radiation is used to study the radiation by plasmonic structures. In order to achieve efficient photon radiation at a plasmonic resonance, a proper distribution of surface charges is necessary.

The planar fishnet structure is proposed as a substitution for plasmonic particles. Large particles are required in order to resonate at the bandgap of semiconductor material. Hence, the resulting overall thickness of solar cells with large particles is large. Instead, the resonance of fishnet structure can be tuned without affecting the overall cell thickness. Numerical simulation shows that the enhancement of light absorption in the active layer is over 10x compared to the same cell without fishnet. Photons radiated from the resonating fishnet structure travel in multiple



directions within the semiconductor layer. There is enhanced field localization due to interference. The short circuit current was enhanced by 13.29%.

Photonic structures such as nanodomes and gratings are studied. Compared to existing designs, photonic structures studied in this dissertation exhibited further improvements in light absorption and carrier transport. The nanodome geometry was combined with conductive charge collectors in order to perform simultaneous enhancement in optics and carrier transport. Despite the increased volume of semiconductor material, the collection length for carriers is less than the diffusion length for minority carriers. The nanodome geometry can be used in the back end and the front end of solar cells. A blazed grating structure made of transparent conductive oxide serves as the back passivation layer while enhancing light absorption. The surface area of the absorber is increased by only 15%, indicating a limited increase in surface recombination. The resulting short circuit current is enhanced by over 20%.

The designs presented in the dissertation have demonstrated enhancement in Si thin film solar cells. The enhancement is achieved without hurting carrier transport in solar cells. As a result, the enhancement in light absorption can efficiently convert to the enhancement in cell efficiency. The fabrication of the proposed designs in this dissertation involves expensive process such as electron beam lithography. Future work is focused on optical designs that are feasible for cheap fabrication process. The designs studied in this dissertation can serve as prototype designs for future work.

This dissertation is approved for recommendation  
to the Graduate Council.

Dissertation Director:

---

Dr. Vasundara V. Varadan

Dissertation Committee:

---

Dr. Samir El-Ghazaly

---

Dr. Hameed Naseem

---

Dr. Reeta Vyas

---

Dr. Shui-Qing Yu

**DISSERTATION DUPLICATION RELEASE**

I hereby authorize the University of Arkansas Libraries to duplicate this dissertation when needed for research and/or scholarship.

**Agreed** \_\_\_\_\_

Liming Ji

**Refused** \_\_\_\_\_

Liming Ji

## **ACKNOWLEDGEMENTS**

I would like to acknowledge Dr. Vasundara V. Varadan for her mentorship and support through my Ph. D. study.

I would like to thank Prof. Shui-Qing Yu, Prof. Hameed Naseem, Prof. Reeta Vyas and Prof. Samir El-Ghazaly for taking their precious time serving in my committee.

I would like to thank Prof. Stephen J. Fonash and Dr. Wook Jun Nam of Pennsylvania State University for their help during our collaboration.

I would like to appreciate all the help from my colleagues, especially Dr. In Kwang Kim, Mr. Michael Brandon Buscher, Dr. Tarek Said, Mr. Binh Tran, Mr. Atanu Dutta, Mr. Sayan Seal and Dr. Vinay Budhraj.

The work in this dissertation is in part supported by the National Science Foundation under EPS–1003970. The numerical simulation work is also in part supported by the National Science Foundation under Grants ARI # 0963249, MRI #0959124 (Razor), EPS #0918970 (CI TRAIN), and a grant from the Arkansas Science and Technology Authority, managed by the Arkansas High Performance Computing Center.

## **DEDICATION**

The Ph. D. degree is dedicated to my wife Chen Yue and my parents Zengchi Ji and Guixi Zhang, who have kept giving me priceless support all the way through my education.

## TABLE OF CONTENTS

I. Introduction .....	1
1.1 Thin Film Photovoltaics .....	1
1.2 Light Trapping in Thin Film Solar Cells.....	4
II. A Review of Methods for Light Trapping .....	9
2.1 Background .....	9
2.2 Light Trapping by Rough Surfaces .....	9
2.3 Light Trapping by Plasmonic Particles .....	12
2.4 Light Trapping by Nanodome and Nanowire Geometry .....	19
2.5 Summary .....	21
III. Transmission Line Theory for Thickness Optimization of Anti-Reflection Coatings .....	23
3.1 Background .....	23
3.2 Transmission Line Theory for Thin Film Solar Cells.....	26
3.3 Optimization of the Anti-Reflection Layer .....	30
IV. Radiation by Plasmonic Structures .....	34
4.1 Plasmonic Structures and Antennas .....	34
4.2 Radiation by Plasmonic Particles .....	36
4.3 Particle Array and Near Field Coupling.....	40
4.4 Plasmonic Particles on Top of Solar Cells .....	45
V. Fishnet Structures for Enhancing Light Absorption in Solar Cells .....	48
5.1 Background .....	48
5.2 Design of Fishnet for a-Si:H Thin Film Solar Cells .....	54
5.3 Light Absorption Enhancement by Fishnet.....	56

VI. Temperature Dependence of Plasmonic Resonances .....	62
6.1 Background .....	62
6.2 Metamaterial Samples .....	65
6.3 Experimental Set-up and Verification.....	68
6.4 High Temperature Characterization of Material Samples.....	74
6.5 Theoretical Explanation of the Observed Temperature Behavior of Metamaterials .....	82
6.6 Comparison of Full Wave Simulation with Observed Data.....	88
6.7 Future Work .....	90
VII. Light Trapping by Nanodome Geometry .....	91
7.1 Background .....	91
7.2 Design and Fabrication.....	91
7.3 Numerical Study.....	96
7.4 Nanodomains for Thin Film Solar Cells on Substrate .....	98
VIII. Blazed Grating for Light Trapping in Thin Film Solar Cells .....	110
8.1 Background .....	110
8.2 Design of 1D Gratings in Thin Film Solar Cells.....	111
8.3 Fabrication of the Grating Structure.....	112
8.4 Results and Discussions .....	114
8.5 2D Blazed Grating.....	121
IX. Conclusions.....	124
List of References .....	127
Appendix.....	133

## LIST OF TABLES

Table 5.1 The calculated short circuit current .....	60
Table 6.1 The permittivity of substrate at 10GHz .....	64
Table 6.2 SRR Orientations and Dimension for FR4 Based Samples .....	66
Table 6.3 Mechanical and Thermal Properties of Silver and DuPont 951 .....	87
Table 6.4 Shift in Resonance Frequency Due to Each Factor (20°C to 400°C) .....	89



## LIST OF FIGURES

Figure 1.1 The cost breakdown of Si wafer solar panels.....	1
Figure 1.2 The pie plot showing the market share of each PV technology in 2010 .....	2
Figure 1.3 The comparison of the imaginary part of permittivity of a-Si and c-Si.. .....	3
Figure 1.4 The required length of light path at each wavelength in order to achieve 90% of light absorption within a-Si.....	5
Figure 1.5 (a) Light transmits through a semiconductor layer without any back reflection; (b) The incident light is reflected by the rear reflector.....	6
Figure 1.6 The schematic showing rays within an absorber.....	7
Figure 2.1 A schematic of scattered rays within an absorber .....	10
Figure 2.2 The dielectric constant of noble metals .....	13
Figure 2.3 The band diagram showing the photon-electron-photon conversion process at a plasmonic resonance.....	14
Figure 2.4 The localized field near the surface of an Au sphere .....	15
Figure 2.5 The wavelengths of plasmonic resonances for nanoplasmonic particles made of Al, Ag and Au.....	16
Figure 2.6 The electrical size of a nanosphere in AZO with different values of radius .....	17
Figure 2.7 a-Si thin film solar cells with plasmonic structures.....	18
Figure 2.8 Nanodome a-Si:H solar cell structure.....	19
Figure 2.9 The schematic of nanowire solar cells with radial junctions in each wire. ....	21
Figure 3.1 The comparison between the absorption in the a-Si:H layer of solar cells with different thickness values of the front spacer .....	23

Figure 3.2 (a) The schematic of a typical a-Si:H thin film solar cell. In this paper, we consider putting plasmonic structures in the back passivation layer; (b) The corresponding transmission line model of the typical thin film solar cell shown in (a). .....	26
Figure 3.3 The comparison of the absorption of a TFSC obtained by a full wave simulation and the transmission line method. ....	30
Figure 3.4 (a) The mapping of weighted absorption with respect to the thickness of the front passivation layer ( $t_1$ ) and the thickness of the back passivation layer ( $t_3$ ). (b) Light absorption in a-Si:H for the planar solar cell with $t_1=60$ nm and $t_3=50$ nm .....	32
Figure 4.1 The analogy between a (dipole) antenna and a radiator made of plasmonic particles	34
Figure 4.2 The schematics for (a) Radiating currents; (b) Non-radiating currents.....	35
Figure 4.3 The size of a small plasmonic particle with respect to a period of a sinusoidal wave at long wavelength.....	37
Figure 4.4 The localized electric field and the surface current on plasmonic spheres at the resonance of each one.....	38
Figure 4.5 The normalized radiation power by a single Au sphere with different sizes .....	39
Figure 4.6 The refractive index of the Au sphere array at different spacing .....	41
Figure 4.7 The surface current at the resonance of Au spheres with different spacings .....	42
Figure 4.8 The refractive index of particles with spacings of 150 nm and 500 nm.....	43
Figure 4.9 The radiated waves from two closely spaced Ag disks and a single silver disk .....	44
Figure 4.10 The spectrum of light absorption in the a-Si layer of a thin film solar cell coated with Ag nanospheres on top. ....	45
Figure 4.11 The absorption at short wavelengths of Ag spheres on top with respect to the radius of each sphere. The spacing is 400 nm.....	46

Figure 5.1 The real part of the effective permittivity and effective permeability of Au fishnet with different spacings. The thickness of fishnet is 20 nm and the line width is 100 nm. The Au fishnet is placed in SiO <sub>2</sub> whose dielectric constant is set to be 2.1. ....	50
Figure 5.2 The real and imaginary parts of the effective wave number of the fishnet .....	53
Figure 5.3 The schematic of an a-Si:H solar cell with 20 nm thick Au fishnet embedded in the back spacer .....	55
Figure 5.4 The total absorption of the solar cell with and without the embedded fishnet.....	56
Figure 5.5 The localization of electric field within the a-Si:H layer .....	57
Figure 5.6 Light absorption in the a-Si region of the solar cells.....	59
Figure 6.1 Sample geometries used in study .....	67
Figure 6.2 Experimental set-up used in study.....	70
Figure 6.3 Verification of measurement data by comparison of measurements with and without the furnace in place at room temperature .....	72
Figure 6.4 Variation of transmission through an empty furnace at 10 GHz as a function of temperature .....	74
Figure 6.5 Measured real part of permittivity for SRR <sub>  </sub> printed on FR4 substrate at various temperatures.....	75
Figure 6.6 Measured real parts of permeability for SRR <sub>l</sub> on FR4 substrate at various temperatures .....	76
Figure 6.7 Measured real parts of (a) permittivity and (b) permeability for the SRR <sub>random</sub> on FR4 substrate at various temperatures.....	78
Figure 6.8 Observed change in resonance frequency of FR4-SRR samples versus temperature.	79
Figure 6.9 Measured magnitude of S21 of the random SRRs on LTCC substrate.....	80

Figure 6.10 Observed change in resonance frequency of DuPont 951-SRR sample versus temperature .....	81
Figure 6.11 Observed change in plasma frequency for a thin wire medium (printed on FR4). ...	81
Figure 6.12 Measured temperature dependence of permittivity of DuPont 951 and FR4 averaged over X-band frequencies (8.2-12.4 GHz). (a) Real part; (b) Imaginary part.....	84
Figure 6.13 Temperature dependence of the conductivity of copper and silver.....	85
Figure 6.14 Change in dimensions of an SRR computed using ANSYS due to thermal expansion of silver and the substrate from 20°C to 400° .....	88
Figure 6.15 Numerically simulated (using Ansoft HFSS) $ S_{21} $ for random SRRs on an LTCC substrate at 20°C and 400°C.....	90
Figure 7.1. The unit cell of the LCCM design used in this study.....	92
Figure 7.2. FESEM micrograph showing the cross-section of an actual LCCM device .....	93
Figure 7.3. The light (AM 1.5, 100 mW/cm <sup>2</sup> ) and dark J-V and performance characteristics of an LCCM device. ....	95
Figure 7.4. The computed short circuit current density $J_{SC}$ as a function of $L$ .....	97
Figure 7.5 The schematic of the substrate nanodome solar cell .....	99
Figure 7.6 The schematics of the nanodome cells on a substrate .....	100
Figure 7.7 (a) The effective thickness of a-Si:H with respect to the dome-to-dome spacing $L$ . (b) The curvature height of the nanodome cell with respect to $L$ . ....	102
Figure 7.8 The absorption in the a-Si:H layer for the nanodome cell with different spacings. ...	103
Figure 7.9 The calculated $J_{sc}$ with respect to spacings. ....	104
Figure 7.10 The absorption of the optimized nanodome cell with $L=550$ nm.....	105

Figure 7.11 (a) The localized electric field and (b) the Poynting vectors of the optimized cell at $\lambda=681$ nm. ....	106
Figure 7.12 The schematic of the nc-Si nanodome cell on a substrate. ....	107
Figure 7.13 The calculated $J_{sc}$ of the nc-Si nanodome substrate cell with respect to spacings. .	108
Figure 7.14 The localized electric field in the optimized cell. ....	109
Figure 8.1. The schematic of the 1D grating design. ....	112
Figure 8.2. The schematic for the glancing angle deposition process to fabricate the AZO grating .....	113
Figure 8.3. The color map showing the parametric study of $J_{sc}$ with respect to $\alpha$ and $L$ . ....	116
Figure 8.4. The absorption spectrum of the three local maxima points. ....	117
Figure 8.5. The absorption spectrum of the optimized design ( $L=650$ nm, $\alpha=35^\circ$ ) at normal incidence for TE and TM polarizations and comparison to a planar cell with 277 nm and 505 nm a-Si:H. ....	118
Figure 8.6. The plots of the calculated energy density across the a-Si:H region. ....	120
Figure 8.7. The calculated $J_{sc}$ of the optimized design ( $L=650$ nm, $\alpha =35^\circ$ , $h_{eff}=277$ nm) at varying angles of incidence. ....	121
Figure 8.8. (a)The schematic of the optimized 2D grating design; (b)The absorption spectrum of the optimized 2D design compared to a planar cell with 322 nm a-Si:H. ....	122

# I. Introduction

## 1.1 Thin Film Photovoltaics

Thin film solar cells (TFSCs) have been proposed as a promising solution to reduce the cost of photovoltaic (PV) energy generation. The high cost of PV cells is the limit for further expansion of the PV market. In Figure 1.1, about half the cost in conventional Si wafer cells is for the semiconductor material, despite the variation of total cost due to comprehensive factors including manufacture scale, labor cost, government support, etc [1,2]. The amount of semiconductor in TFSCs is much smaller than conventional cells. The reduction of semiconductor usage achieved by TFSCs can be over 90%.

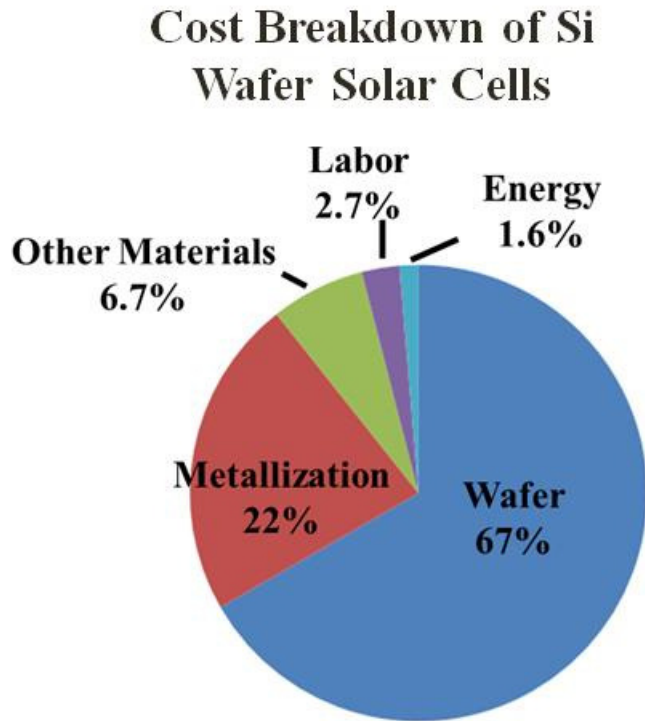


Figure 1.1 The cost breakdown of Si wafer solar panels [1,2].

Despite the low cost of TFSCs, current PV market is dominated by conventional Si wafer cells. In Figure 1.2, 85% of the global market is taken by wafer Si cells [2]. The limit for TFSCs is their efficiency. Compared to the efficiency of Si wafer cells, the efficiency of TFSCs is 30% lower [3]. Several reasons cause the low efficiency of TFSCs including poor material quality [4], insufficient light absorption [3, 5], etc. Besides, other considerations are necessary, such as environmental effect (CdTe) [3, 6-8], material availability (CdTe and CIGS) [9, 10], etc. In this dissertation, amorphous silicon (a-Si) is used as the semiconductor for TFSCs.

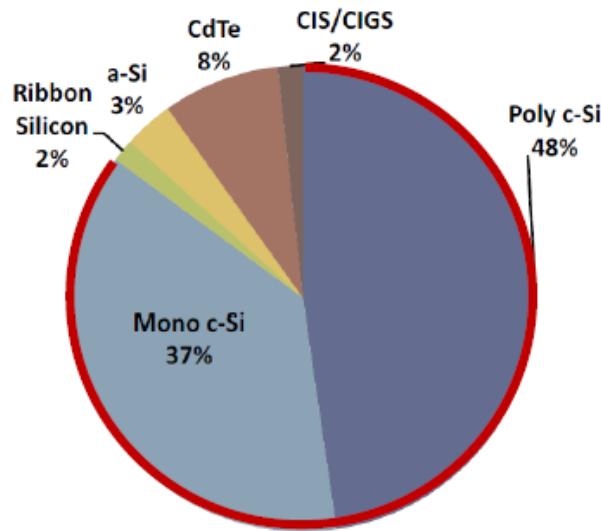


Figure 1.2 The pie plot showing the market share of each PV technology in 2010 [2].

Si is the most abundant semiconductor material on earth. Hence, the acquisition of Si is much easier and cheaper than other materials. Wafer cells use crystalline silicon (c-Si). The thickness of a c-Si wafer is around 180  $\mu\text{m}$  in order to achieve sufficient light absorption [11]. a-Si single junction TFSCs, however, consist of active layers less than 1  $\mu\text{m}$  thick. On one hand, the absorption coefficient of a-Si does not require a very thick layer for light absorption. Unlike c-Si, a-Si is a quasi-direct bandgap material. In Figure 1.3, the absorption coefficient of a-Si, hence,

increases very quickly from nearly 0. An a-Si layer of 3 $\mu$ m thick is able to absorb over 90% of incoming photons above its bandgap. The bandgap of a-Si is between 700 nm and 800 nm depending on the level of hydrogenation [12]. Compared to c-Si whose bandgap is around 1100 nm [14], a-Si cannot absorb photons in the infrared region but a-Si solar cells have a higher open circuit voltage [15]. a-Si is able to be fabricated by low temperature process [16] and is a candidate for roll-to-roll fabrication [17].

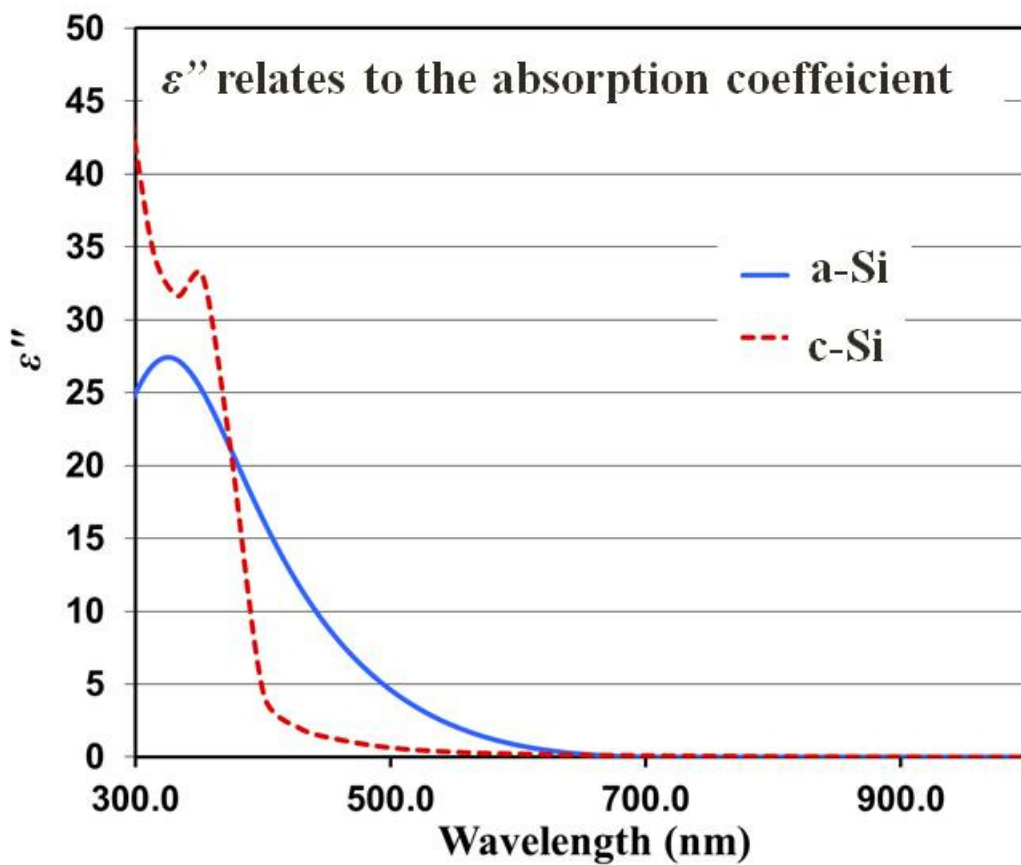


Figure 1.3 The comparison of the imaginary part of permittivity of a-Si and c-Si. The imaginary part of permittivity is proportional to the absorption coefficient of a material. The optical constants of a-Si and p-Si are from literature [12, 13].



The amorphous structure of a-Si results in poor carrier transport [18]. The upper limit of the distance for photon-generated carriers to travel in a-Si, defined as the diffusion length of a-Si, is around 400 nm [19]. It is very probable that carriers will encounter recombination when they travel longer than the diffusion length. Consequently, the thickness of a-Si active layer in TFSCs should be in the order of 400 nm to avoid significant recombination. In that case, light absorption in a-Si is insufficient.

## 1.2 Light Trapping in Thin Film Solar Cells

Light absorption in semiconductors is described by the Beer Lambert law [20].

$$A(z) = I_0(1 - e^{-\alpha L}) \quad (1.1)$$

$I_0$  is the intensity of incident light,  $\alpha$  is the absorption coefficient of the semiconductor and  $L$  is the effective light path inside the semiconductor. When  $\alpha$  is small, a large  $L$  is required for sufficient light absorption. In Figure 1.4, the required optical thickness in a-Si at 650 nm is over  $6\mu\text{m}$ . The length of light path is directly related to the thickness of an active layer. Since the thickness of a-Si solar cells is far from the requirement for the length of light path near bandgap, light absorption at those wavelengths is also limited. The key point for enhancing light absorption in a-Si TFSCs, therefore, is to obtain a long light path within a very limited thickness of active layers.

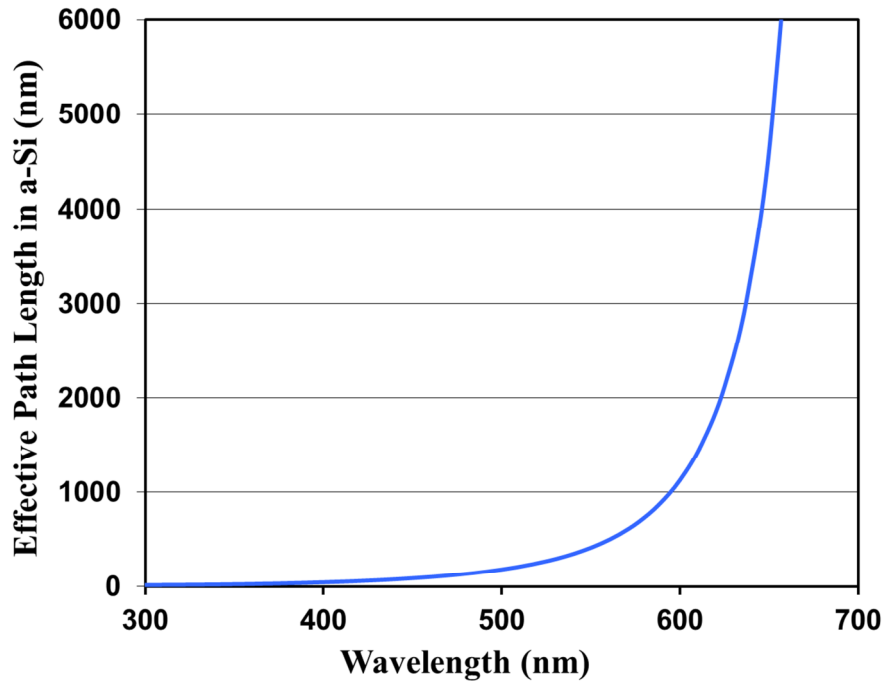


Figure 1.4 The required length of light path at each wavelength in order to achieve 90% of light absorption within a-Si. The calculation is based on Beer Lambert law. The reflection at the front surface of a-Si is considered to be 0.

The easiest way to increase the length of light path, as shown in Figure 1.5, is to add a reflection surface at the back end of solar cells. Light travels at least twice the thickness of active layers. This method is used by most solar cells. Metals are able to serve the purpose. The back reflector also serves as an electrode for solar cells.

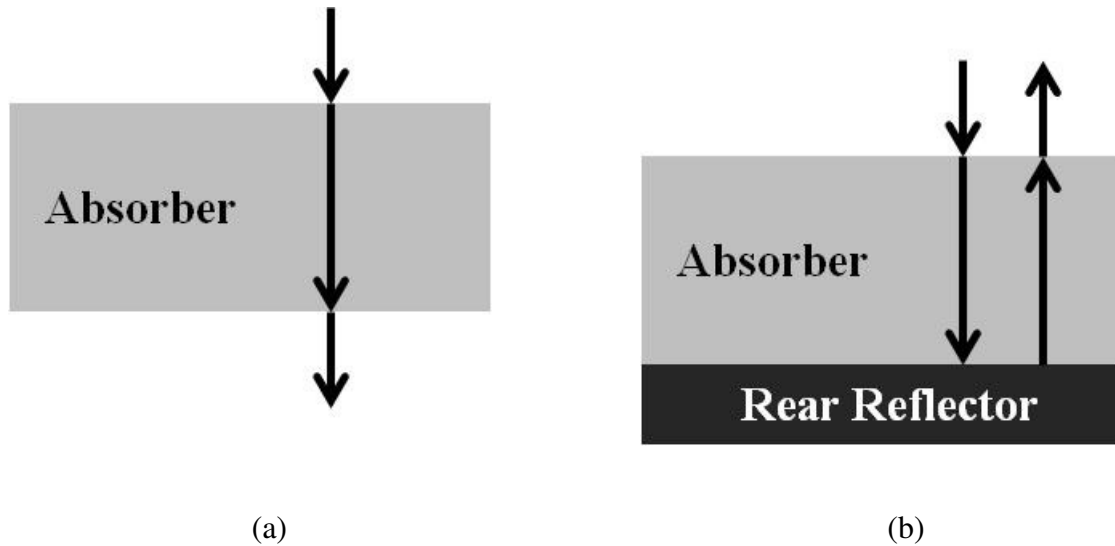


Figure 1.5 (a) Light transmits through a semiconductor layer without any back reflection; (b) The incident light is reflected by the rear reflector [21]. The length of optical path is increased by at least twice.

The increase in light path by back reflectors, however, is far from enough. Advanced designs have to be considered for further improvement of light absorption. In Figure 1.6, a schematic of rays in an absorbing layer is shown. Light is incident normally or at small angles on the absorber. If the back reflector is planar, the reflected light will be travelling at small angles toward the top surface of the absorber and will be escaping from the absorber. The resulting light path in this case is just slightly longer than twice the thickness of the absorber. If a light trapping design is integrated into the rear reflector, the reflected light in the absorber will be at large angles off the horizontal plane. Light path within the absorber will be significantly increased due to two reasons. First, the reflected light can travel a distance much longer than the absorber thickness before it reaches the top surface of the absorber. Second, if light is reflected at angles greater than the critical angle at the top interface of the absorber, the reflected light that reaches

the top surface will be undergoing total internal reflection. As a result, light will be trapped in the absorber. The schematic in Figure 1.6 is in ideal conditions but it clearly shows the idea to design light trapping: making light travel at large angles off the horizontal plane of an absorber in order to 1) take advantage of the horizontal space to increase one wave travelling distance of light and to 2) generate total internal reflections within the absorber to trap light.

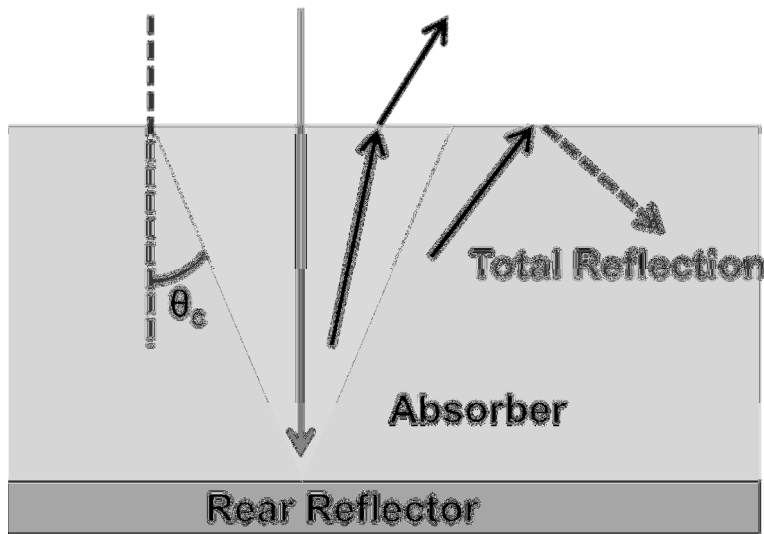


Figure 1.6 The schematic showing rays within an absorber.  $\theta_c$  is the critical angle at the top surface of the absorber layer.

In this dissertation, we firstly review existing approaches to design light trapping structures. Light absorption in solar cells can be enhanced by surface texturing, plasmonic designs and photonic designs. The existing methods, although have exhibited their advantage, undergo several disadvantages that prevent them from further improvement. They either do not show sufficient enhancement or introduce additional loss in optics and carrier transport. Light trapping by plasmonic structures is dependent on the radiation of photons at plasmonic resonances. We resemble plasmonic structures to antennas in order to explain the radiation at

plasmonic resonances. The distribution of surface charges, as well as the amount of surface charges, is the determinant for plasmonic radiation. Non-radiating energy absorbed by plasmonic structures will be dissipated. We propose the fishnet structure as a new type of plasmonic structures for light trapping in a-Si thin film solar cells. The enhancement of short circuit is 13.28%. The temperature dependence of plasmonic resonances is discussed by studying the temperature dependence of microwave metamaterials. The physics of optical plasmonic structures and microwave metamaterials is very similar. Photonic structures, such as the nanodome structure and the grating structure, are also studied in this dissertation for light trapping purposes. Compared to planar cells with the same amount of a-Si, the studied photonic structures are able to enhance light absorption by over 20%. Besides the significant enhancement in light absorption by the photonic structures, our designs also include considerations for carrier transport. Light absorption is achieved without hurting the transport of carriers in a-Si.

## **II. A Review of Methods for Light Trapping**

### **2.1 Background**

As mentioned in the first chapter, the key point for light trapping is to increase the length of light path within the semiconductor absorber. Figure 1.6 depicts the concept that is used for every light trapping design. Light traveling within a solar cell needs to be manipulated in a way that it travels outside the escape cone defined by the critical angle at the top surface of the absorber. Light traveling within the escape cone is going to escape solar cells. Hence, many designs have been proposed to scatter incident light.

A solar cell is a system integrated by an optical subsystem and a semiconductor subsystem. A good performance of solar cells requires simultaneous high quality performance of both subsystems. The improvement in the optics part may be cancelled by the downgrade in the semiconductor part. Additional carriers generated due to light trapping designs may undergo recombination and hence cannot contribute to current generation. Therefore, an important principle for light trapping designs in solar cells is to reduce as much as possible its negative impact on carrier transport.

### **2.2 Light Trapping by Rough Surfaces**

A simple but effective approach to increase the length of light path is to rough the surface of absorbers. In Figure 2.1, light is normally incident on a rough surface. Instead of specular reflection that occurs for a planar rear reflector, diffusive reflection occurs within the absorber. If the pattern of surface roughness is random, the reflected light intensity is uniform across all directions.

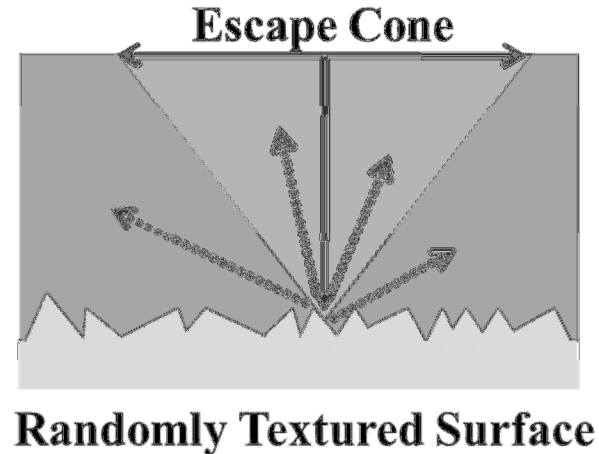


Figure 2.1 A schematic of scattered rays within an absorber. The escape cone is defined by the critical angle at the top surface the absorber. Light traveling within the escape cone is going to escape the absorber.

Light reflected within the escape cone is going to transmit through the top surface of the absorber. The reflected light outside the escape cone is going to undergo total internal reflection and be trapped within the absorber. Theoretical work has been done to predict the enhancement of light absorption by a randomly textured rough surface [22, 23]. The theoretical calculation was done based on three assumptions: 1) The absorber is thick so that the top surface is within the Fraunhofer region of the reflected light; 2) The absorption coefficient of the absorber is very small; 3) The reflected light intensity is uniform at all directions. A theoretical limit of optical path enhancement is obtained from the calculation. As a result of the calculation, the enhancement of optical path within a weak absorber by a rough surface is no more than  $4n^2$ . Here,  $n$  is the refractive index of the absorber and the material above the absorber is air.

The refractive index of a-Si is approximately 4 at its bandgap. Hence, the maximal enhancement is 64. In practical solar cells, there is a spacer layer on top of the absorber layer for the purpose of anti-reflection and surface passivation. The maximal enhancement of optical path, therefore, is decreased to  $4n^2/n_s^2$ .  $n_s$  is the refractive index of the spacer layer. If the spacer is made of AZO whose refractive index is 2, the maximal enhancement is only 16. With this enhancement, the maximal optical path in a 500 nm-thick a-Si is only 8000 nm. This length is far below the length calculated in Figure 1.4, in which over 70  $\mu\text{m}$  is required to obtain 90% at the bandgap of a-Si. In fact, the maximal enhancement is very difficult to obtain by a rough surface because its surface pattern is not a real random pattern.

The fabrication methods of rough surfaces vary case by case, depending on the requirement on material type and feature size. A single crystalline substrate can be textured by etching along the faces of the crystal planes. The resulting rough surface is made up of pyramids. The orientation of pyramids can be inverted. The feature size of each pyramid is in the order of 5  $\mu\text{m}$ . Compared to the thickness of a Si wafer ( $\sim 180$  nm), the feature size is negligible [24, 25].

The above mentioned method, however, does not apply to thin film solar cells whose thickness is less than 1  $\mu\text{m}$ . Nanofabrication technique, such as the Asahi U-type process, has been implemented in a-Si/nc-Si TFSC [26-28]. The substrate was roughened by this process and the solar cells are deposited on the substrate conformally. The feature size of the rough surface can be as small as 40 nm. The efficiency of light scattering by a rough surface, measured by a parameter called haze factor [29], is determined by each process. The haze factor of an object is the ratio between the luminescence of the object and the luminescence of the scattering medium through which it is being viewed. It refers to the percentage of incident light that is scattered diffusely by a rough surface. The feature size needs optimization to achieve the highest



scattering efficiency. The haze factor of Asahi U-type rough surface is only 10% [30]. New processes, such as the Asahi HU-type process, has been developed in order to achieve a haze factor of 90% [30].

### 2.3 Light Trapping by Plasmonic Particles

Light absorption in solar cells can also be enhanced by employing metallic particles. Metallic particles are placed in the front or back end of solar cells [31-33]. The particles are made of noble metals such Au and Ag. The dielectric constant of metal is described by the Drude model [34]:

$$\epsilon = \epsilon_{\infty} \left(1 - \frac{\omega_p}{\omega}\right) \quad (2.1)$$

$\omega_p$  is the plasma frequency. The plasma frequency is defined as the frequency where the real part of permittivity is 0. The dielectric constant of a material will be negative at frequencies lower than the plasma frequency. The plasma frequencies of noble metals are in the UV region. Figure 2.2 shows the permittivity of metals at optical frequencies. The optical constants of metals are from well cited literature [35]. The permittivity of copper, silver, gold and Aluminum is shown. Their plasma frequencies are higher than 1000 THz (300 nm).

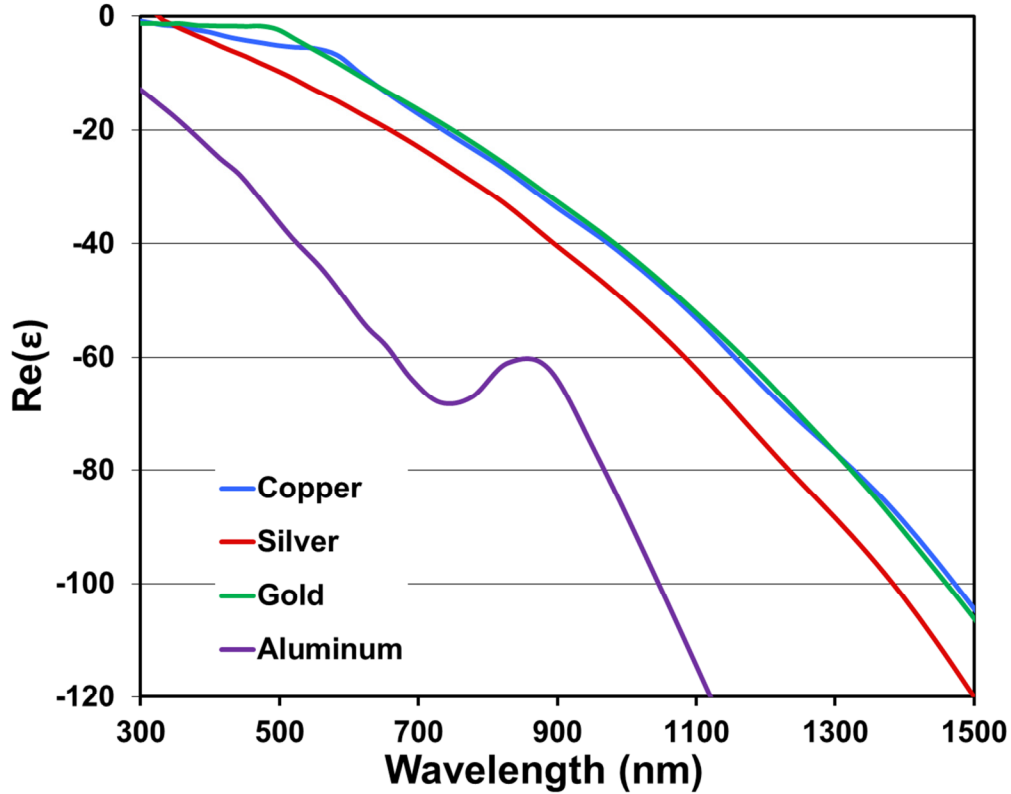


Figure 2.2 The dielectric constant of noble metals [35].

As a result, the permittivity of a metal is treated to be negative infinity at microwave frequencies. The reflection at a metal surface is approximately 100% at microwave frequencies. The plasma frequency is related to the density and mass of electrons as shown in Eq. 2.2.

$$\omega_p = \sqrt{\frac{n_e e^2}{m \epsilon_0}} \quad (2.2)$$

$n_e$  is the density of electrons,  $e$  is the electron charge,  $m$  is the mass of electrons and  $\epsilon_0$  is the dielectric constant of free space. In visible band, the permittivity of metals is finite.

The electrons in a particle are driven by incident electric field and then exhibit oscillating motions. The oscillation achieves maximal strength at a frequency call the plasmonic resonance

frequency. In Figure 2.3, electrons at a plasmonic resonance absorb the energy of photons and reach higher energy levels. The unstable electrons at higher energy levels will later release energy in the form of photon radiation.

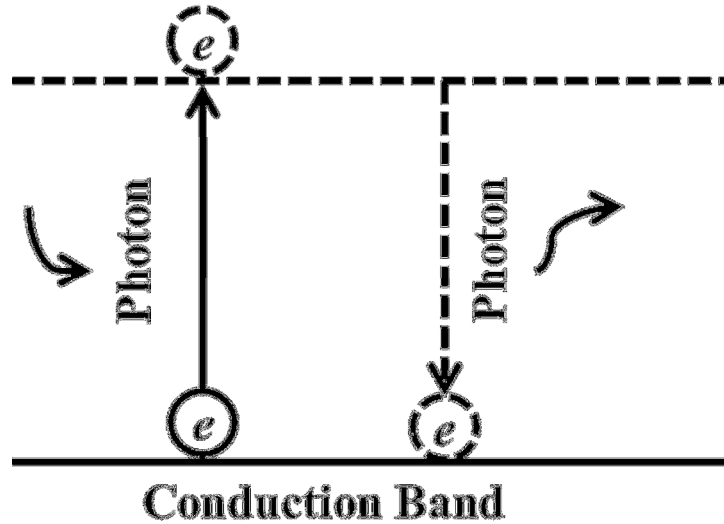


Figure 2.3 The band diagram showing the photon-electron-photon conversion process at a plasmonic resonance.

The radiated photons will be travelling toward directions defined by the electron distribution on the surface of plasmonic structures. If the photons cannot radiate, the released energy by high energy electrons will be dissipated.

The distribution of electrons is related to the strength of near field around each plasmonic structure. A spot with a higher electron density exhibits a higher intensity of surrounding electric field. Figure 2.4 shows the intensity of localized electric field at the resonance of a gold particle. The electric field is highly enhanced at the two ends of the particle, indicating that charges are separated by the incident electric field. An effective dipole is created.

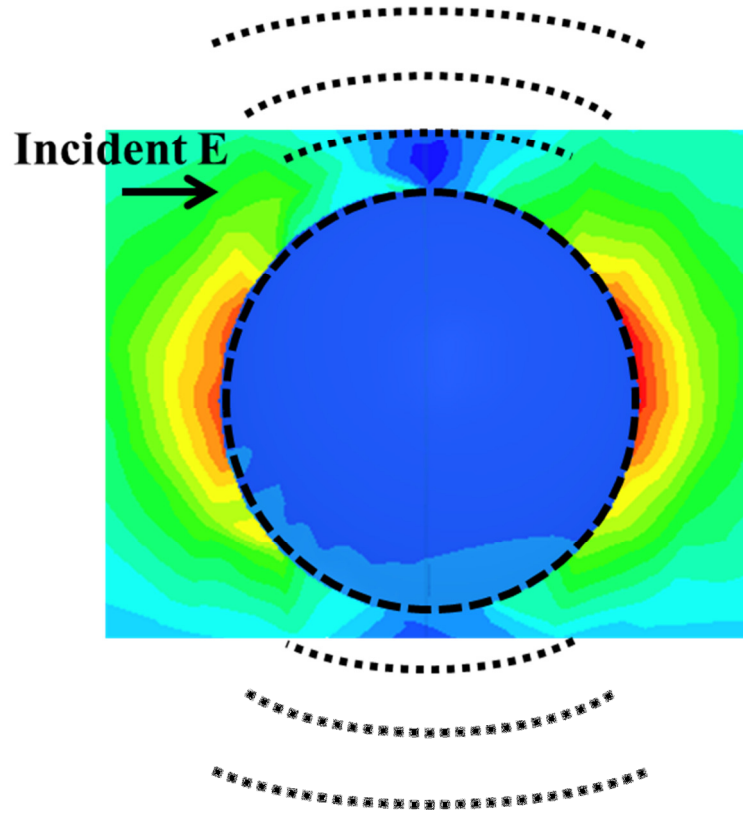


Figure 2.4 The localized field near the surface of an Au sphere. The radius of the sphere is 40 nm and the host medium is SiO<sub>2</sub> ( $\epsilon_r=2.1$ ). An electric dipole is formed at the resonance of the sphere. The radiation pattern of the sphere is similar to an electric dipole.

The resonance of a nanoplasmonic particle can be described by dipole approximation [36] when the size of each particle is much smaller than the wavelength.

$$\alpha = 4\pi a^3 \epsilon_2 \frac{\epsilon_1 / \epsilon_2 - 1}{\epsilon_1 / \epsilon_2 + 2} [1 + o(k_2 a)^2] \quad (2.2)$$

$\alpha$  is the polarizability,  $\epsilon_1$  is the permittivity of the metal,  $\epsilon_2$  is the permittivity of the host medium,  $k_2$  is the wave number in the host medium and  $a$  is the diameter of the nanosphere. This approximation is based on electrostatics conditions. The condition for electrostatics is satisfied

for small particles. The incident field has nearly zero phase variation across a particle. According to the solution, the resonance frequency, called the Frohlich frequency, is independent of particle geometry. It is determined only by the optical constants of metals and dielectric host materials. Because the size of particles is much smaller than a wavelength, the electric field on each particle is supposed to have negligible phase variation. The Frohlich frequencies of nanoplasmonic particles made of typical metals are shown in Figure 2.5.

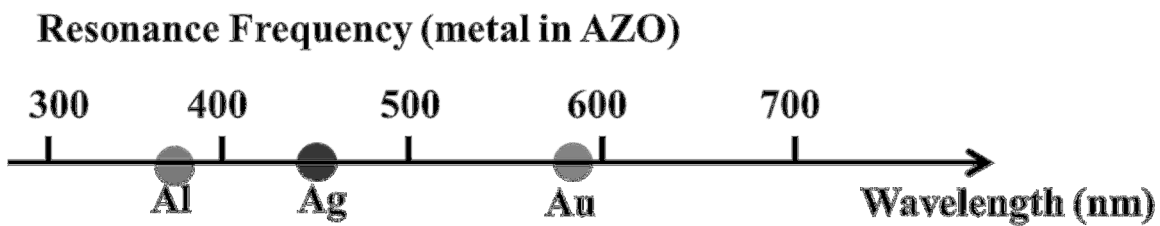


Figure 2.5 The wavelengths of plasmonic resonances for nanoplasmonic particles made of Al, Ag and Au. The host medium is AZO [37].

The wavelengths of the plasmonic resonances for small plasmonic particles are below 600 nm. The absorption coefficient of a-Si (and many other semiconductor materials) is high enough to absorb sufficient light without the aid of light trapping designs. In order to shift the resonance to long wavelength region where the bandgap of a-Si locates, the size of particles needs to increase. When the size of a particle is greater than the Rayleigh limit, the dipole approximation is not valid. Figure 2.6 shows the electrical size of nanospheres compared to the Rayleigh. The electrical size of a particle is wavelength dependent.

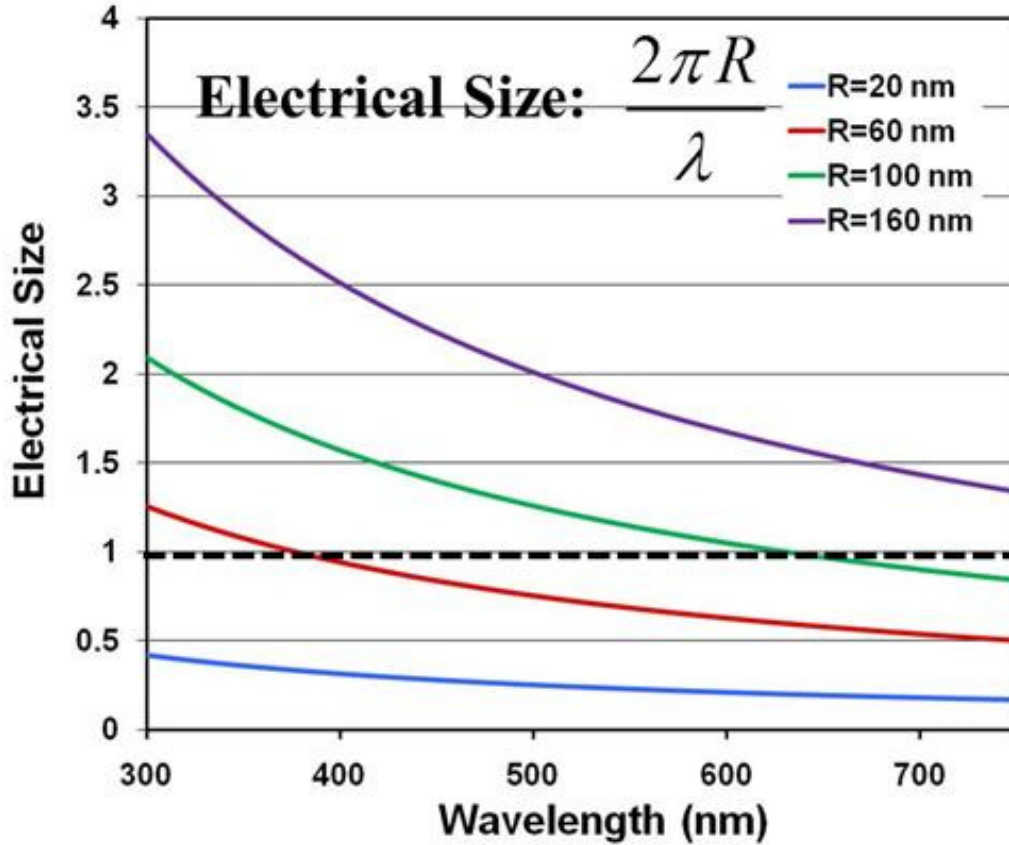


Figure 2.6 The electrical size of a nanosphere in AZO with different values of radius. The electrical size is wavelength dependent. The Rayleigh limit is defined when the electrical size is 1.

In plasmonic solar cells, metallic particles and metallic gratings are integrated with a-Si thin film solar cells as shown in Fig 2.7. Light scattering from plasmonic structures is the combined effect of plasmonics and photonics.

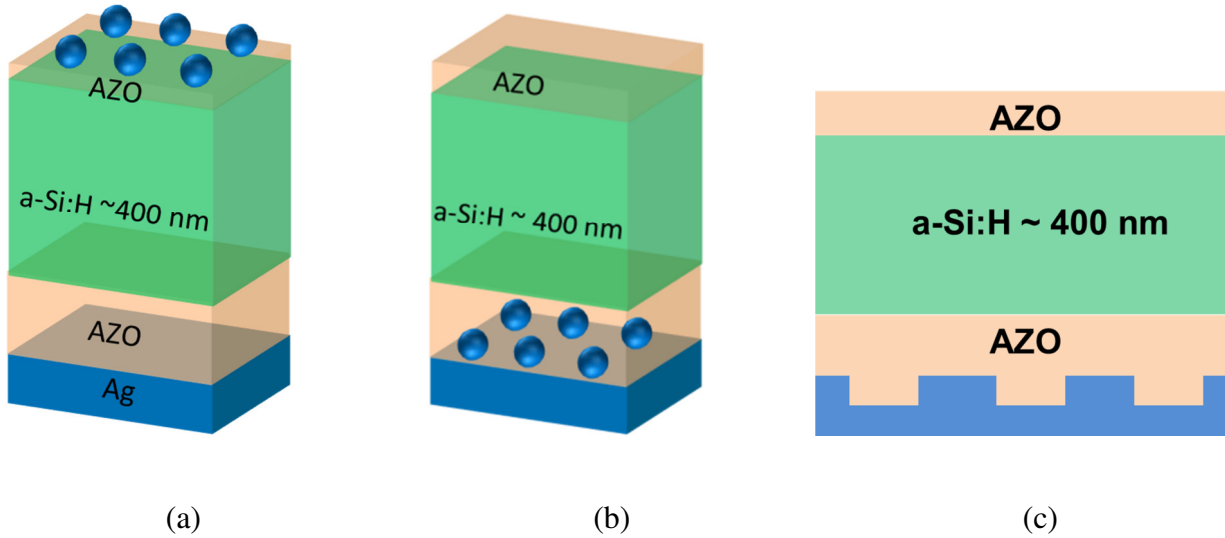


Figure 2.7 a-Si thin film solar cells with plasmonic structures (a) Plasmonic particles on top of solar cells; (b) Plasmonic particles at the bottom of solar cells; (c) Corrugated back electrode as the plasmonic structure for light trapping purposes.

The geometry is not limited to spheres. Hemispheres, disks and other simple geometries can be used. The resonance of plasmonic particles is designed to occur at the bandgap of the semiconductor. Non-resonant scattering occurs at the off-resonance wavelengths of particles. The geometry of particles is very difficult to control in fabrication. However, plasmonic particles with acceptable deformation can be fabricated by a cheap process. The size of each particle is controllable but the shape of each particle is random. Theoretical calculations showed that the maximal enhancement by plasmonic structures is  $4n^2 + n\lambda/h$  [38].  $n$  is the refractive index of the absorber,  $\lambda$  is the wavelength and  $h$  is the absorber thickness.

One disadvantage of plasmonic particles is heated dissipation. As mentioned above, if the absorbed photon energy cannot radiate, it will result in “ohmic loss” in metallic particles or dielectric loss in surround media. Instead of radiating waves, evanescent waves are generated

from plasmonic particles. The decay length of the evanescent waves is very short. As a result, the photon energy will attenuate before it reaches the semiconductor region of a solar cell.

## 2.4 Light Trapping by Nanodome and Nanowire Geometry

Light absorption in solar cells can also be enhanced by shaping solar cells into non-planar geometry. Unlike rough surfaces where only a small part of the absorber is involved in light trapping, shaping the absorber can make use of the whole absorber layer in light trapping. So far, many people have implemented solar cells with nanodome geometry and nanowire geometry.

### 2.4.1 Nanodome Geometry

Shaping solar cells into periodically spaced nanodomains has been realized by researchers [39, 40]. In Figure 2.8, a schematic of solar cells with nanodome geometry is shown. Layers of a-Si thin film solar cells were deposited on a patterned substrate. The substrate was patterned with nanocones before the deposition process. The geometry of each nanocone and the spacing between two neighboring cones were determined based on the requirement for light trapping.

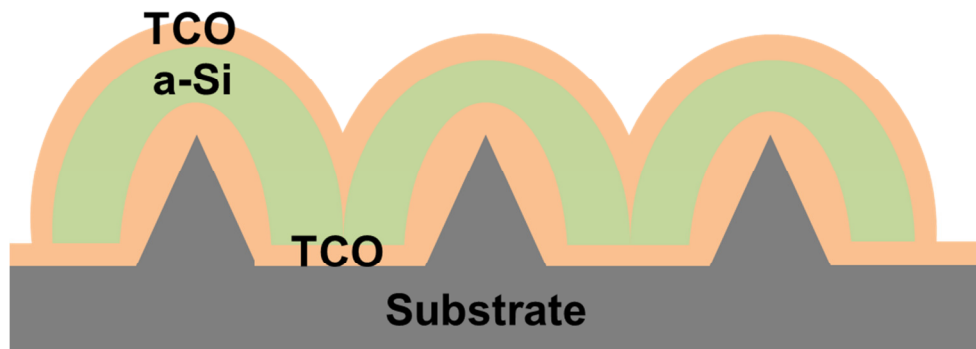


Figure 2.8 Nanodome a-Si:H solar cell structure. All the layers for thin film solar cells are made by conformal deposition on a patterned substrate.



The reported enhancement of short circuit current by the nanodome geometry is over 53% compared to a planar cell with the same thickness of a-Si. The resulting efficiency of the cell with nanodome geometry, however, does not increase as much as the short circuit current. The enhancement of efficiency is only 25.5% compared to a planar cell with the same thickness of a-Si. The nanodome geometry increases surface recombination due to the increased surface area and additional surface defects. As a result, the fill factor is decreased from 0.54 to 0.45 [39].

#### **2.4.2 Nanowire/Microwire Geometry**

Solar cells can also be shaped into periodic long wires. Light incident on the periodic wires will undergo repeated reflections among wires and hence be trapped. The length of each wire, as well as the periodic spacing between each two wires, is determined in order to achieve the best light trapping effect at designed wavelengths.

Radial junctions are used for carrier collection as shown in Figure 2.9. In this configuration, the length for carrier collection is much shorter than the minority carrier diffusion length. Therefore, low quality semiconductors can be used. In the typical process to fabricate wire-geometry cells, the p doped layer is firstly fabricated using the nanocluster-catalised vapor liquid solid (VLS) method and then the outer n doped shell is deposited [41]. The diameter of each radial junction is usually around 100 nm and the height of each wire is usually less than 10  $\mu\text{m}$ . A c-Si nanowire solar cell can enhance the short circuit current by 18% based on the corresponding planar control cell. Increasing the diameter of each wire to micrometer scale has been predicted to have better absorption and the microwire structure is especially useful for semiconductors with their minority carrier diffusion lengths in the order of several micrometers. An optimized Si microwire array with the effective thickness of 20  $\mu\text{m}$  has been reported to have

comparable light absorption with a corresponding 300  $\mu\text{m}$  planar control cell [42]. The wire-shaped cells, however, exhibit the same problem as the nanodome cells. The increased surface area results in low cell efficiencies [43].

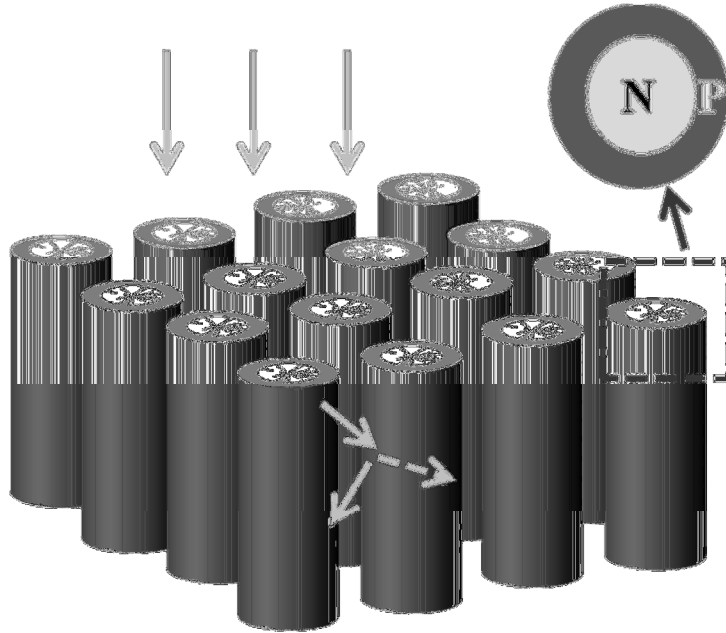


Figure 2.9 The schematic of nanowire solar cells with radial junctions in each wire.

## 2.5 Summary

Light trapping in solar cells are not limited to the above mentioned designs. However, the above mentioned designs include the three most important approaches for light trapping designs.

### 1) Surface Texturing Approach

Surface texturing is cheap to fabricate and has been widely used in industry. It achieves acceptable enhancement in light absorption with very small negative impacts on carrier transport. The major limit of surface texturing is its insufficient enhancement factor for light absorption. Although the theoretical maximal enhancement by surface

texturing is close to enough for thin film solar cells, the practical enhancement is always much lower than the theoretical limit due to impurity in the randomness of surface patterns.

## 2) Plasmonic Approach

Light absorption in solar cells with plasmonic particles is enhanced by a significant amount. The enhancement, however, is limited within a very small wavelength region. The nature of plasmonic resonances indicates that a plasmonic resonance is narrow banded. Trapping light in solar cells is required to work over a broad spectrum. An ideal geometry of each particle is hard to fabricate. Instead, particles with certain levels of deformation can be fabricated by a cheap process. The variation of the size of each particle is controllable. A important disadvantage of plasmonic particles in solar cells is the loss of absorbed photons in undesired regions. The absorbed energy may be trapped within the metallic particles or surrounding regions so that the dissipated energy cannot lead to carrier generation. The plasmonic approach can also be used by shaping the back electrode into periodic structures. This method, however, encounter the same problems as plasmonic particles.

## 3) Photonic Approach

Shaping cells into geometries, such as nanodomes and nanowires, can significantly enhance light absorption in semiconductor. Similar designs made use of periodicity of element-to-element spacing to achieve the lowest reflection at a desired wavelength region. Besides, each element is able to guide incident light at desired directions. The optical loss due to undired absorption in non-semiconductor layers is very small. However, the carrier transport is hurt by increasing surface area.

### III. Transmission Line Theory for Thickness Optimization of Anti-Reflection Coatings

#### 3.1 Background

Light trapping designs are targeted for the band gap region of the semiconductor materials in solar cells. The absorption coefficient of a semiconductor is very small at its bandgap. Light absorption at short wavelengths (less than 500 nm) is not a concern for PV researchers. A semiconductor is able to absorb sufficient light (>90%) at short wavelengths. Solar cells can achieve very good absorption at those wavelengths without any light trapping designs. However, a high absorption coefficient cannot guarantee sufficient light absorption in solar cells.

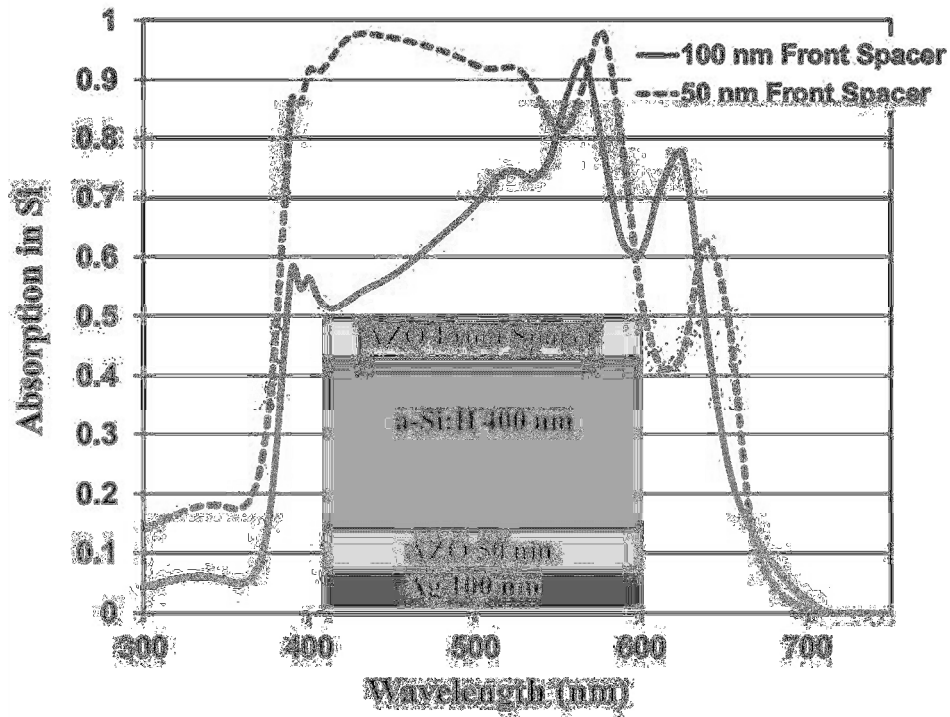


Figure 3.1 The comparison between the absorption in the a-Si:H layer of solar cells with different thickness values of the front spacer. The thickness of a-Si:H is 400 nm in both calculations.

In Figure 3.1, the blue line is the absorption of a 400 nm thick a-Si:H slab calculated with two different thickness values for the front spacer. The optical constants of materials are from well recognized literature [12, 35, 37]. The a-Si:H layer is sandwiched by two spacer layers made of AZO. The thickness of the back spacer is 50 nm in both cases. An Ag slab of 100 nm is placed at the back as the back electrode of the solar cell. Light absorption at short wavelengths for the cell with a 100 nm-thick front spacer is much worse than the other one with a 50 nm-thick front spacer. The 100 nm-thick front spacer is not a proper design for the solar cell in Figure 3.1. Although a-Si:H is able to absorb sufficient light for wavelengths less than 500 nm, an improper design of the anti-reflection coating would prevent light from entering the semiconductor layer. Light absorption in a solar cell is defined by  $1-R$ , where  $R$  is the reflectivity of at the front end of the solar cell. A prerequisite for sufficient light absorption is to allow sufficient light enter the cell. A solar cell without a proper anti-reflection coating is would absorb much less than its absorption capability. In Figure 3.1, the short wavelength absorption of the two cases is quite different although the volume of the absorber is the same. Therefore, a proper design of the anti-reflection layer is crucial to a solar cell. A sufficient light absorption at short wavelengths is the requirement before any further actions for light trapping designs at long wavelengths.

A reflection of electromagnetic waves occurs at the interface of any two media whose indexes are not matched. Since a solar cell is a system of multiple layers, the main idea of an anti-reflection design is to make the reflected waves cancelled by each other. The simplest anti-reflection coating is a transparent layer on top of the solar cell. The refractive index of the transparent layer is between the semiconductor layer and the environmental materials (air, glass, *etc.*). This method is called index matching. It replaces the sharp contrast of the material properties at an interface with a slower gradient. Based on this method, a quarter wave

transformer is invented to achieve ideally zero reflection at a certain wavelength. It tells us that the best index matching design is a transparent layer of a quarter wavelength with a designed refractive index of the matching layer.

The principle of a quarter wave transformer is to make the waves reflected at the back surface of the matching layer cancel the waves reflected at the front surface of the matching layer. The disadvantage of a quarter wave transformer is its narrow bandwidth. The performance of a quarter wave transformer degrades very quickly when moving away from the working wavelength. There are two major problems in designing the quarter-wave anti-reflection layer in solar cells: 1). A solar cell is multi-layer system. The determination of the refractive index of the matching layer requires the consideration of all layers. 2). The solar spectrum is non-uniform. A weighting function due to the solar spectrum is necessary.

The design of an anti-reflection coating can be implemented by full wave numerical codes, which deals exactly the 3D model of solar cells. This approach is straightforward and accurate but pays the price of low speed. The calculation speed can be increased if the design is obtained by analytical solutions. In this section, we make use of the transmission line theory that has been widely used for multi-layer problems in microwave engineering. Complex 3D structure is simplified into 1D transmission line models and the multi-layer problems are transferred into circuits. The complicated wave propagations within solar cells are calculated by circuit parameters which are related to the material properties of each layer. The design of an anti-reflection coating is based on the optimization of these circuit parameters.

Electromagnetic waves reflect at any interface of two different media, resulting in repeated reflections within solar cells. Standing waves are generated due to the interference

among the multi-reflected waves. In transmission line theory [44], the repeated reflections are counted by circuit parameters. Each layer of a solar cell is characterized by three parameters: the wave impedance, the length and the propagation constant. The wave impedance and propagation constant of each layer is related to the material properties of that layer and the polarization state of the incident light. The total reflection at the front surface of a solar cell is measured by the matching condition between the input impedance at the front surface and the intrinsic impedance of the environmental material. Therefore, a complex field analysis for wave propagation in thin film solar cells is converted into a simple circuit problem.

### 3.2 Transmission Line Theory for Thin Film Solar Cells

A typical a-Si:H thin film plasmonic solar cell and its corresponding transmission line model are shown in Figure 3.2.

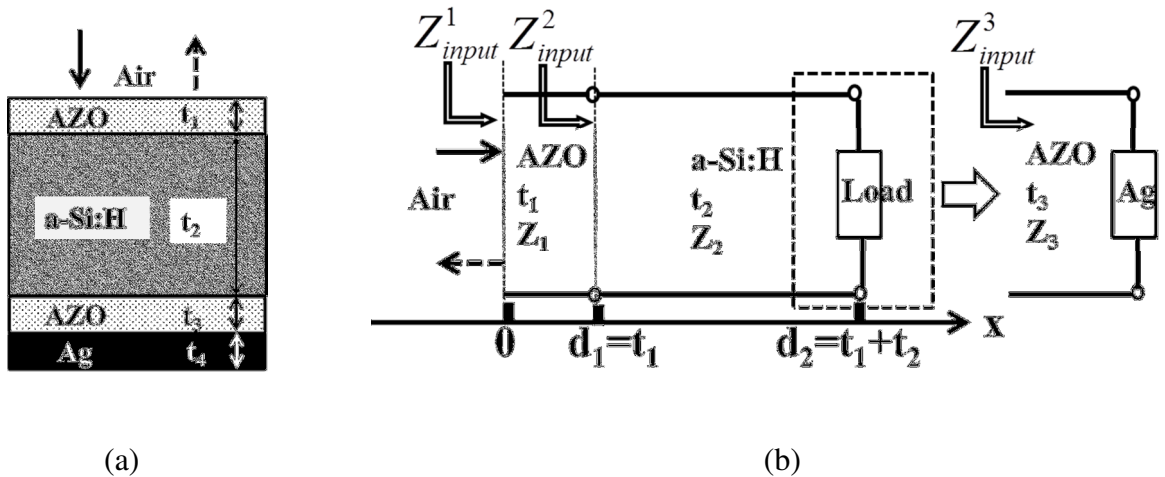


Figure 3.2 (a) The schematic of a typical a-Si:H thin film solar cell. In this paper, we consider putting plasmonic structures in the back passivation layer; (b) The corresponding transmission line model of the typical thin film solar cell shown in (a).

The transmission line parameters of each section are dependent on the material properties of each layer in the solar cell. In this paper, we consider only normal incidence with TE polarization. Thus, the wave impedance of each section is the same as the intrinsic impedance of each layer:

$$Z_n = \sqrt{\frac{\mu_n}{\epsilon_n}} \quad n=1,2,3,4. \quad (3.1)$$

$\mu_n$  and  $\epsilon_n$  are respectively the permeability and permittivity of each layer. In future, we put the plasmonic structure at the back end of solar cells in order to avoid any possible blocking of light. The plasmonic structure embedded in the back passivation layer will couple to the back electrode. They cannot be considered as two independent layers. Hence, integrating these two layers into one can account for all the interactions between them. As long as the back electrode is thick enough ( $>100$  nm) and no light passes through it, the integrated layer is considered as the load of the transmission line.

The total reflection of the solar cell is obtained by comparing the input impedance of the solar cell with that of the environmental medium:

$$R = \left| \frac{Z_{input} - Z_0}{Z_{input} + Z_0} \right|^2 \quad (3.2)$$

$Z_0$  is the impedance of the environmental medium (which is air in this paper) defined by Eq. 3.2. Obtaining the input impedance requires a backward analysis starting from the load. Each layer is integrated with its load and becomes the load of its preceding layer. The load impedance, which is also the input impedance, of the  $n$ th layer is calculated by



$$Z_{input}^n = Z_n \frac{Z_{input}^{n+1} + Z_n \tanh(\gamma_n L_n)}{Z_n + Z_{input}^{n+1} \tanh(\gamma_n L_n)} \quad (3.3)$$

$$\gamma_n = \alpha_n + j\beta_n = j\omega\sqrt{\mu_n \epsilon_n} \quad n=1,2,3 \quad (3.4)$$

$\gamma_n$  and  $L_n$  are the wave propagation constant and length of the  $n$ th layer. Hence, the input impedance of the solar cell is also the input impedance when  $n=1$  and the total absorption of the solar cell is simply  $1-R$  with  $R$  calculated by Eq. 3.2.

Since the semiconductor layer is not the only layer that absorbs power, photons are not guaranteed to be absorbed only in the semiconductor layer and generate electron-hole pairs. In order to find out light absorption in the semiconductor layer, we need to find out the field in each layer and then apply Poynting's theorem. In the  $n^{th}$  layer, we have

$$E_n(x) = E_n^+ e^{-\gamma_n x} + E_n^- e^{\gamma_n x} \quad (3.5)$$

$$H_n(x) = \frac{E_n^+}{\eta_n} e^{-\gamma_n x} - \frac{E_n^-}{\eta_n} e^{\gamma_n x} \quad (3.6)$$

and the boundary conditions at  $x=d_{n-1}$ :

$$E_n^+ e^{-\gamma_n d_{n-1}} + E_n^- e^{\gamma_n d_{n-1}} = E_{n-1}^+ e^{-\gamma_{n-1} d_{n-1}} + E_{n-1}^- e^{\gamma_{n-1} d_{n-1}} \quad (3.7)$$

$$\frac{E_n^+}{\eta_n} e^{-\gamma_n d_{n-1}} - \frac{E_n^-}{\eta_n} e^{\gamma_n d_{n-1}} = \frac{E_{n-1}^+}{\eta_{n-1}} e^{-\gamma_{n-1} d_{n-1}} - \frac{E_{n-1}^-}{\eta_{n-1}} e^{\gamma_{n-1} d_{n-1}} \quad (3.8)$$

By solving the boundary conditions, we obtain

$$E_n^+ = \frac{(1 + \frac{\eta_n}{\eta_{n-1}})E_{n-1}^+ e^{-\gamma_{n-1}d_{n-1}} + (1 - \frac{\eta_n}{\eta_{n-1}})E_{n-1}^- e^{\gamma_{n-1}d_{n-1}}}{2e^{-\gamma_n d_{n-1}}} \quad (3.9)$$

$$E_n^- = \frac{(1 - \frac{\eta_n}{\eta_{n-1}})E_{n-1}^+ e^{-\gamma_{n-1}d_{n-1}} + (1 + \frac{\eta_n}{\eta_{n-1}})E_{n-1}^- e^{\gamma_{n-1}d_{n-1}}}{2e^{\gamma_n d_{n-1}}} \quad (3.10)$$

The field of the  $n$ th layer is dependent on the layer of the  $n-1$ th layer and the field in the  $0^{\text{th}}$  layer (environmental medium) is

$$\begin{aligned} E_0^+ &= E_0^+ \\ E_0^- &= rE_0^+ \end{aligned} \quad (3.11, 3.12)$$

$r$  is the complex total reflection at the interface between the front passivation layer and the environmental medium. It is obtained from Eq. 3.2. The field in each layer can be obtained in order from the environment medium to the load and then the Poynting vector at each interface is:

$$P_n(x = d_n) = \text{Re}[E_n(x = d_n) \times H_n^*(x = d_n)] \quad (3.13)$$

$$A_n = P_{n-1}(x = d_{n-1}) - P_n(x = d_n) \quad (3.14)$$

We now verify the transmission line method by running a calculation of a planar thin film solar cell as shown in Figure 3.2a. The thickness of each layer is:  $t_1=50$  nm,  $t_2=400$  nm,  $t_3=150$  nm and  $t_4=100$  nm. The absorption in a-Si calculated by the transmission line method is compared with the result calculated by 3D numerical simulations. In Figure 3.3, the two methods agree very well.

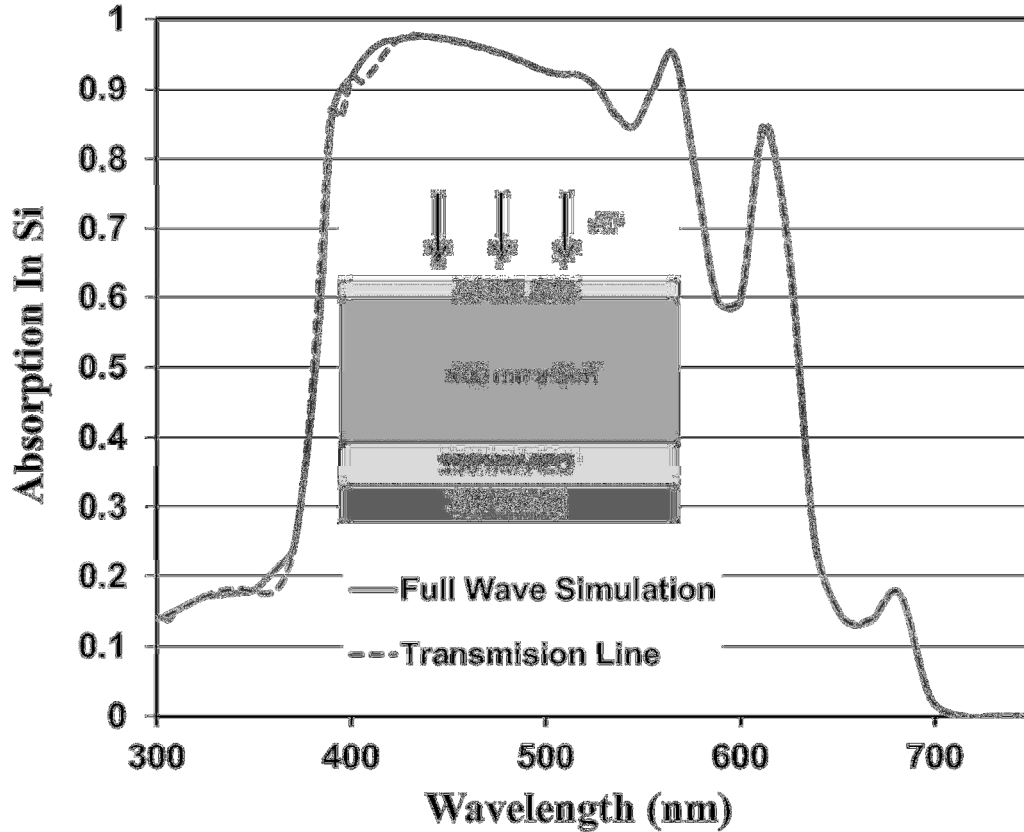


Figure 3.3 The comparison of the absorption of a TFSC obtained by a full wave simulation and the transmission line method. The transmission line method is as accurate as the full wave simulation but it is much faster.

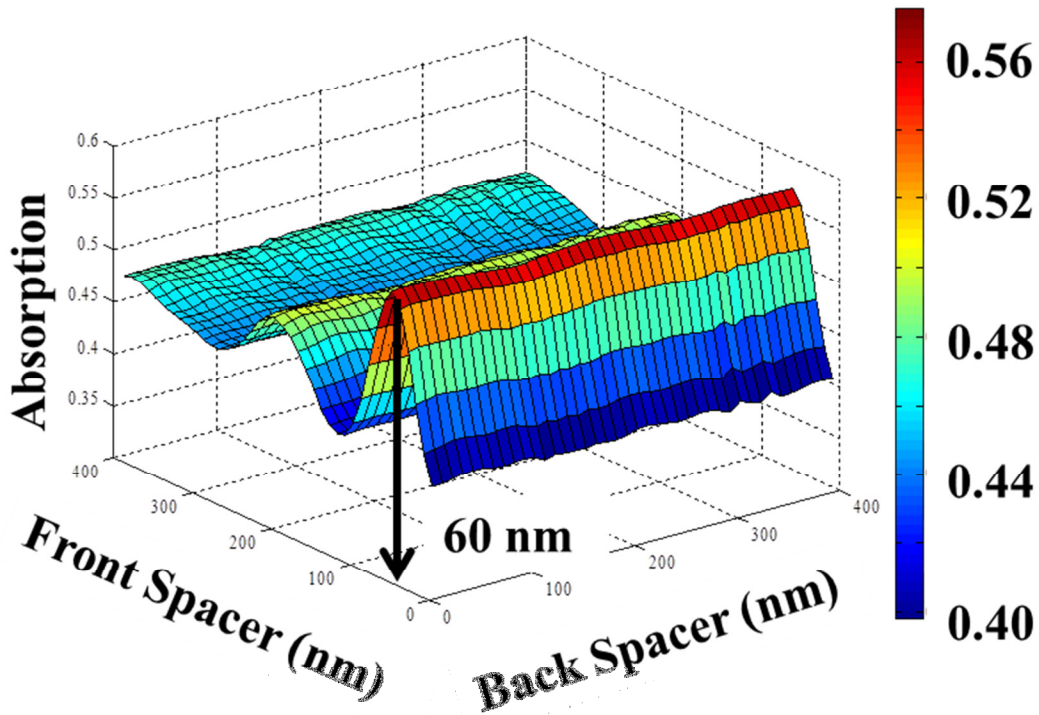
### 3.3 Optimization of the Anti-Reflection Layer

The target for the optimization is to achieve the maximal weighted absorption ( $A^*$ ) for a solar cell with 400 nm thick a-Si:H. The thickness of the back electrode is fixed to be 100 nm since the incident waves reflect at its front surface. The optimization considers light absorption in the a-Si:H layer from 300 nm to 700 nm. The weighting of light absorption is based on the AM 1.5G standard for terrestrial solar irradiance. The thickness of the front spacer ( $t_1$ ) and the back spacer ( $t_3$ ) is going to be adjusted based on the genetic optimization algorithm [45]. It is a

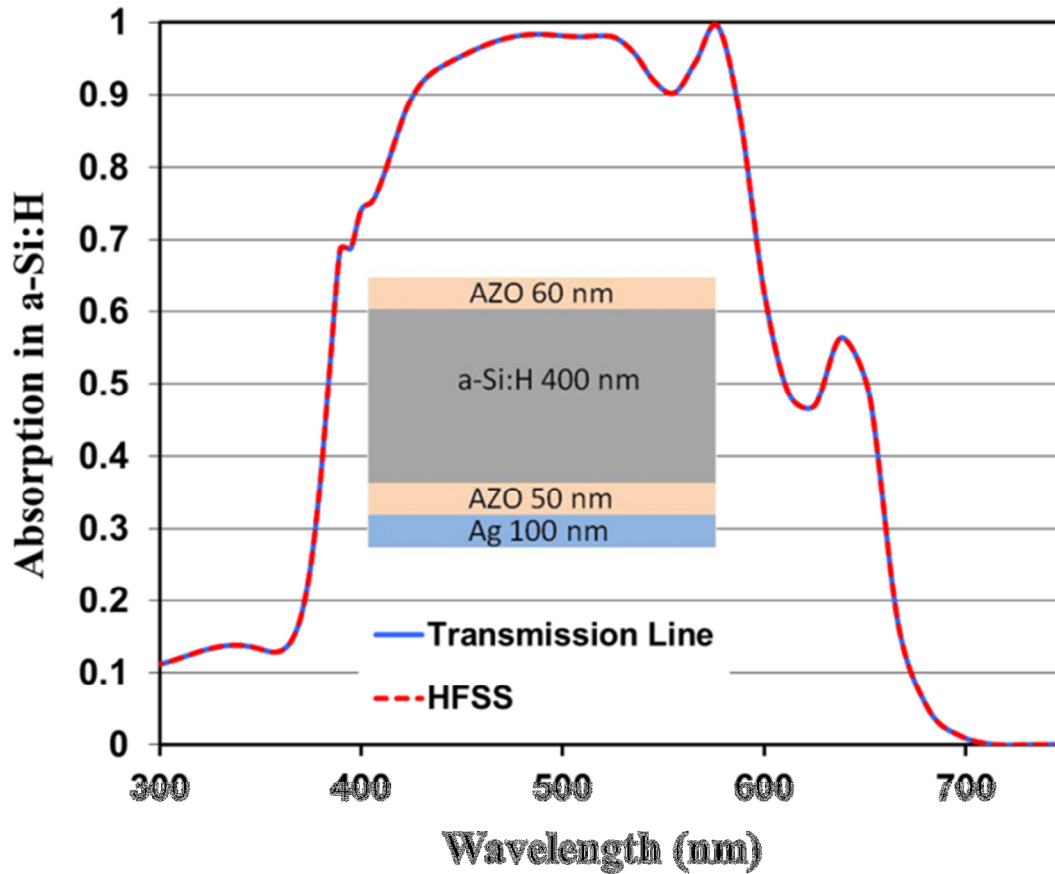
global optimization method so that the optimized results are not misled by local maximums, which are a problem for algorithms such as the Newton-Raphson method. The weighted absorption is defined as:

$$A^* = \frac{\int_{\lambda} A(\lambda)N(\lambda)d\lambda}{\int_{\lambda} N(\lambda)d\lambda} \quad (3.15)$$

$A(\lambda)$  is the light absorption at each wavelength and  $N(\lambda)$  is the incident photon density from the sun . The variation range of the thickness is set from 50 nm to 400 nm. A thick front passivation layer will cost more.



(a)



(b)

Figure 3.4 (a) The mapping of weighted absorption with respect to the thickness of the front passivation layer ( $t_1$ ) and the thickness of the back passivation layer ( $t_3$ ). (b) Light absorption in a-Si:H for the planar solar cell with  $t_1=60$  nm and  $t_3=50$  nm. The optimized weighted absorption over the spectrum is 57.4%. The result calculated by transmission line model is verified by numerical simulations.

A thin passivation layer exhibits a high resistance that is not good for carrier transport. In Figure 3.4a,  $t_1=60$  nm and  $t_3=50$  nm are the best set for the thickness of the front passivation layer and the back passivation layer. The optimization is performed considering the weighting effect of solar spectrum. We compare the results calculated by the transmission line method with

that of the finite element code HFSS and the perfect agreement verifies the transmission line calculation as shown in Figure 3.4b. We also find from Figure 3.4a that the absorption of solar cells is much more sensitive to the thickness of the front passivation layer than the back passivation layer. The weighted absorption is more dependent on the absorption at short wavelengths than long wavelengths. Since a-Si:H is able to absorb sufficient light at short wavelengths, the incident light hardly reaches the back passivation layer. Therefore, the impedance matching is mainly controlled by the front passivation layer. This observation provides with another advantage of putting plasmonic structures at the back end. As long as the thickness of the front passivation layer is optimized, plasmonic structures at the back end can enhance absorption at long wavelengths without degrading the absorption at short wavelengths.

## IV. Radiation by Plasmonic Structures

### 4.1 Plasmonic Structures and Antennas

Solar cells with coated with nanoplasmonic metal particles on top are able to achieve enhancement in light absorption [46-48]. At a plasmonic resonance, the energy from photons is converted into electron energy and then radiate as photons. In order to achieve light absorption at long wavelengths, the size of plasmonic particles needs to increase in order to red-shift plasmonic resonances. The dipole approximation for small particles is not valid for particles over the Rayleigh limit. As a result, the radiation nature by large particles is different from small particles.

The physics of electromagnetic radiation stands for different types of radiating elements. Hence, we are able to resemble any plasmonic structure with an antenna as shown in Figure 4.1.

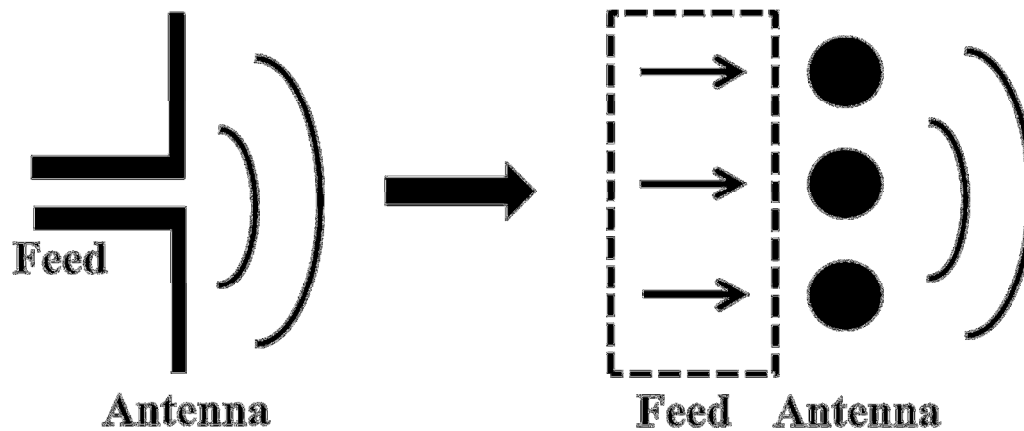


Figure 4.1 The analogy between a (dipole) antenna and a radiator made of plasmonic particles. The incident plane waves resemble the feed of an antenna. The plasmonic particles are radiating elements that are similar to any radiating antenna structure.

The performance of an antenna is related to two factors: 1) the amount of power received by an antenna from incident power; 2) the amount of power radiated from an antenna. These two factors are also the determinants for plasmonic structures. On one hand, incident photons are required to be absorbed by plasmonic structures. Plasmonic structures are able to absorb photon energy when the collective electron motion within the structure is in phase with the oscillation of incident field. The spectral location of this resonance is related to the geometry that confines electron motions. The radiation of photons from plasmonic structures is determined by the distribution of electrons on metallic surfaces. Firstly, no radiation will occur if the net charge on the surface of radiating elements is zero. The net charge on plasmonic structures at off-resonance frequencies is near zero. Secondly, despite the non-zero surface charges, the radiated power can be very small when the distribution of surface charges is improper.

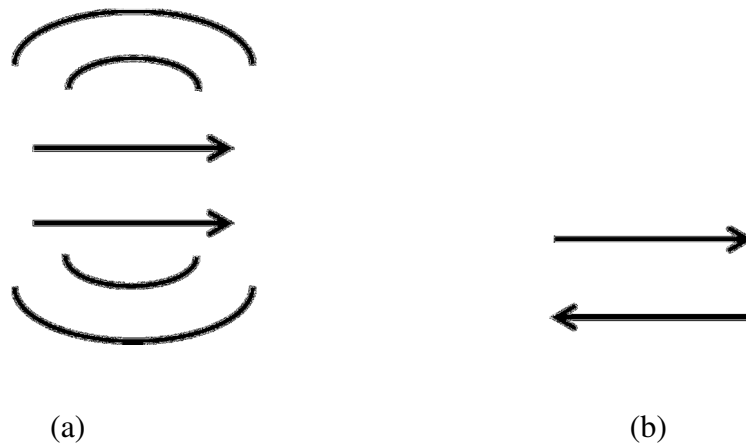


Figure 4.2 The schematics for (a) Radiating currents; (b) Non-radiating currents. In a radiating element, the two closely spaced currents are in the same direction so that the radiated waves by the two current flows add up. In a non-radiating element, the radiated waves by the two oppositely-oriented current flows cancel. As a result, the photon energy is trapped in plasmonic structures.



In Figure 4.2, the typical current flows in radiating elements and non-radiating elements are shown. In a radiating element, current oscillations at two closed spaced locations are in phase. Therefore, the radiated waves by each current flow add up with the radiated waves by others. In a non-radiating element, current oscillations are  $180^\circ$  out of phase. The resulting radiation will be zero since the radiated waves cancel each other. Instead of outward radiation, photon energy is trapped in plasmonic structures. The photon energy is transferred from the local electric field and the local magnetic field and vice versa. If there is not loss, this oscillation between capacitive energy and inductive energy will continue. If loss is present, the photon energy will be dissipated.

#### **4.2 Radiation by Plasmonic Particles**

Photon radiation from plasmonic structures is determined not only by the net surface charge but also by the distribution of charges. As mentioned before, the dipole approximation is used to describe the resonance of nanoplasmonic particles with their size below the Rayleigh limit. Positive and negative charges are separated, forming a dipole at the plasmonic resonance. Theoretical calculations show that small particles can absorb photon energy only in the short wavelength region. In fact, small plasmonic particles can radiate photon energy only at the short wavelength region, too.

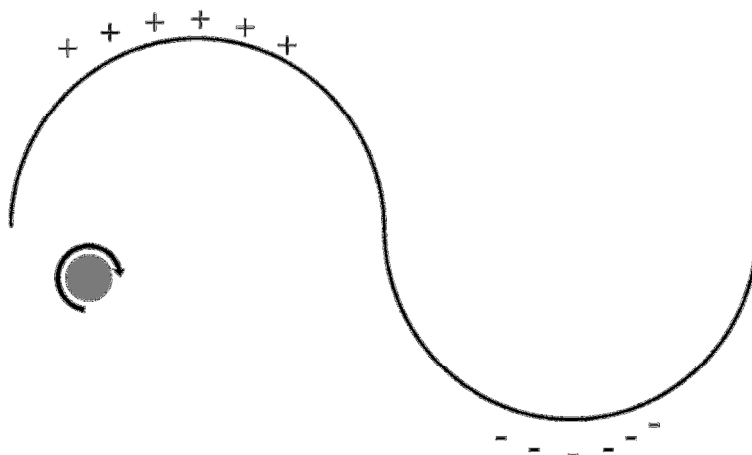


Figure 4.3 The size of a small plasmonic particle with respect to a period of a sinusoidal wave at long wavelength. There is nearly zero phase variation across the particle. Because of zero electrical potential across the particle, a closed loop current is generated equivalently.

In Figure 4.3, the nanoplasmonic particle is very small compared to the wavelength of light. As a result, the incident field has not phase variation across the particle. The resulting electric voltage across the particle is zero. The equivalent circuit will be a loop current around the particle. Since the particle is small, the loop current is made of closed spaced components that are oscillating  $180^\circ$  out of phase. Therefore, no energy is radiated at long wavelengths.

When the size of a particle is large enough, the incident field has phase variation across the particle. Non-zero electric voltage is generated across the particle. In this case, the resulting current along the metallic surface is not a closed loop.

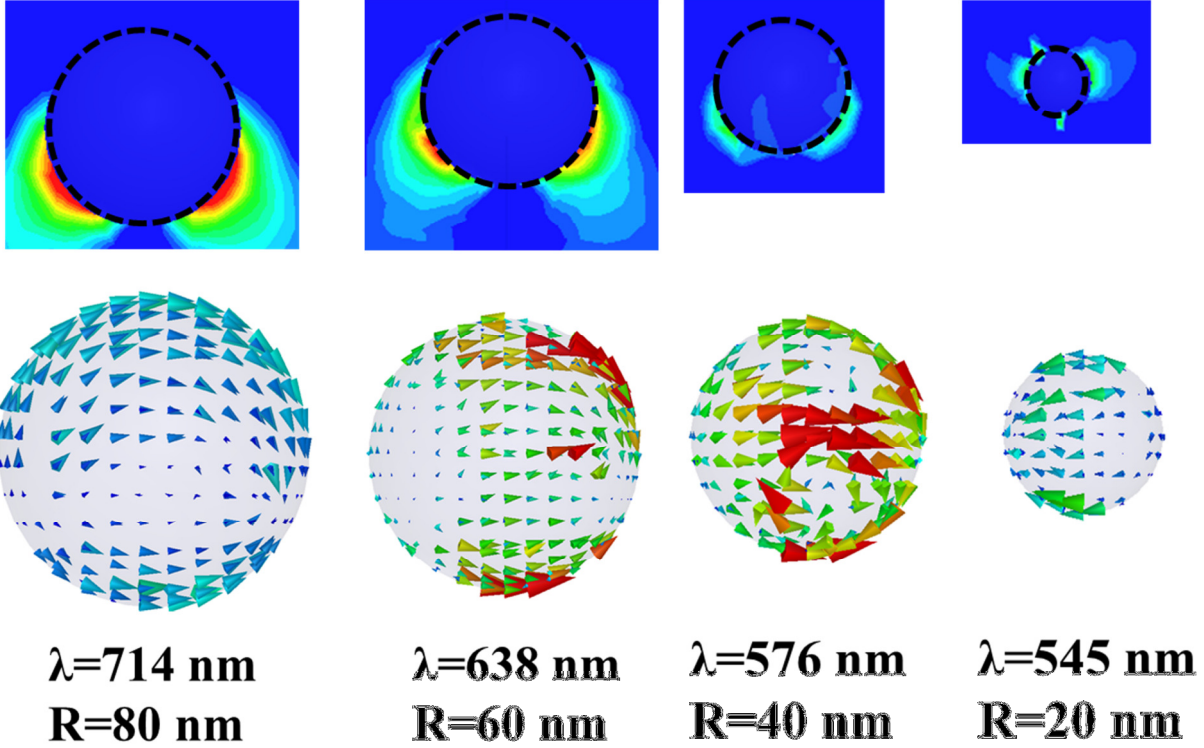


Figure 4.4 The localized electric field and the surface current on plasmonic spheres at the resonance of each one. The Au spheres are in  $\text{SiO}_2$  ( $\epsilon_r=2.1$ ).

Figure 4.4 shows the localized electric field and surface currents at the resonances of Au spheres with different values of radius. The maximal polarization at each resonance enforces charges to concentrate at the two ends of a sphere. As a result, the surface current on each sphere is flowing from one end to the other. Despite the similar patterns of localized field and surface currents, we observe that the density of surface current is stronger when the radius of the sphere is 40 nm and 60 nm. The resulting radiation from spheres with these two sizes is expected to be stronger than the other two.

In order to study the intensity of radiation by particles with different sizes, we normalized the radiation of each sphere by the base area of each one.

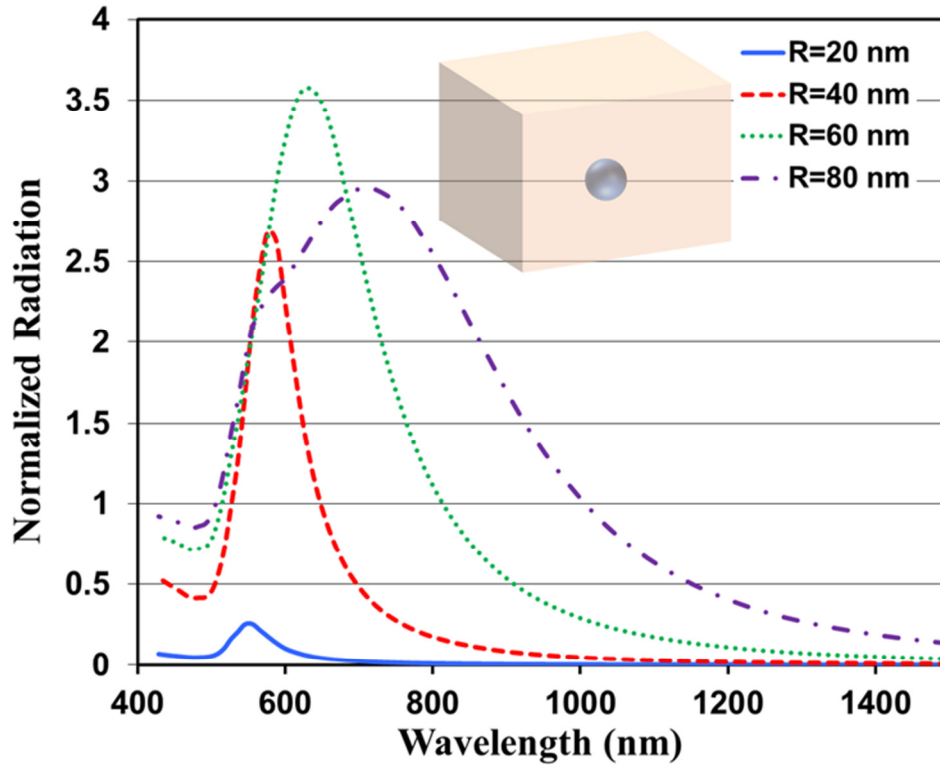


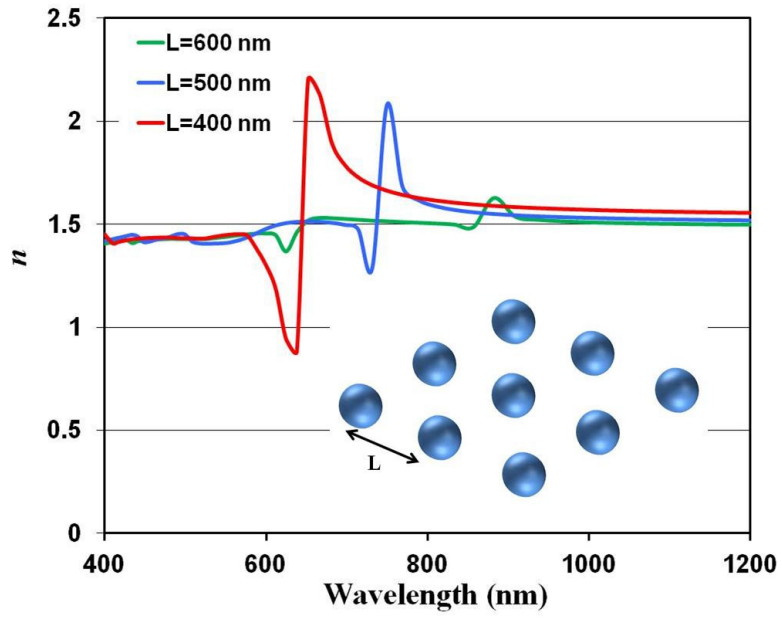
Figure 4.5 The normalized radiation power by a single Au sphere with different sizes. The Au spheres are in SiO<sub>2</sub> ( $\epsilon_r=2.1$ ). The normalized radiation power is calculated by dividing the radiated power from each sphere by the base area of each sphere. The incident electric field intensity is  $10^{10}$  V/m.

In Figure 4.5, the normalized radiated power is maximal when the radius of the sphere is 60 nm. Further increasing the size of plasmonic particles will result in weaker radiation.

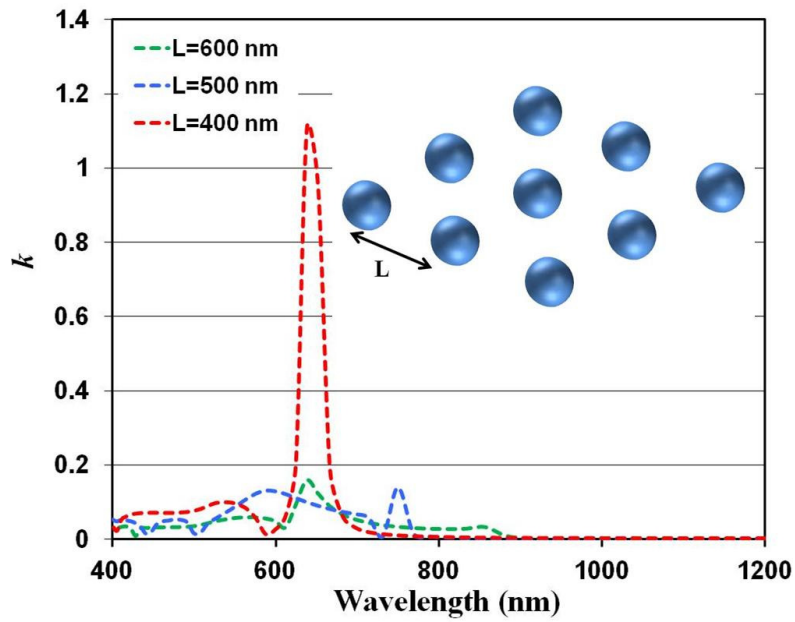
### 4.3 Particle Array and Near Field Coupling

There is no single particle in solar cells for light trapping. Instead, an array of particles is present in solar cells. When the spacing between particles is large, the resonance of each particle is independent. The radiation of the particle array is determined by both the array factor and the resonance of each particle.

In practice, the spacing between plasmonic particles in solar cells is in the order of the wavelength. In this case, near field coupling occurs and the resonance of each particle is not independent. We firstly study particle arrays with weak coupling effects. Au nanospheres are placed in SiO<sub>2</sub>. The radius of each nanosphere is 60 nm. The spacing between each two neighboring nanospheres varies from 400 nm to 600 nm. Considering 600 nm in free space is the reference wavelength, the wavelength in SiO<sub>2</sub> is 413 nm. Therefore, the variation of spacing in our study is from 1 to 1.5 wavelengths. In our study, plane waves are normally incident on the Au sphere array. We extracted the effective properties from the simulated reflectance and transmittance using the standard Nicolson-Ross-Weir method [49]. The plasmonic resonance is measured by the dispersion in the effective refractive index.



(a)



(b)

Figure 4.6 The refractive index of the Au sphere array at different spacing. (a) Real part; (b) Imaginary part. The Au spheres are placed in  $\text{SiO}_2$ . The radius of each sphere is 60 nm.

In Figure 4.6, the refractive index of the Au sphere array is shown. Although the size of each particle is constant, the wavelength for the plasmonic resonance is red-shifted with increasing spacing. The strength of the resonance, indicated by the amplitude of dispersion in the real part of refractive index, is reduced with increasing spacing. This is partly due to the less filling ratio of Au spheres at large spacing. The spacing does have impact on the plasmonic resonance.

When two particles are very close to each other, strong near field coupling effects will occur. Electrons on each particle start to interact with electrons on the neighboring particles. As a result, the current on each particle becomes quite different from a single particle. The radiation will also be different.

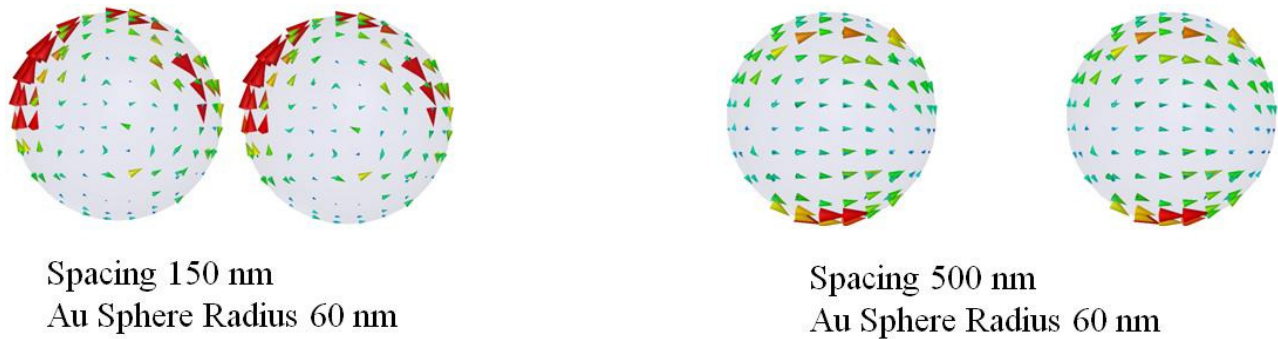
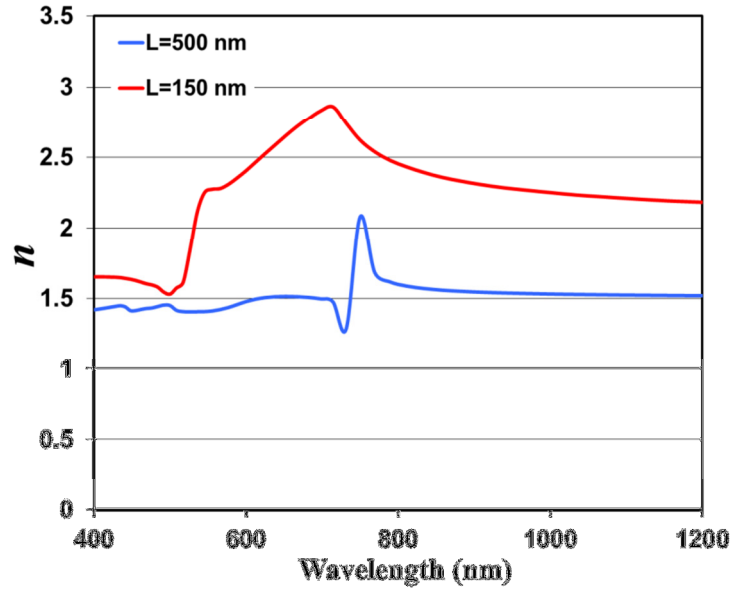
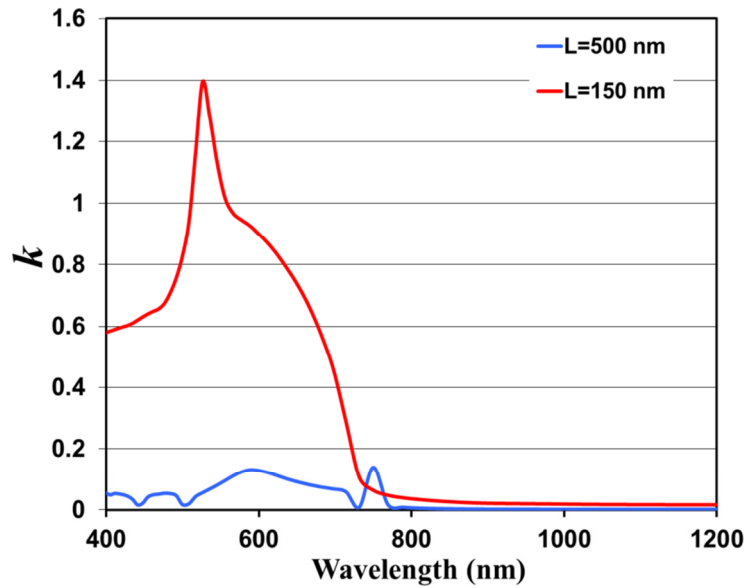


Figure 4.7 The surface current at the resonance ( $\lambda=638$  nm) of Au spheres with different spacings. The particles are in  $\text{SiO}_2$  ( $\epsilon_r=2.1$ ).

In Figure 4.7, the surface currents are shown on particles with two different values for the center to center spacing. When the spacing is 150 nm, the vertical components of the surface currents more or less cancel. This is not true when the spacing is 500 nm. The current flows are in the same direction when the spacing is 500 nm. The radiation by particles with 150 nm spacing is expected to be worse than particles with 500 nm spacing.



(a)



(b)

Figure 4.8 The refractive index of particles with spacings of 150 nm and 500 nm. (a) real part; (b) imaginary part. The loss in the particles with a 500 nm spacing is much smaller than particles with a 150 nm spacing.



In Figure 4.8, the refractive index of the particle arrays are shown. Two spacings are studied: 150 nm and 500 nm. The loss is much higher when the spacing is 150 nm. It agrees with our observation of surface currents in Figure 4.7. The non-radiating energy will be dissipated as heat.

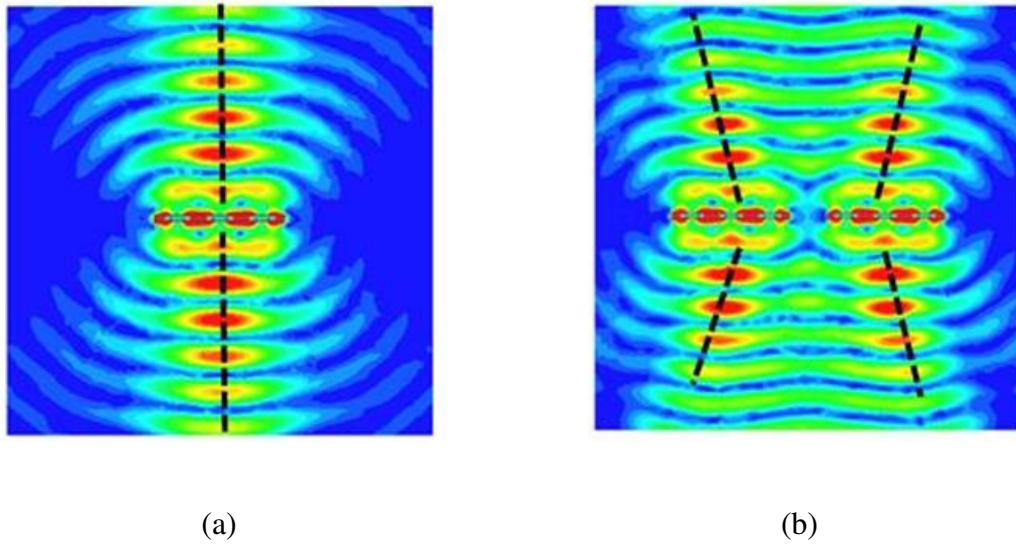


Figure 4.9 The radiated waves from two closely spaced Ag disks and a single silver disk. (a) single disk; (b) two disks with 500 nm center to center spacing. The side length of each Ag square disk is 400 nm.

Although Figure 4.8 shows the negative impact of coupling effects, it does not mean coupling effects are also bad. In fact, they may result in radiation patterns that can never be obtained by particle arrays with large spacing values. In Fig 4.9, the radiation patterns are shown for a single Ag disk and two closely spaced Ag disks. The coupling effects are able to direct the radiated light into oblique angles, which is good for light trapping purposes. The manipulation of

near field coupling effects is complicated. Practical designs would require full wave simulation to perform precise prediction of the coupling effects.

#### 4.4 Plasmonic Particles on Top of Solar Cells

Large particles resonate at long wavelengths. The scattered power intensity from large particles is stronger. Moreover, power scattering by large particles is more diffusive than small particles. Therefore, large particles are preferred for light trapping in solar cells. However, large particles can block the incident light when they are in the front end. When placing in the back end, large particles will result in a very thick back spacer layer.

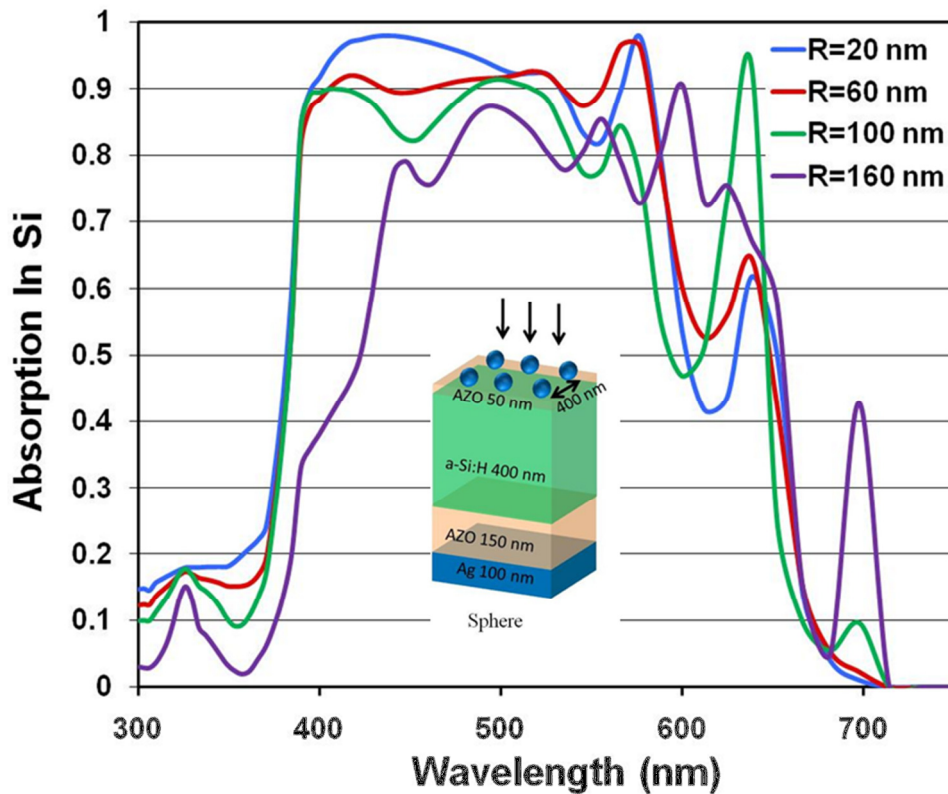


Figure 4.10 The spectrum of light absorption in the a-Si layer of a thin film solar cell coated with Ag nanospheres on top.

Fig 4.10 clearly shows that large metallic particles in the front end of solar cells block incident light and cause insufficient absorption at short wavelengths. In fact, these particles in the front end also scatter light into the active layer of solar cells. It is possible that the scattering effects may compensate the negative effect of blocking light.

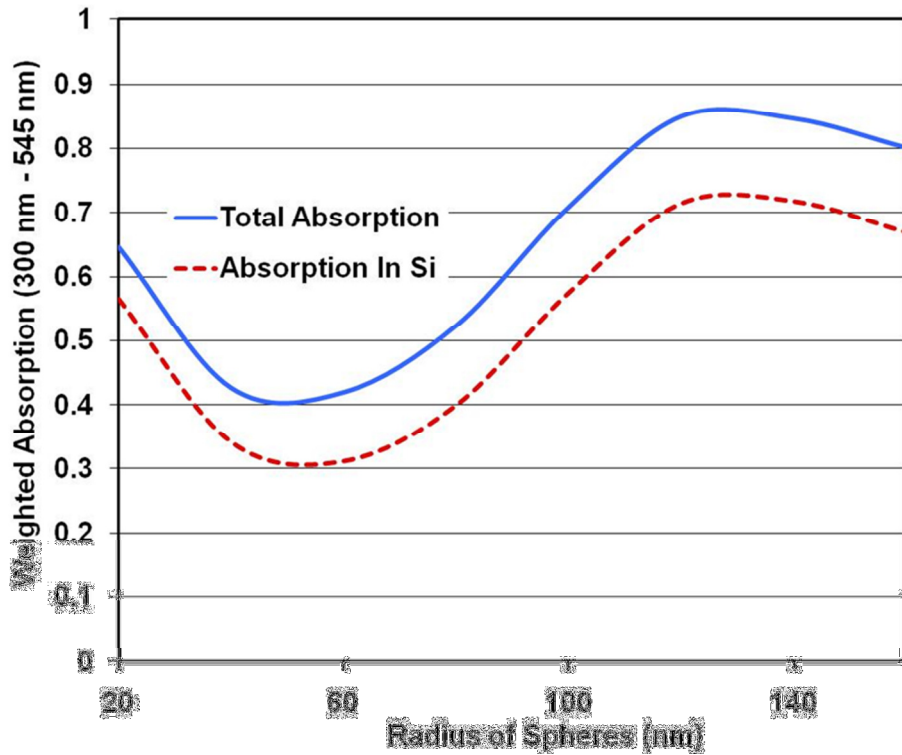


Figure 4.11 The absorption at short wavelengths of Ag spheres on top with respect to the radius of each sphere. The spacing is 400 nm.

Figure 4.11 shows the weighed absorption in the a-Si of TFSCs with respect to the radius of nanospheres. AM 1.5G standard is used and the absorption is weighed from 300 nm to 545 nm. The surface area blocked by Ag spheres is increased when increasing the size of each nanosphere. The weighed absorption, however, does not decrease accordingly. Instead, the maximal weighed

absorption occurs when the radius of nanospheres is 120 nm. The maximal absorption (0.72 in a-Si) is even higher than the absorption obtained when the radius of nanospheres is 20 nm (0.56 in a-Si). The surface area blocked by nanospheres of 20 nm radius is negligible. It is clear from the study that the scattering effects can compensate the negative effect of blocking light. Furthermore, we believe that properly arranged metallic particles in the front end of solar cells will perform better than the case without particles.

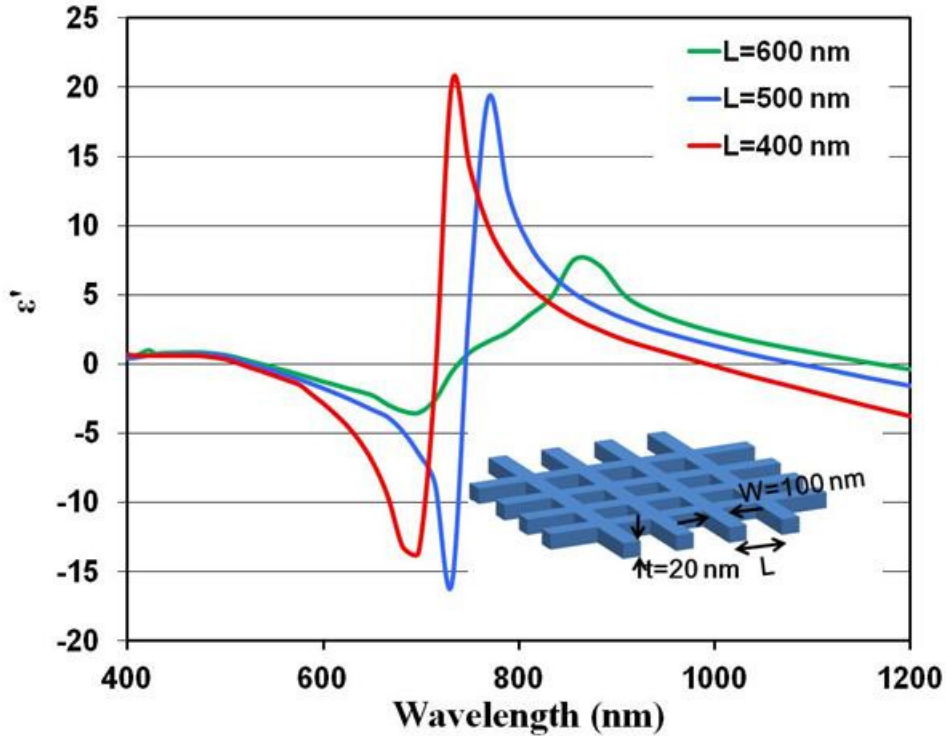
## V. Fishnet Structures for Enhancing Light Absorption in Solar Cells

### 5.1 Background

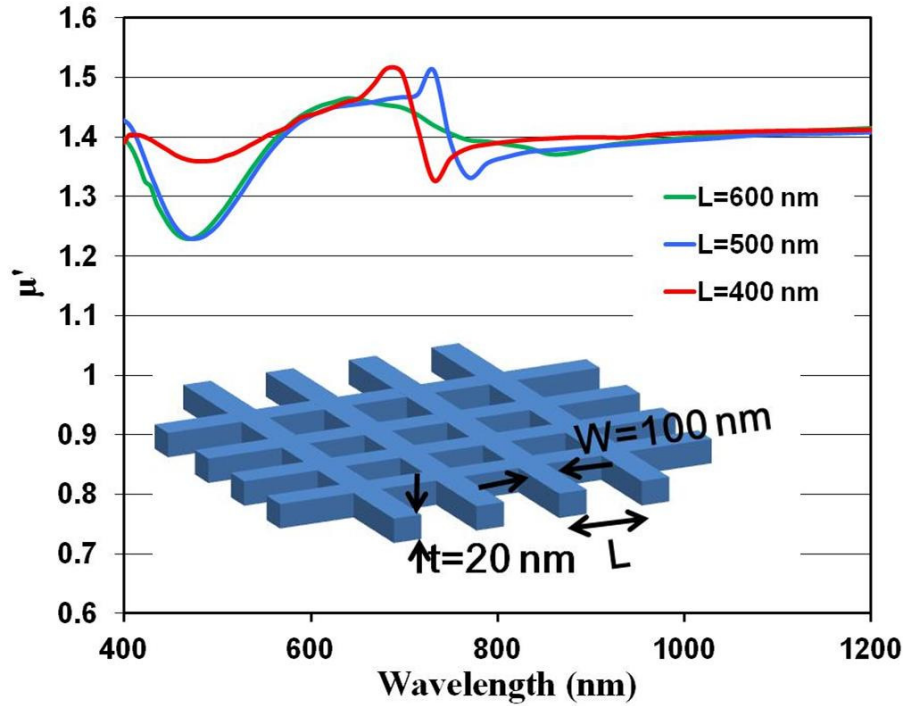
Large particles have to be used for light trapping in solar cells. The large size of particles also increases the overall thickness of solar cells. It is better to find plasmonic geometries that are able to tune their resonances without resulting in bulky shapes. Planar structures, such as gratings [50-52] and photonic crystals [53], have been proposed to enhance solar cell efficiency. Compared to bulky metal particles, planar structures occupy less area and are easy to integrate. They can even be integrated with the electrodes of a solar cell to fulfill the functions of light trapping and carrier collection simultaneously [54]. In this paper, we introduce a fishnet metastructure for increasing light absorption in thin film a-Si:H solar cells. A fishnet structure is in the category of metamaterials in which geometry is exploited to tailor the resonance frequencies. Compared to previously reported planar structures, a typical metamaterial structure works like an LC resonator and the plasmon resonance strongly depends on the geometry and also on the material properties of the metal and the embedding layer. Overall structure size, and the detailed layout and orientation are also very important parameters in determining the resonance. For solar cells, we wish to lower the light reflection at the front surface of the solar cell to achieve high absorption. An impedance matching condition is required for low reflection. In terms of tuning the effective impedance of the medium, metamaterials have very high flexibility because the plasmon resonance can be easily controlled by the metal structure. The fishnet structure was first proposed for the purpose of creating negative index materials in the near infrared band [55, 56]. A multilayer stack of fishnets can be used to excite both electric and magnetic plasmons. The wire array parallel to the incident electric field contributes to the generation of electric plasmons and the magnetic plasmons are generated by the inter layer

coupling between wires parallel to the incident magnetic field [56]. Using an effective circuit model of the fishnet [57], as well as full wave models [58], the resonance of the fishnet can be related to the width of the wire, the thickness of wire and the material properties. We observe that metamaterial structures are sub-wavelength in size at resonance.

In this section, only a single layer fishnet structure is used in order to reduce the cost of fabrication. Therefore, only electric resonance is expected to excite.



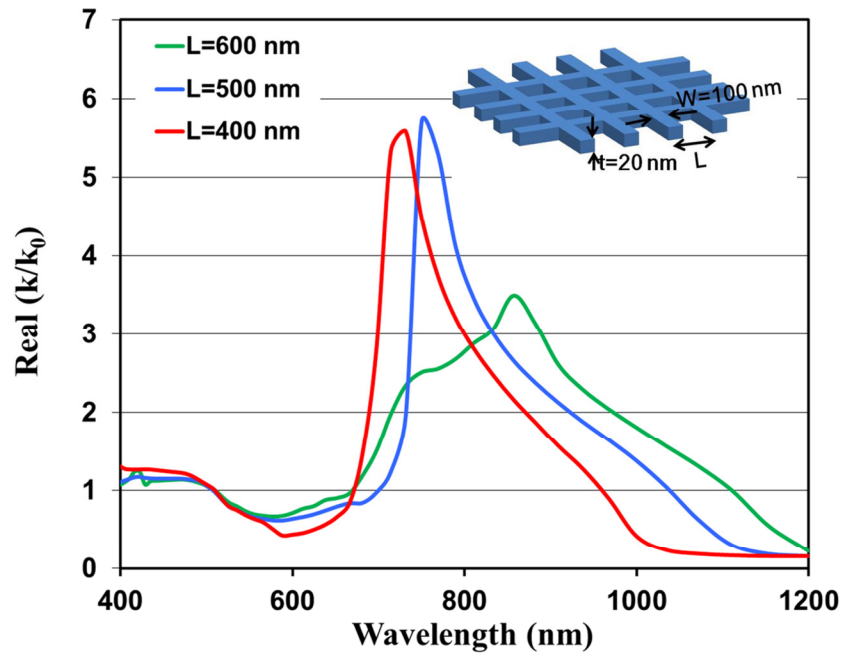
(a)



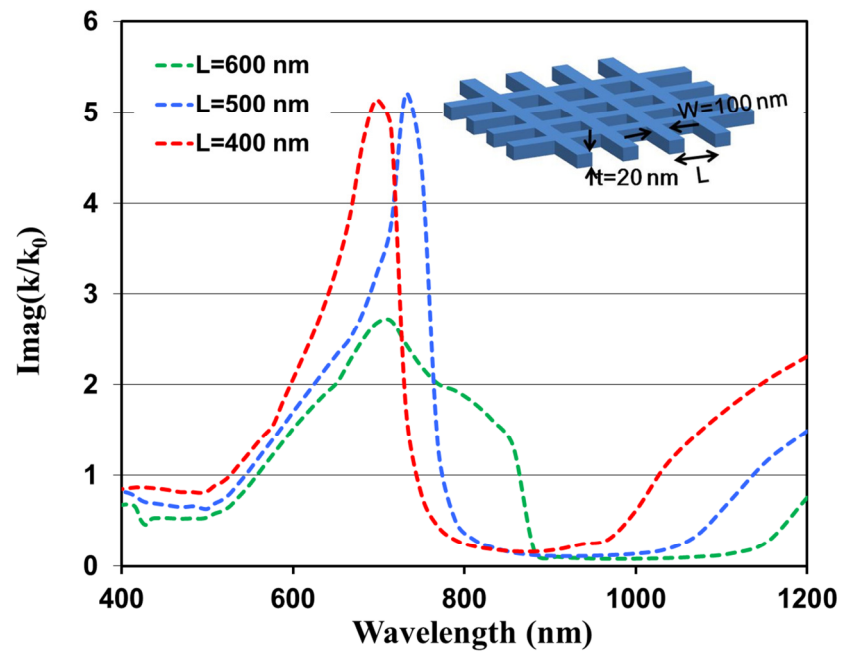
(b)

Figure 5.1 The real part of the effective permittivity and effective permeability of Au fishnet with different spacings. The thickness of fishnet is 20 nm and the line width is 100 nm. The Au fishnet is placed in  $\text{SiO}_2$  whose dielectric constant is set to be 2.1.

The effective permittivity and permeability is shown in Figure 5.1. The dispersion of permittivity shows a Lorentz-like behavior, indicating that an electric resonance is excited. Although no magnetic resonance occurs, the effective permeability at off resonance wavelengths is around 1.4. The resonance wavelength is shifted to long wavelength with increasing spacing. However, the strength of a fishnet resonance becomes weaker with increasing spacing. We studied the dependence of a fishnet resonance on spacing, line width and line thickness as shown in Figure 5.2.

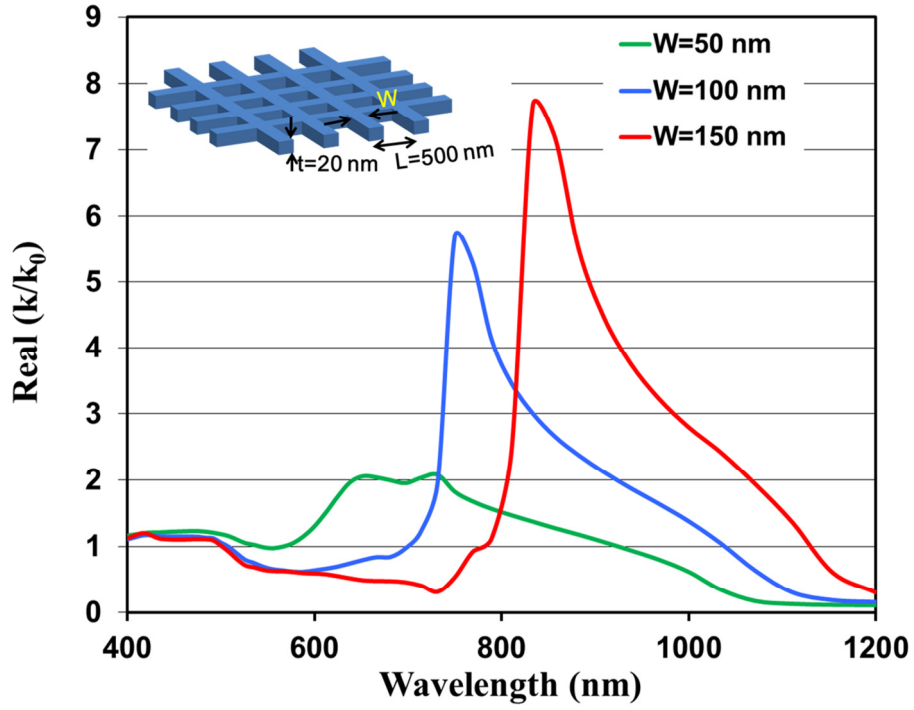


(a)

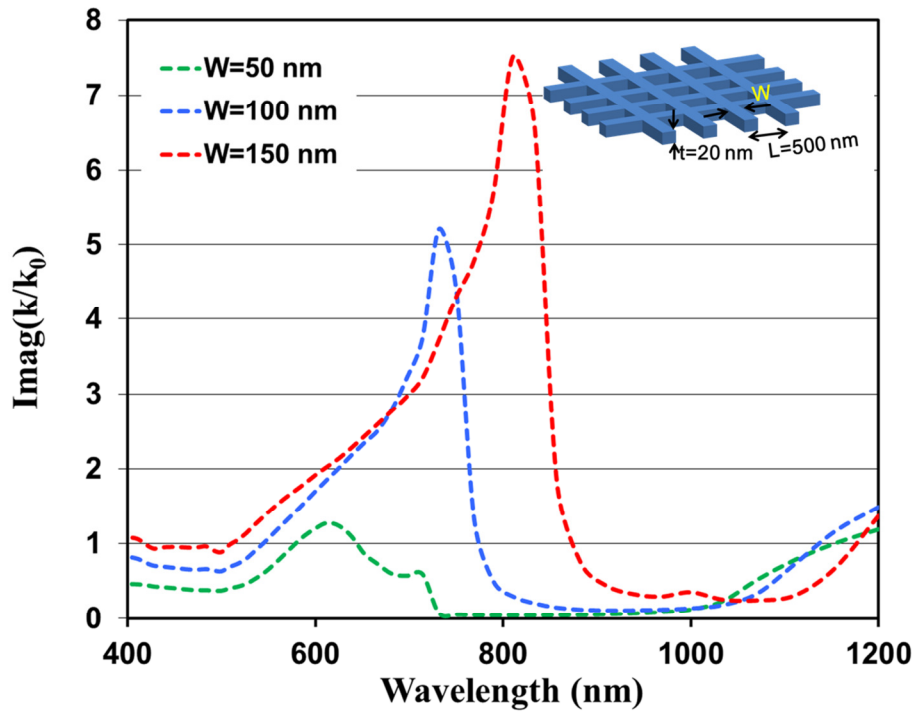


(b)

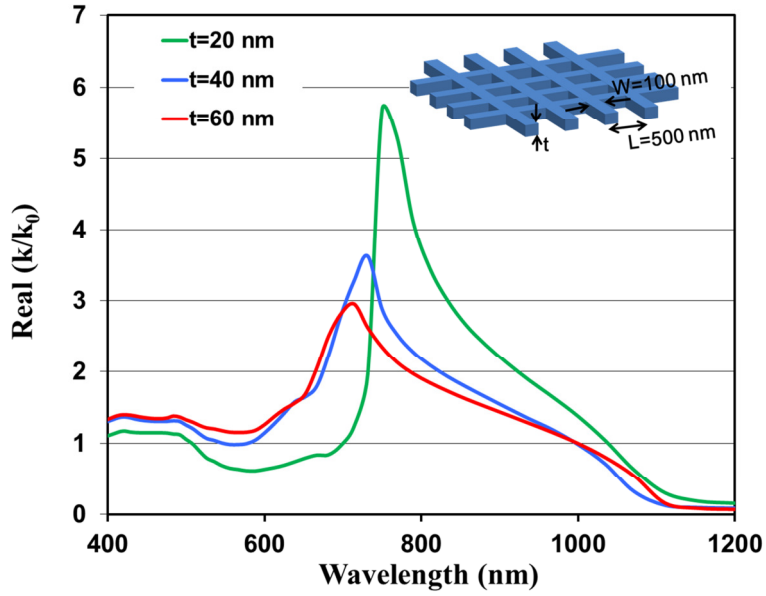




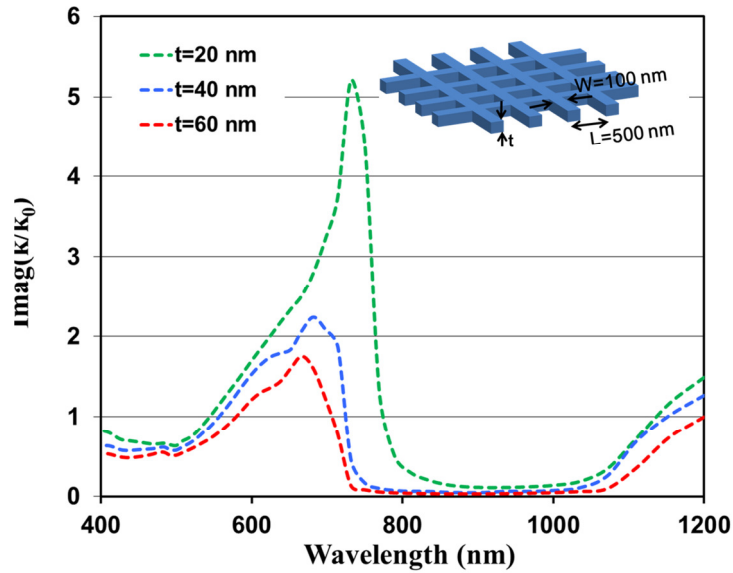
(c)



(d)



(e)



(f)

Figure 5.2 The real and imaginary parts of the effective wave number of the fishnet. (a) and (b) show the wave numbers with different spacing. (c) and (d) show the wave numbers with different line width. (e) and (f) show the wave numbers with different line thickness. The Au fishnet is placed in  $\text{SiO}_2$  whose dielectric constant is 2.1.

The wavelength and the strength of a fishnet resonance are related to geometrical parameters. We may conclude from Figure 5.2 that a stronger fishnet resonance will occur with a smaller spacing, a wider line and a thinner line. However, a strong dispersion in the resonance region also results in a higher loss at the resonance. A proper design of fishnet in solar cells is a tradeoff between resonance strength and loss.

## **5.2 Design of Fishnet for a-Si:H Thin Film Solar Cells**

We embed the fishnet in the back passivation layer (AZO) of a thin film solar cell as shown in Figure 5.3. The 20 nm thick fishnet is 30 nm away from the a-Si:H and 50 nm away from the back electrode (Ag). Assuming infinite periodic extensions, we studied the electromagnetic response of a unit cell of the solar cell in simulations. The finite element commercial code HFSS is used for full wave simulations. Putting the metastructure layer in the back passivation layer avoids the possible blocking of light by the metal layer in short wavelength region. The incident light can excite only electrical resonances in the fishnet wires for two orthogonal polarization directions along the wires. The widths of the crossing wires are designed to be equal so that the fishnet response is more isotropic.

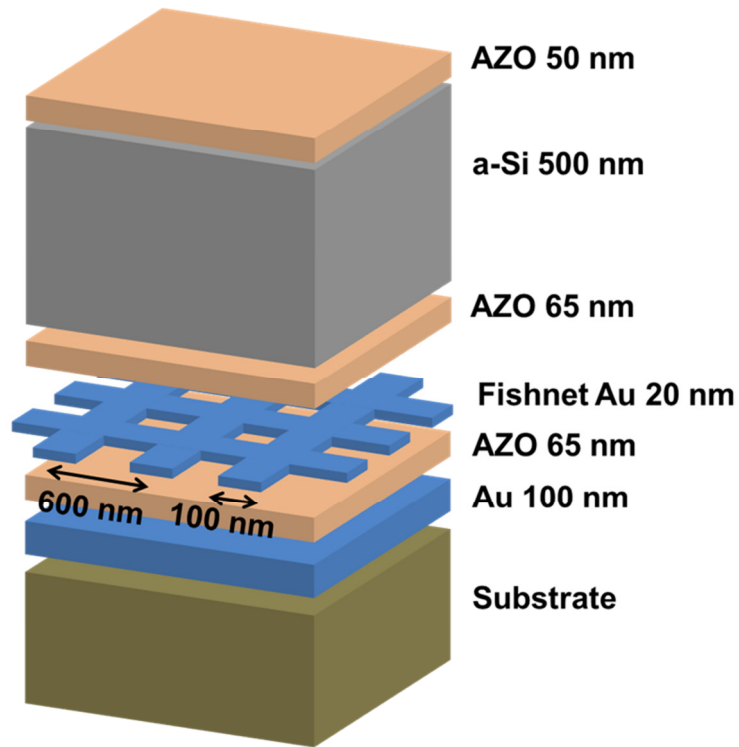


Figure 5.3 The schematic of an a-Si:H solar cell with 20 nm thick Au fishnet embedded in the back spacer. The line width of fishnet is 100 nm and the center to center spacing of the fishnet is 600 nm. The thickness of a-Si:H is 500 nm. The whole cell is standing on a substrate. A 20 nm thick bump in the back spacer layer is considered due to the fishnet structure.

Both the front and back passivation layers are made of AZO. The embedded fishnet effectively increases the conductivity of the back passivation layer. The a-Si:H layer is chosen to be 500 nm thick for acceptable performance of carrier transport. Moreover, 500 nm of a-Si:H is able to absorb sufficient light at wavelengths shorter than 600 nm. Our model in simulation also includes a 20 nm bump at the bottom the a-Si layer. This bump will be present in practice.

### 5.3 Light Absorption Enhancement by Fishnet

Firstly we consider linearly polarized plane waves normally incident on the solar cell. The optical properties of n type, p type and intrinsic Si are the same so that they can be treated as a homogeneous material. The fishnet is designed to excite a resonance in the band gap region (from 650 nm to 700 nm) where the light absorption of 500 nm a-Si:H is very weak. Enhancing light absorption in this region is able to take advantage of the high conversion efficiency near the band gap of a-Si:H. Moreover, the solar spectrum has highest density in this region. The light absorption of the thin film solar cell model using HFSS finite element simulation is shown in Figure 5.4.

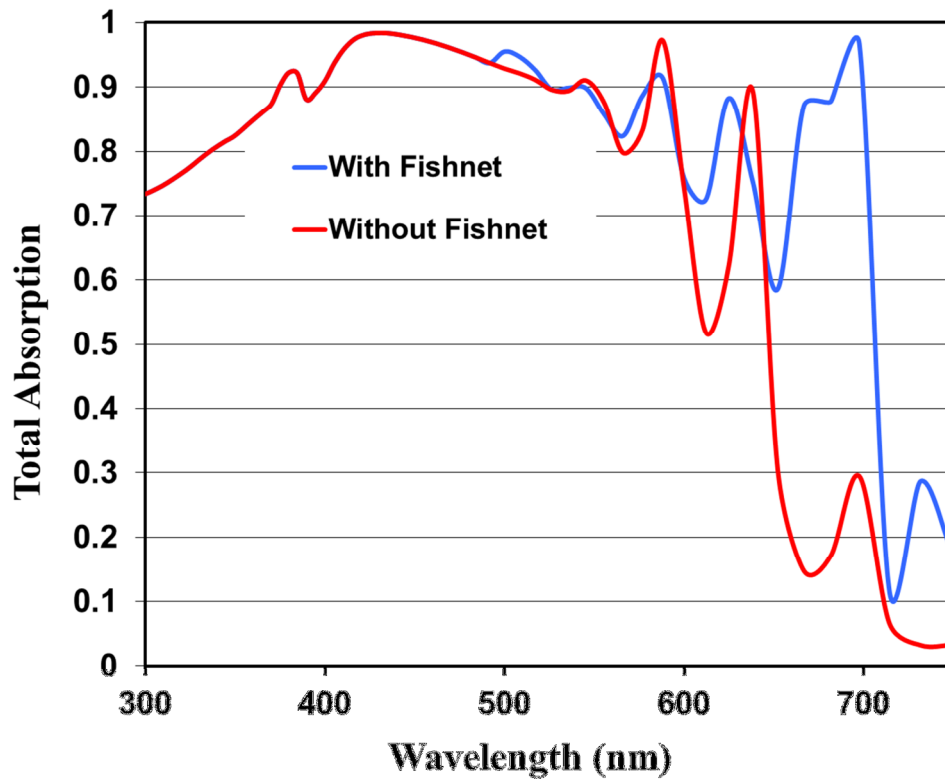


Figure 5.4 The total absorption of the solar cell with and without the embedded fishnet.

The fishnet exhibits its unique plasmon resonance at 697 nm. At off-resonance frequencies, incident light will go through the fishnet holes and be reflected by the back electrode. The fishnet has no interaction with the incident light and the light absorption of the solar cells with and without the fishnet is the same.

There is enhanced constructive interference in the a-Si:H region at the fishnet resonance as shown in Figure 5.5. Surface charges confined by the fishnet move in phase at resonance. The scattered surface waves by the fishnet and the incident wave interfere constructively at the locations where the field is strong. Compared to the same thin film cell without fishnet, the field localization within the a-Si:H layer of the cell with fishnet is stronger and the localization pattern is irregular. The strong field localization indicates a high absorption within the a-Si:H layer.

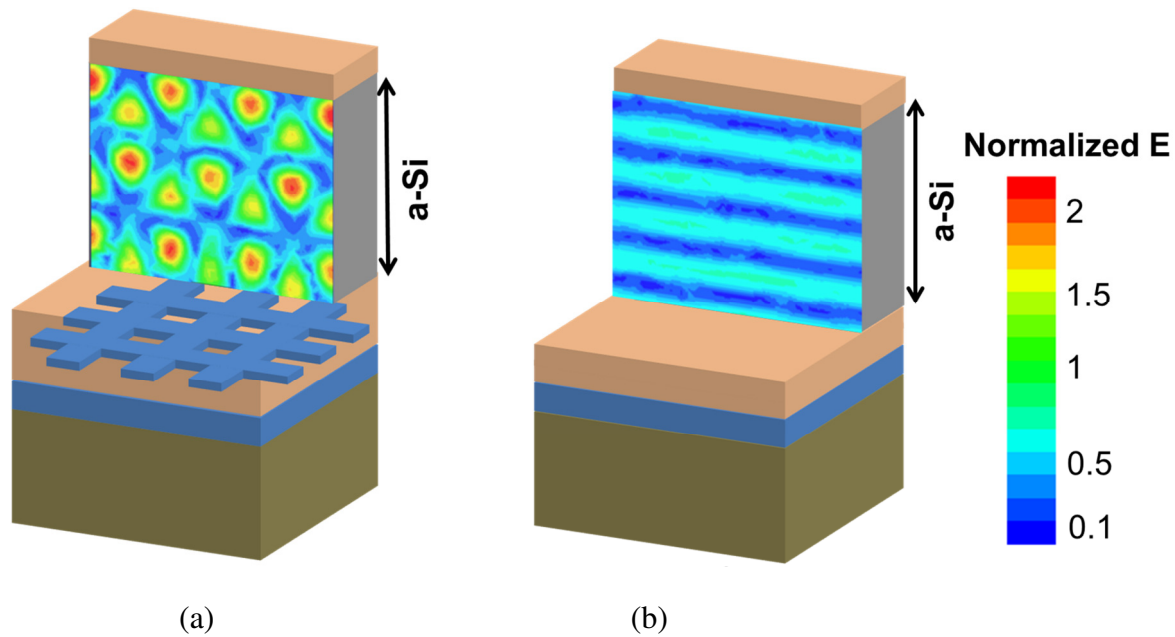


Figure 5.5 The localization of electric field within the a-Si:H layer. (a) With fishnet; (b) Without fishnet.

In order to estimate the performance of a solar cell, only light absorption in a-Si:H is useful. As discussed before, a plasmonic resonance will result in loss in the metallic structure. There are other minor sources of loss from the rear reflection and the passivation layers. The loss cannot contribute to photocurrent but they are included in the total absorption of the solar cell. It is, therefore, necessary to sort out loss from the useful absorption in the a-Si:H layer. We calculated the absorption  $A_{Si}$  in the a-Si:H layer according to Poynting's theorem:

$$A_{Si} = \frac{1}{2} \int_{Si} \frac{2\pi c}{\sqrt{\epsilon'} \lambda} \epsilon'' |E|^2 dV \quad (5.1)$$

$c$  is the velocity of light in free space,  $\lambda$  is the free space wavelength,  $\epsilon'$  and  $\epsilon''$  are the real and imaginary part of the permittivity of a-Si:H.  $|E|$  is the magnitude of the local electric field in the a-Si:H. We obtained the local field from the simulations and then integrated this value over the volume of the a-Si:H.

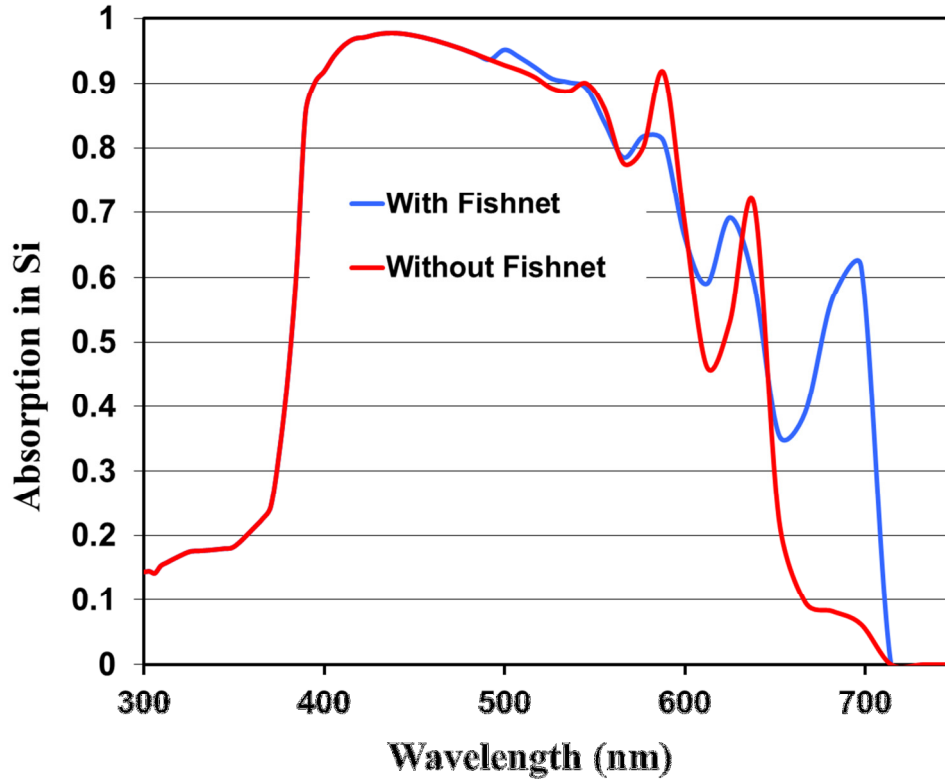


Figure 5.6 Light absorption in the a-Si region of the solar cells.

In Figure 5.6, we show the absorption within the a-Si:H for the cells with and without fishnet. At 697 nm where the plasmon resonance occurs, light absorption within the a-Si:H layer is 62% while the total absorption is 98%. Loss in other layers accounts for 37% of the total absorption. Compared to the cell without fishnet, 10x enhancement of light absorption within the a-Si:H layer is made at the plasmon resonance of fishnet. The same solar cell without fishnet only has 6% light absorption in a-Si:H. The loss is majorly within the fishnet layer due to enhanced field localization. This loss, however, cannot be avoided. Firstly, the electric field has a tendency to localize at the metal-dielectric interface because of the discontinuity; secondly, the in phase motions of free electrons at plasmon resonance create standing wave patterns at the metal surface, leading to strong field localization.



The losses away from the resonance region (from 600 nm to 700 nm) are very small and nearly all the light absorption results in carrier generation. High absorption in a-Si:H is maintained down to 400 nm where the absorption coefficient of AZO increases sharply. Excluding the reflected light, incident light suffers strong attenuation in the front passivation layer and the remaining light is absorbed by a-Si:H. This disadvantage can be overcome by optimally designing the front passivation layer. A solar cell of high efficiency requires its passivation layers of high conductivity to reduce loss in carrier transportation. The fishnet improves the conductivity of the back passivation layer.

Table 5.1 The calculated short circuit current

	Short Circuit Current (mA/cm <sup>2</sup> )
With Fishnet	15.43
Without Fishnet	13.62

Based on the numerical computation of light absorption, we calculated the short circuit current of the solar cell using the following formula:

$$J_{sc} = \int_{\lambda} eA(\lambda)\Phi_0(\lambda)d\lambda \quad (5.2)$$

where  $e$  is the charge of an electron,  $A(\lambda)$  is the frequency dependent light absorption in silicon as calculated from the full wave simulation and  $\Phi_0$  is the number of incident photons per wavelength. AM1.5G is used for the solar spectrum illumination. Several assumptions are made for the current calculation: (i) IQE=100% over the whole spectrum; (ii) there is no light absorption in silicon above its band gap, which is 700nm; (iii) light absorption below 300nm

does not contribute to photocurrent generation. Only the absorption in a-Si:H is included for photocurrent calculation. Because there is no recombination considered in the calculation, all absorbed photons contribute to current generation. The calculated short circuit current is shown in Table 5.1. We achieve 13.29% enhancement in  $J_{sc}$ .

## VI. Temperature Dependence of Plasmonic Resonances

### 6.1 Background

Heating is an important issue for solar cells. The temperature of solar cells under the exposure of sunlight increases very quickly. The performance of carrier transport in solar cells degrades at high temperature. In this dissertation, we discussed using plasmonic structures to enhance light absorption. The plasmonic resonance of a structure is very sensitive to the geometry of the structures and the optical constants of materials. As a result, the heating of solar cells not only affects carrier transport, but also affects the performance of light trapping. It is, therefore, necessary to study the temperature dependence of plasmonic resonances.

In this section, we study the temperature dependence of quasi-plasmonic structures at microwave frequencies. The acquisition of microwave samples is much easier than optical samples. The Split Ring Resonator (SRR) is selected for our study. The physics of SRR resonances is the same as the plasmonic structures we studied before in this dissertation. The resonance of SRRs is also due to the collective motion of electrons in confined structures. A big difference between microwave quasi-plasmonics and optical plasmonics is the electrical properties of metals. Metals are good conductors at microwave frequencies and their real parts of permittivity are considered as negative infinity. As a result, the intensity of field penetrating into metals at microwave frequencies is nearly zero. The mobility of electrons in metals is much higher at microwave frequencies than at optical frequencies. Despite this difference, the physics of microwave SRRs and optical plasmonic structures is the same. It is, therefore, valid to apply the study on microwave SRRs to optical plasmonic structures.

SRRs have been found to have potential applications in antennas, filters, phase shifters, etc. These designs may require stable device performance under extreme temperature conditions (high and low). Because the bandwidth of metamaterial resonances is narrow (high Q), even a small shift in resonance will make a big difference in device performance. For example, an SRR-based antenna usually has a very narrow bandwidth ( $< 5\%$ ), and will have poor radiation efficiency if it is subject to any conditions that shift the resonance frequency. A 3% shift in resonance frequency will be sufficient to filter out the frequency that the antenna is designed for. The resonances are very sensitive to parameters like SRR dimensions and material properties that can be affected by variations in temperature. Therefore, it is necessary to investigate whether metamaterials still perform as designed under different temperature conditions. In addition, metamaterial structures absorb energy at resonance, and a large portion of the absorbed energy will be dissipated as heat. Even if the devices are operating in a stable temperature environment, the dissipated heat may increase the temperature of the devices due to high field localization [59]. The power absorption and heating characteristics of metamaterials have been proposed for use as the sensing element for bolometers [59]. All such applications will require a detailed analysis of the temperature dependence of metamaterial resonances.

The purpose of this study is to understand how metamaterial resonances are affected by large fluctuations in temperature, but also giving a guideline in designing metamaterial based devices and to identify the material and geometric parameters that are most critical in effecting the frequency change. This will be a useful guideline in device/material designs that have to be stable under variable temperature conditions. In this section, we investigate experimentally for the first time the temperature dependence of metamaterial resonances. Previous experimental and theoretical studies have shown that the SRR resonance depends on the polarization of the

exciting electromagnetic field with respect to the orientation in the gap of the SRR [60, 61]. If the gaps of a periodic distribution of SRRs are perpendicular to the exciting electric field, it has been shown that the resonance is magnetic giving rise to a highly dispersive effective magnetic permeability and even negative permeability in the resonance region. If on the other hand, the gaps are parallel to the electric field, the resonance is electrical in nature and leads to a highly dispersive dielectric permittivity. In this experimental study, we also investigate the temperature dependence of the response to different types of polarization. In [60], it has also been shown that a distribution of randomly oriented SRRs gives rise to both electric and magnetic resonances and near perfect absorption (>95%) and we study the temperature behavior of such materials also.

Table 6.1 The permittivity of substrate at 10GHz

	$\epsilon'$	$\epsilon''$
FR4*	4.225	0.045
DuPont 951*	7.413	0.037
Rogers TMM13i*	12.668	0.053
Rogers TMM13i**	12.995	0.052

In Table 6.1, we have compared the complex permittivity of FR4 and Dupont 951 with other microwave substrate materials such as Rogers TMM13i series at 10 GHz. While FR4 is slightly more lossy than Rogers materials, it is an order of magnitude less expensive. It may be noted that the stripline method used by Rogers will not yield the same results as the free space method that we have used. The thermal expansion module in the ANSYS finite element software was used to obtain the thermal expansion behavior of the SRRs. The temperature dependence of the permittivity, electrical conductivity and the geometrical parameters of the SRR as a function

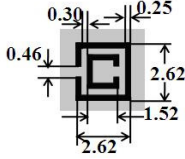

of temperature were input to the Ansoft HFSS full wave simulator to obtain the microwave response (S-parameters) as a function of frequency at a specific temperature. The simulation was repeated for different temperatures. The comparison between our experimental measurements and numerical simulation is in good agreement.

From a microscopic point of view, metamaterial resonances derive from the oscillations of free electrons in the metal structure. A detailed physical model to explain the observed experimental behavior with rising temperature should include a consideration of changes in free electron motions with temperature. However, we have considered only macroscopic effects since these provide more useful guidelines for device and material designs using metamaterials.

## **6.2 Metamaterial Samples**

Several types of metamaterial samples have been used in the experimental study including periodic and random metamaterials as well as thin wire media. The resonant metallo-dielectric structure is chosen to be a split ring resonator (SRR) since it is a very well-studied geometry. Our samples are Cu SRRs deposited on an FR4 dielectric substrate using wet etching lithography and Ag SRRs deposited on a DuPont 951 ceramic substrate using screen printing and subsequent sintering at 700°C. In Table I, the thickness and material properties of the substrate materials are listed. The SRRs were designed to have a resonance around 10 GHz (X-band) since this is a commonly studied frequency band and used in many applications.

Table 6.2 SRR Orientations and Dimension for FR4 Based Samples

	Gap orientation <i>w.r.t.</i> incident field	Dimension (mm)
SRR <sub>  </sub>	Parallel	
SRR <sub>⊥</sub>	Perpendicular	
SRR <sub>random</sub>	Parallel & Perpendicular	
Wire medium	N/A	

In Table 6.2, the different SRR orientations with respect to the incident electric field and their dimensions are presented. The electrical size of the SRR is small,  $\sim 0.1\lambda$  and the line width of the metallization is  $250\ \mu\text{m}$  and the spacing between the double split rings is  $300\ \mu\text{m}$ . The spacing between the split rings is very critical and gives rise to a capacitance that determines the resonance frequency. The split ring gap of  $460\ \mu\text{m}$  is important with respect to its orientation and determines the nature of the resonance but has a smaller influence on the resonance frequency. Since both these parameters are electrically very small,  $\sim 0.01\lambda$ , small changes in the values of these parameters due to thermal expansion may affect the resonance frequency.

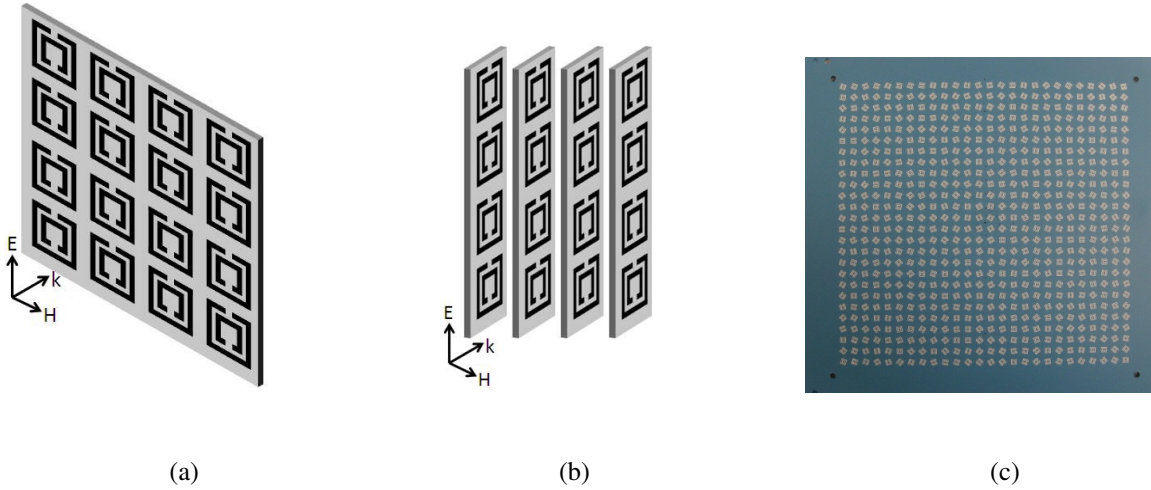


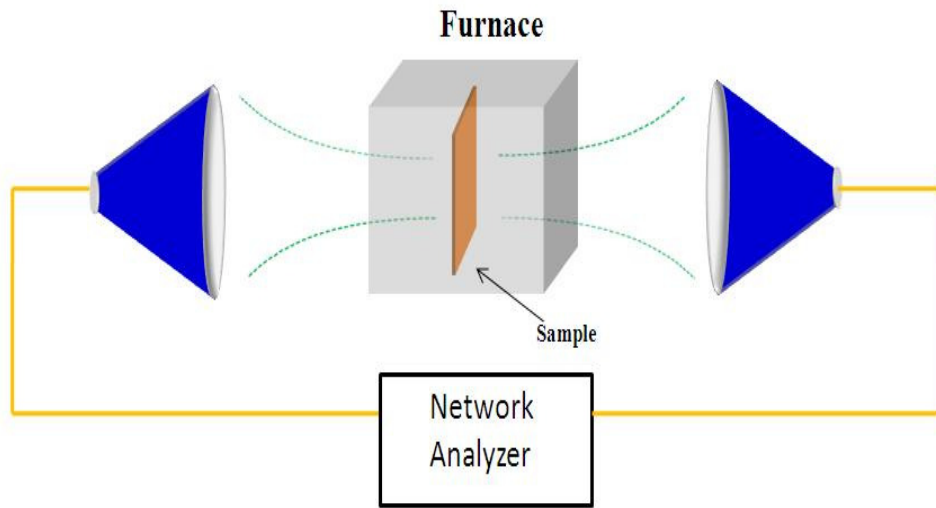
Figure 6.1 Sample geometries used in study: (a) incident wave vector perpendicular to the SRR plane; (b) incident wave vector parallel to the SRR plane; (c) randomly oriented SRRs on an LTCC substrate.

The FR4 metamaterial sample can be studied in two different arrangements - incident wave vector perpendicular to the plane of the SRR (Figure 6.1a) and by cutting the SRR into strips and placing them in a frame with grooves that can support the SRR strips at a fixed lateral spacing (Figure 6.1b). In this case, the incident wave vector is parallel to the plane of the SRR. For this case, we can orient the gap of the SRRs parallel to the E-field ( $SRR_{\parallel}$ ), gap of the SRRs perpendicular to the E-field ( $SRR_{\perp}$ ) and randomly oriented SRRs ( $SRR_{\text{random}}$ ). For the DuPont LTCC substrate, only one sample was studied that consisted of randomly oriented but periodically distributed SRRs all in a plane (Figure 6.1c). The sample size is 15 cm x 15 cm and the thickness depends on the orientation and placement of the SRRs.

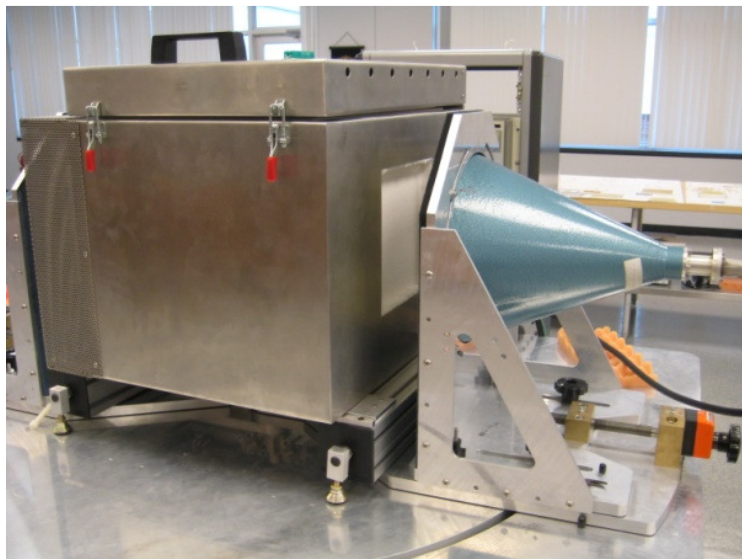


### 6.3 Experimental Set-up and Verification

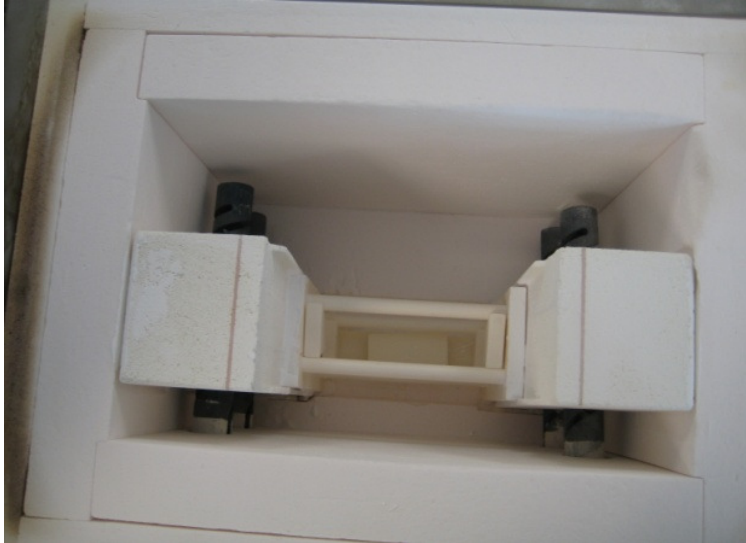
A free space measurement system as described in [62] and used in [60] for characterizing metamaterials, is used for the temperature study. Previously, the measurement system was modified to accommodate a furnace between the transmit and receive antennas [63, 64]. This arrangement is shown in Figs. 6.2a and 6.2b. The Tx and Rx antennas are conical horn antennas that are excited by coax-rectangular waveguide- circular waveguide transitions. Back to back plano-convex lenses are used to focus the radiation from the antenna into a Gaussian beam with a constant phase front and a focal diameter (3 dB width) of  $1\lambda$  at midband. For X-band measurements, the beam width is 3 cm and a sample size of 15 cm x 15 cm is sufficient to completely capture the incident beam since the first side lobes are 20 dB down. The focal length of the antenna is 30 cm. Free space TRL calibration is implemented to realize a calibration plane on which the amplitude and phase of the incident signal is defined. Time domain gating is also implemented to remove residual errors and potential multiple reflections between the antennas and the furnace windows. A sample holder is placed such that the front surface of a planar sample is at the calibration plane of the Tx antenna and the Rx antenna is moved back so that the back surface of the sample is at the calibration plane of the Rx antenna. The sample is supported in a picture frame sample holder as shown in Figure 6.2d.



(a)



(b)



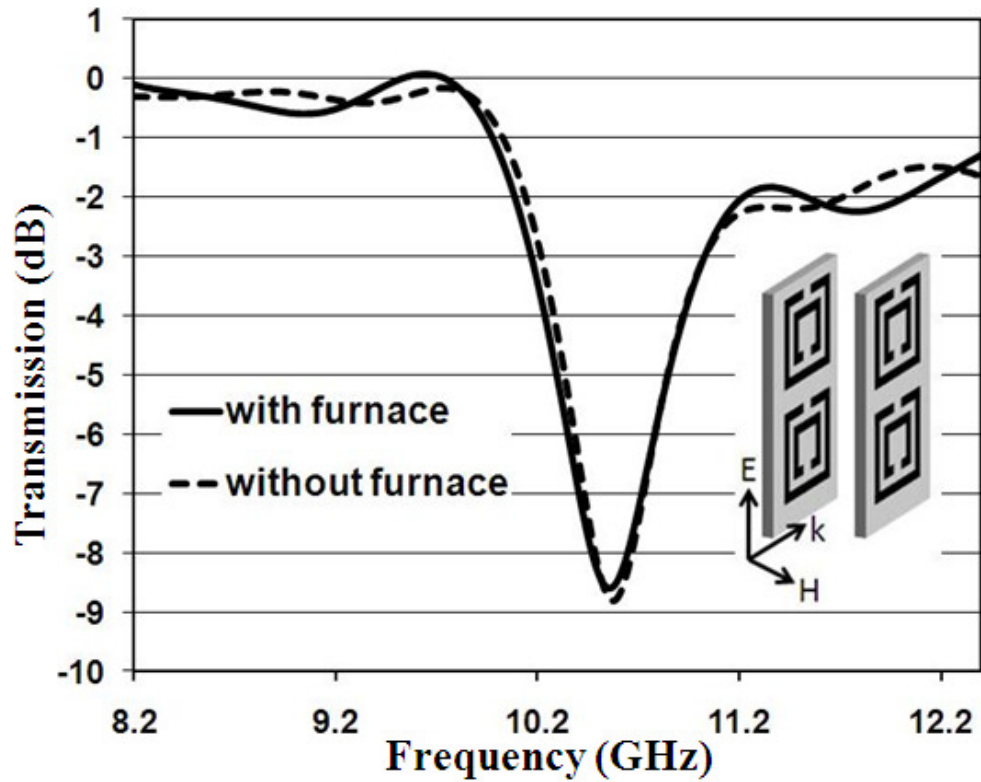
(c)

Figure 6.2 Experimental set-up used in study. (a) Schematic diagram of the set-up and (b) Photograph of the measurement setup; (c) Ceramic sample holder in the furnace.

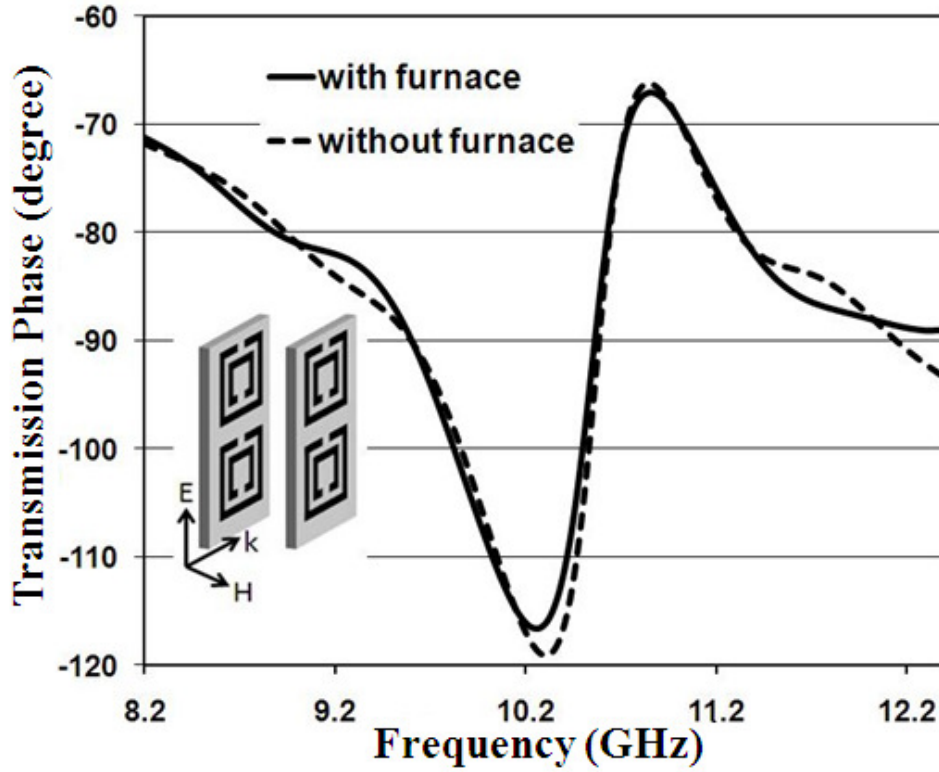
After performing TRL calibration, a DuPont 951 sample with screen printed SRRs that are randomly oriented and periodically distributed, as shown in Figure 6.1b is placed in the sample holder and the S-parameters are measured. The Nicholson-Ross-Weir method [49] is used to extract the complex permittivity and permeability from the measured complex S-parameters.

Next the furnace arrangement shown in Figs. 6.2a and 6.2b is wheeled into place between the antennas. The furnace has MW transparent, heat insulating windows that face the antennas. The furnace has a computer controlled temperature sensor and the temperature can be varied from 25°C to 1500 °C. A ceramic sample holder is used inside the furnace. First TRL calibration is performed with the furnace in place at room temperature. The SRR sample is first measured at

room temperature. In Figs. 6.3a, 6.3b, the S-parameters and complex dielectric permittivity of the SRR sample as measured with and without the furnace are compared.



(a)



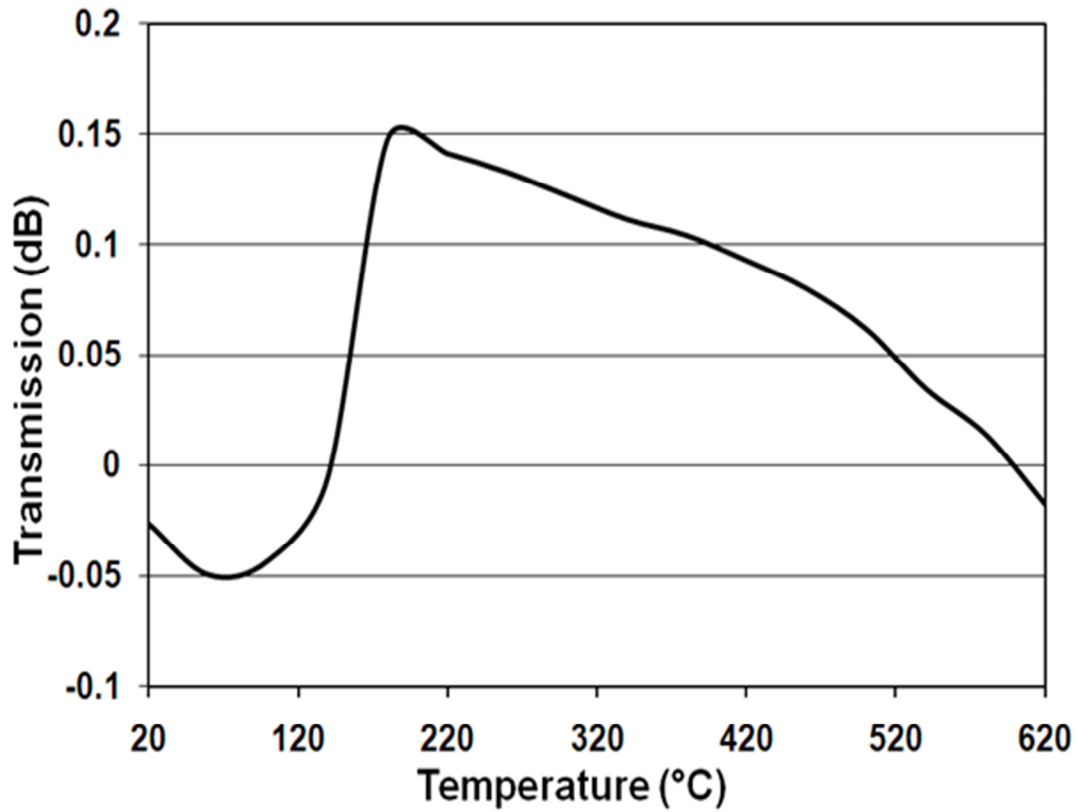
(b)

Figure 6.3 Verification of measurement data by comparison of measurements with and without the furnace in place at room temperature (a)  $S_{21}$  magnitude; (b)  $S_{21}$  phase.

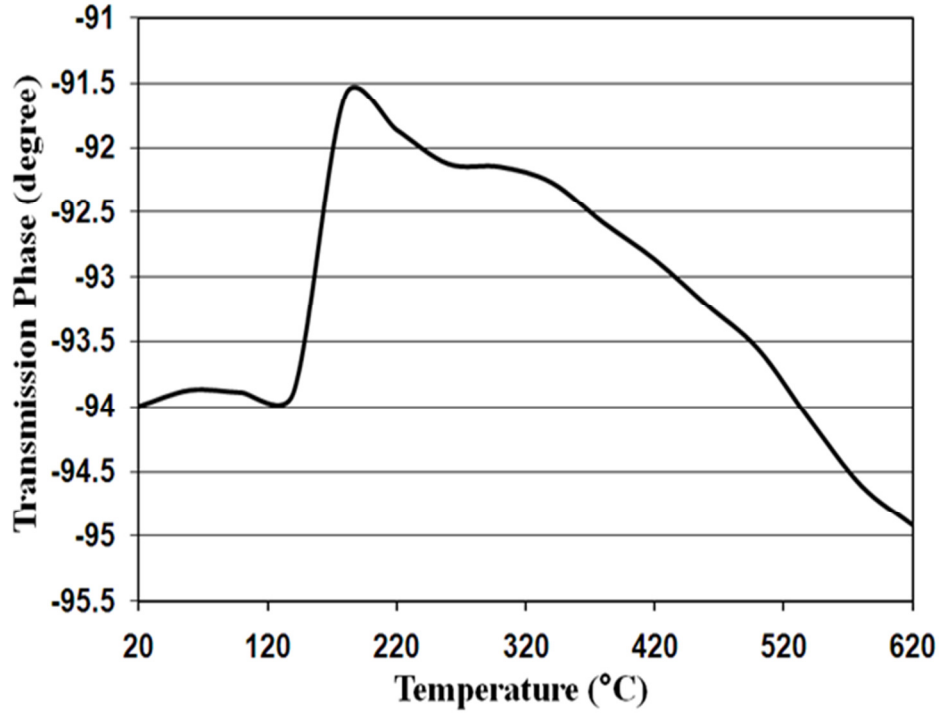
We have previously verified the accuracy of the free space measurements for metamaterial characterization by comparison with HFSS full wave simulations. We observe that the difference in  $S_{21}$  magnitude is less than 0.5 dB and phase difference is less than  $3^\circ$  on average.

Because the TRL calibration is performed at room temperature, it is necessary to verify if the calibration parameters drift with temperature. Physically it is not possible to recalibrate after we start heating the furnace. In Figure 6.4a and Figure 6.4b we plot the magnitude and phase of

the transmission coefficient ( $S_{21}$ ) of the empty furnace as a function of temperature. We plot the transmission at 10GHz, at the center of the X-band frequencies (8-12.4 GHz), since this can give us an idea of the calibration drift, if any, with temperature. The  $|S_{21}|$  changes only by about 0.2 dB, which is acceptable. The phase varies as small as  $3.5^\circ$  as can be seen from Figure 6.4b.



(a)



(b)

Figure 6.4 Variation of transmission through an empty furnace at 10 GHz as a function of temperature (a) magnitude; (b) phase.

We may conclude that accurate measurement of the amplitude and phase of  $S_{21}$  as a function of frequency and temperature is possible with the proposed set-up and calibration procedure.

#### 6.4 High Temperature Characterization of Material Samples

Several metamaterial samples as described in Table 4.2 were characterized in the X-band as a function of temperature. For SRRs printed on the FR4 substrate, we had to limit the maximum temperature to 90°C to prevent the FR4 from becoming soft. We heated the Dupont 951 samples to a temperature of 420°C. For the FR4 samples, we characterized SRR<sub>||</sub> strips

(electric resonance),  $SRR_{\parallel}$  strips (magnetic resonance) and randomly oriented SRR strips,  $SRR_{\text{random}}$  (both electric and magnetic resonance) for which the  $k$ -vector is in the plane of the SRRs. The real part of the permeability and/or permittivity, as appropriate, extracted from the measured complex  $S_{11}$  and  $S_{21}$  is plotted in Figs. 6.5-6.7.

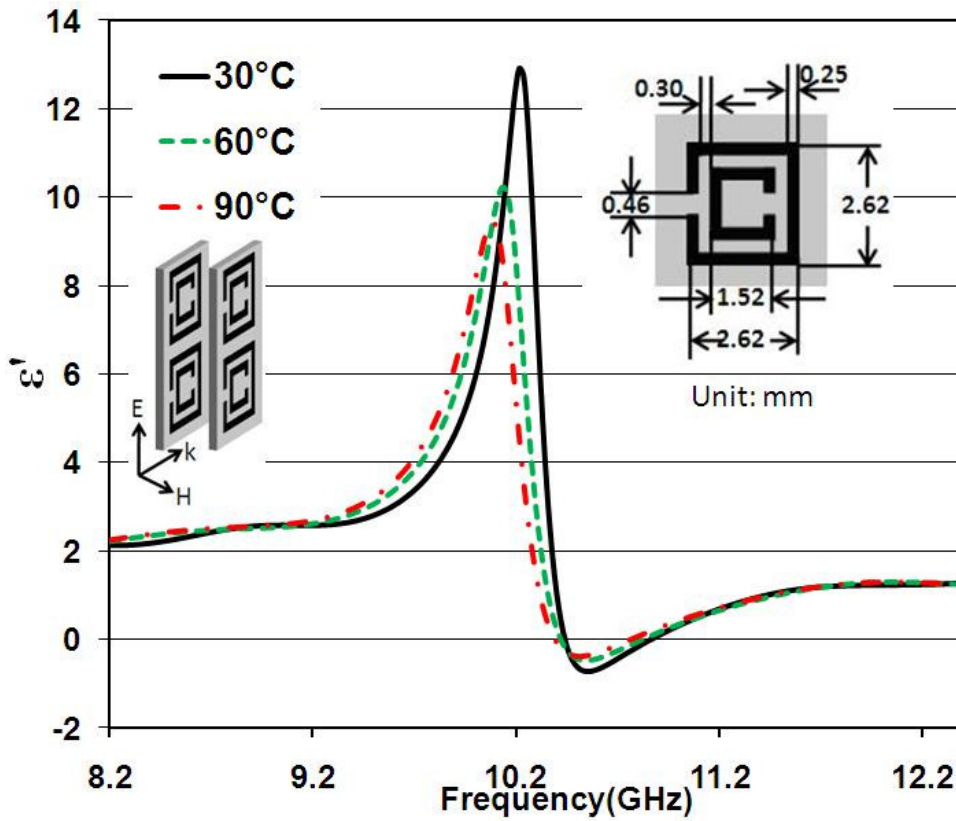


Figure 6.5 Measured real part of permittivity for  $SRR_{\parallel}$  printed on FR4 substrate at various temperatures.



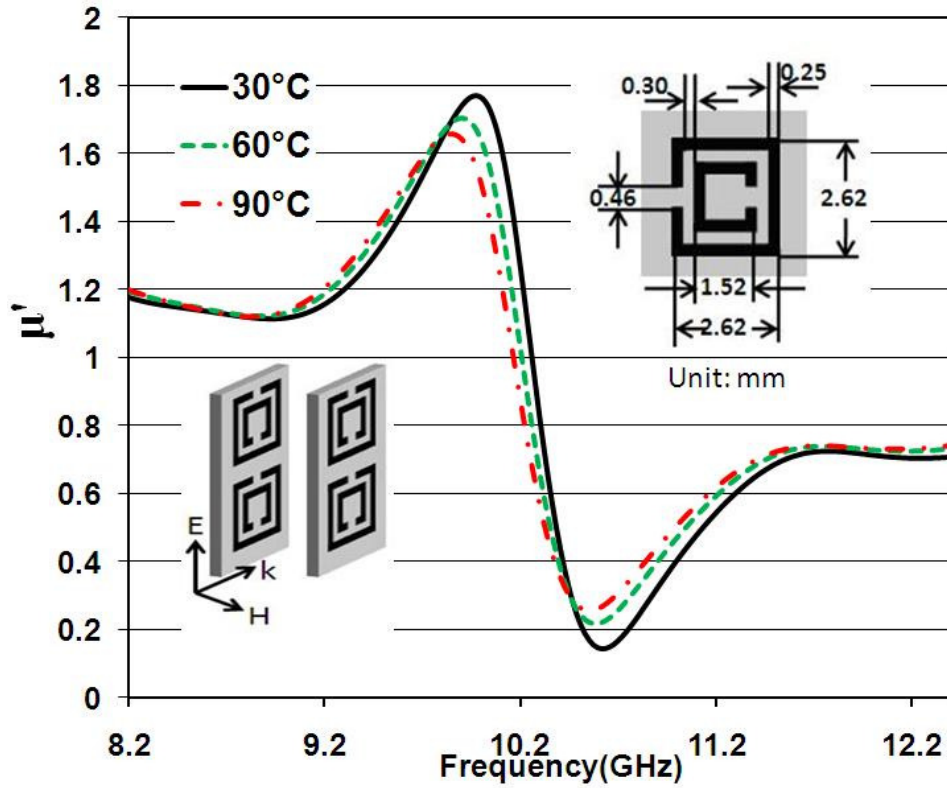
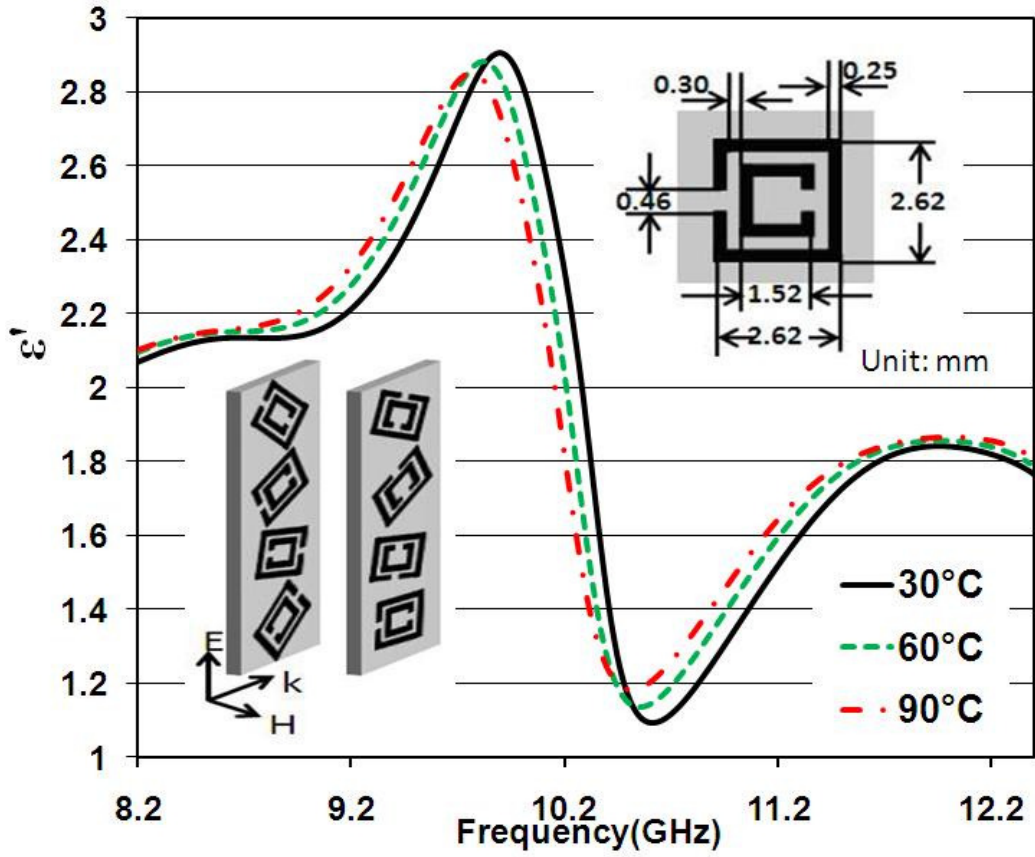
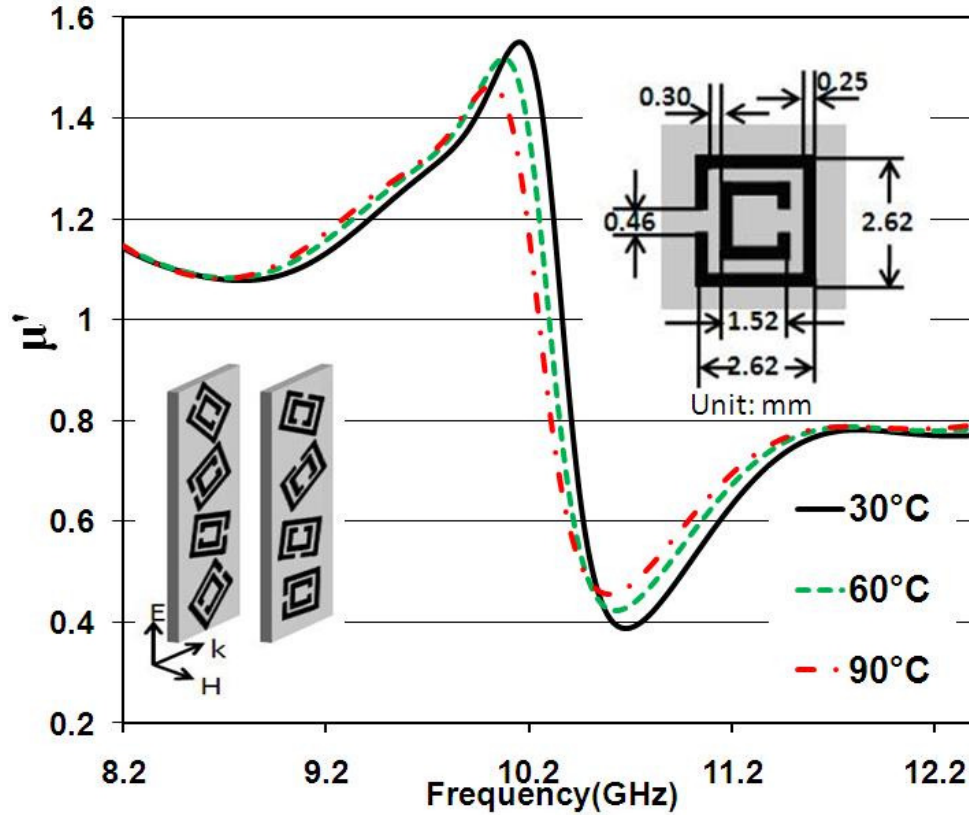


Figure 6.6 Measured real parts of permeability for  $SRR_1$  on FR4 substrate at various temperatures.

The imaginary part is not presented here. In all three figures we notice a systematic downward shift of the maxima and minima of  $\mu'$  and  $\epsilon'$  with rising temperature, both in amplitude and frequency. Since the temperature range is only from 30°C – 90°C, the shift is small but the trend is well defined.



(a)



(b)

Figure 6.7 Measured real parts of (a) permittivity and (b) permeability for the SRR<sub>random</sub> on FR4 substrate at various temperatures.

In Figure 6.8, the shift in the resonance frequency is plotted as function of temperature for all three samples. The downward frequency shift is about 0.15 GHz for a temperature change from 30°C to 90°C for all three samples. Although the resonance frequency is slightly different for the three cases, the change is almost the same. We may infer from this, that the change is associated with changes in the substrate and electrical conductivity and thermal expansion of the Cu metallization that is the same for all three samples. This will be discussed in the next section.

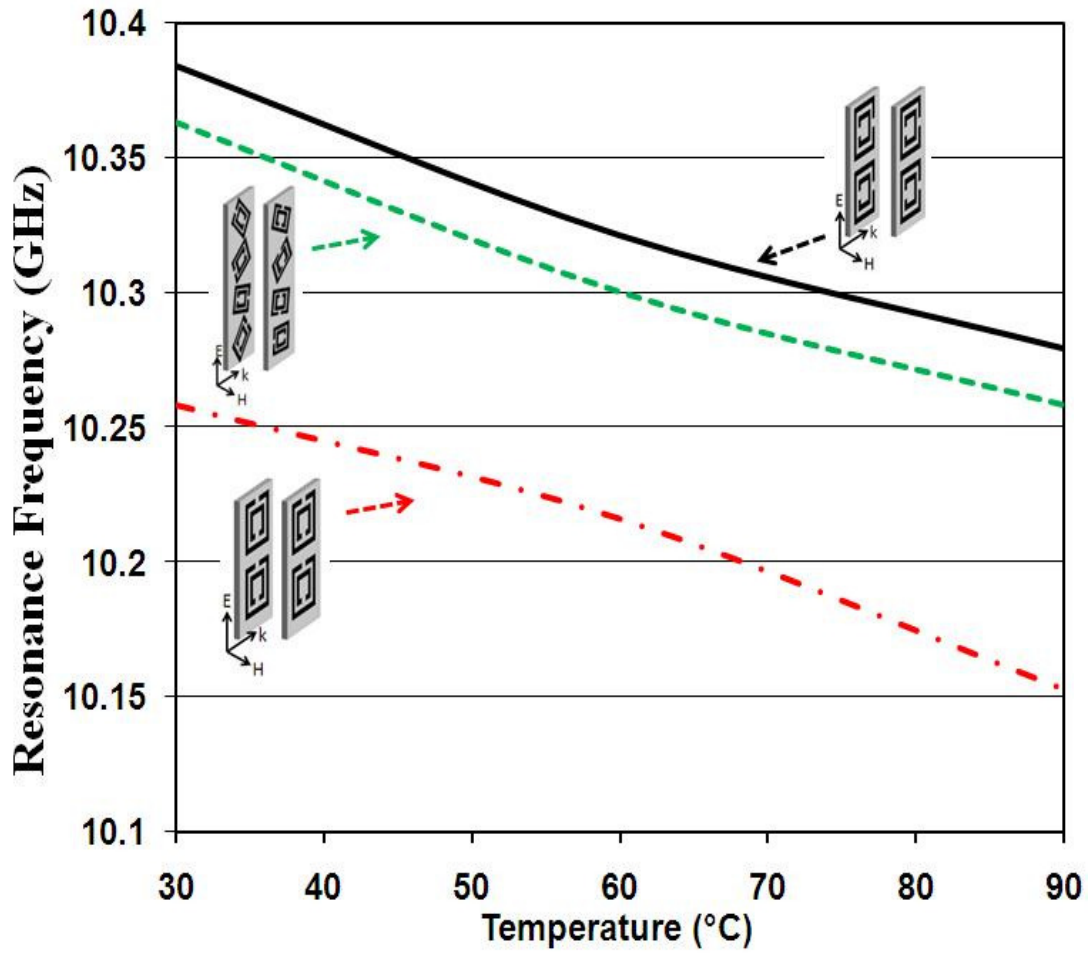


Figure 6.8 Observed change in resonance frequency of FR4-SRR samples versus temperature.

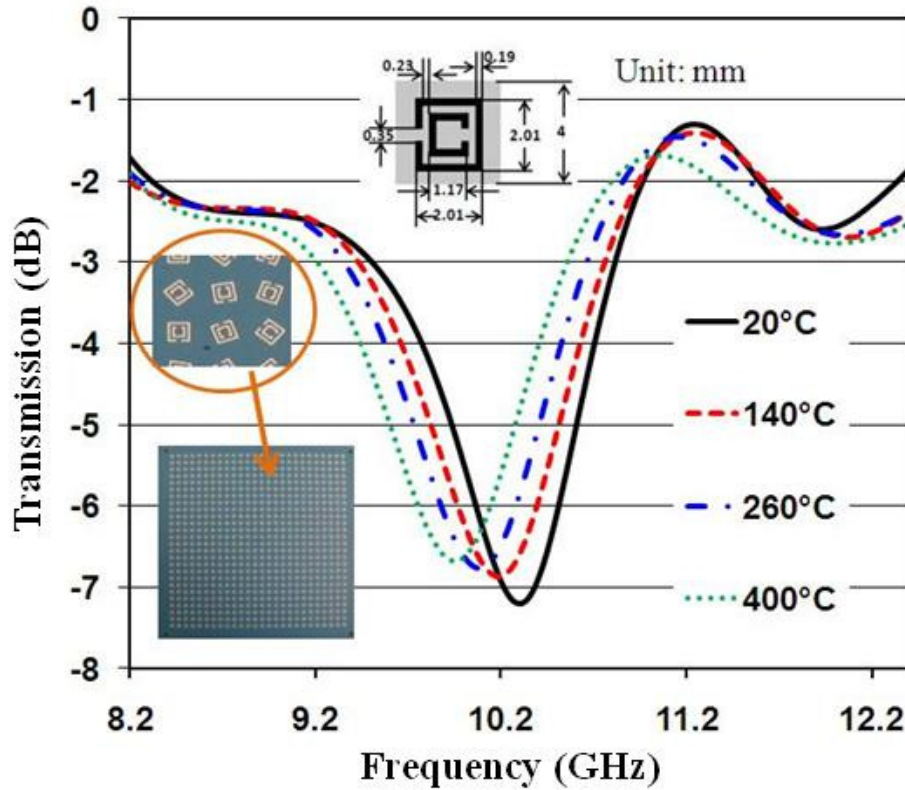


Figure 6.9 Measured magnitude of  $S_{21}$  of the random SRRs on LTCC substrate.

Next, the DuPont 951 sample with randomly oriented SRRs is characterized from room temperature to 420°C. This time we present the magnitude of  $S_{21}$  in Figure 6.9. The minimum of  $S_{21}$  is associated with the resonance frequency of the SRRs. The actual definition of the resonance frequency varies; some authors take this to be the minimum of  $S_{21}$  and others as the frequency at which there is maximum power absorption. Again, we observe the systematic downward shift of the maxima and minima amplitude as well as the resonance frequency with increasing temperature. In Figure 6.10, the shift in resonance frequency with temperature is plotted. For the DuPont 951 sample, we observe a frequency shift of 0.35 GHz for a temperature change of almost 400°C.

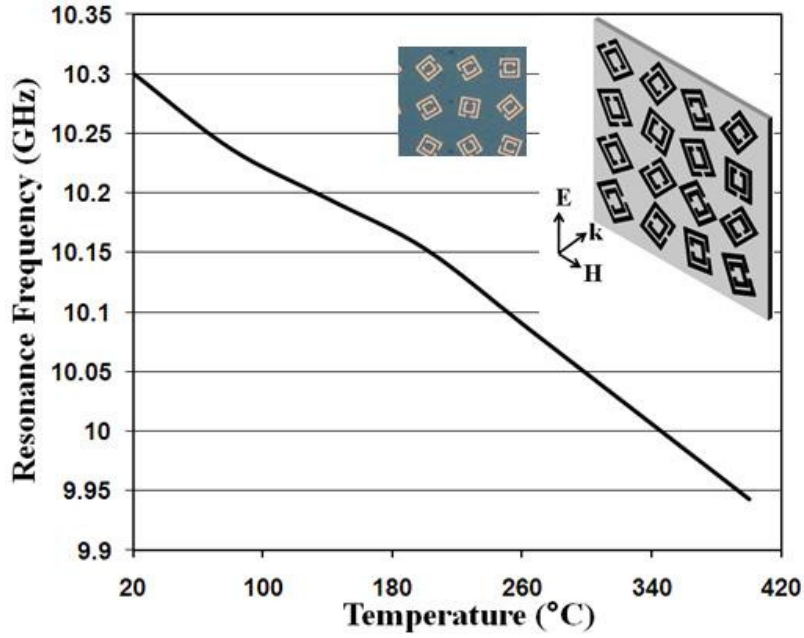


Figure 6.10 Observed change in resonance frequency of DuPont 951-SRR sample versus temperature

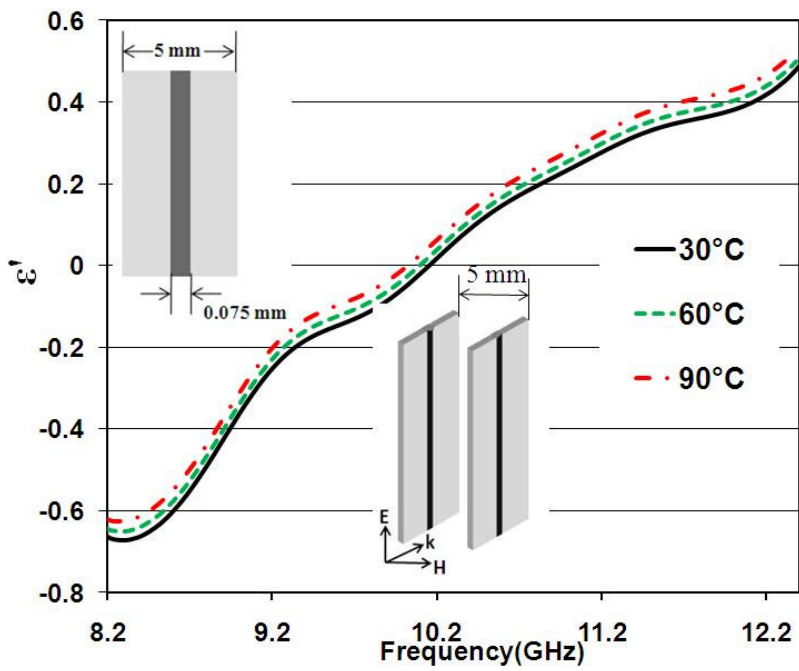


Figure 6.11 Observed change in plasma frequency for a thin wire medium (printed on FR4).

We also performed measurements on a wire sample printed on FR4 using the strip arrangement. It has been shown [65] that a parallel array of very thin wires with electric field parallel to the wires behaves like a plasma medium. The real part of the effective permittivity of such a medium displays the Drude behavior with negative values below a well-defined frequency called the plasma frequency that depends on the radius of the wires and the spacing between the wires. In Figure 6.11, we have plotted the real part of the permittivity of an FR4 wire sample extracted from the measured S-parameters. We again notice a well-defined, but small downward shift of the plasma frequency from 10.13 GHz at room temperature to 10.03 GHz at 90°C.

The per degree shift of frequency for the FR4 sample is 0.021 GHz/°C and the per degree shift of the DuPont 951 sample is 0.0087 GHz/°C which is much lower. So we may expect that the permittivity of DuPont 951 changes much less with rising temperature than FR4. We also conclude that the per degree shift of the resonance frequency is not dependent on the polarization of the incident wave *w.r.t.* the orientation of the SRR gap. The reasons for the decreasing resonance strength and downward shift in the resonance frequency are studied in the next section.

## **6.5 Theoretical Explanation of the Observed Temperature Behavior of Metamaterials**

Based on the experimental data, we hypothesize that there are three possible reasons for the decreasing resonance strength and resonance frequency with rising temperature. These are:

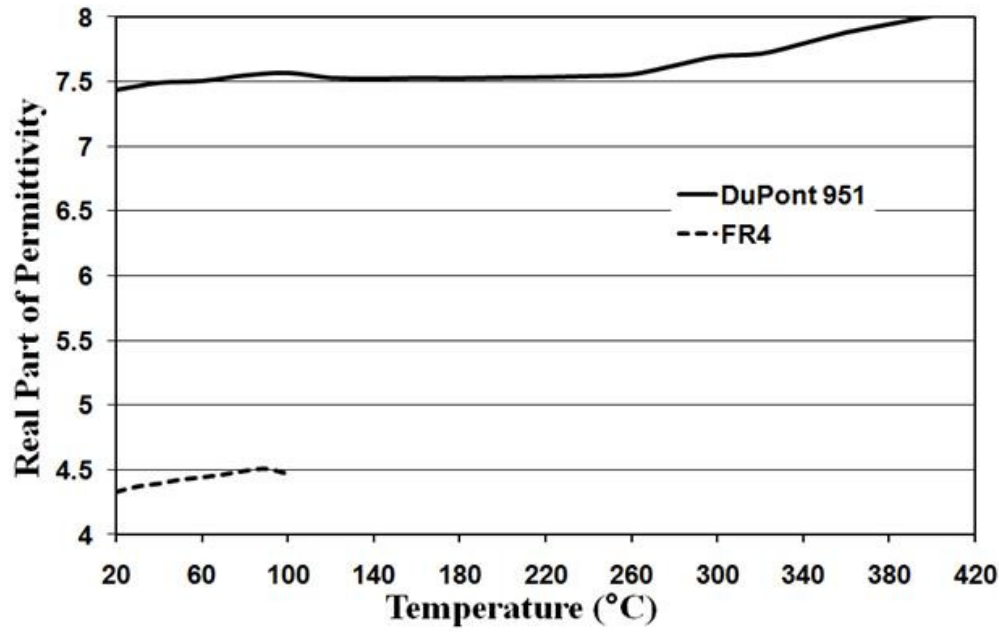
- 1) Change in the dielectric permittivity of substrate with temperature
- 2) Change in the electrical conductivity of the metal
- 3) Thermal expansion of the metal

We next verify our hypotheses by calculating the change in resonance strength and resonance frequency caused by each factor either with experimental data or full field, finite element simulations. We assume that the three factors are independent and can be calculated separately. We next perform a full wave finite element simulation of the transmission and reflection of waves through metamaterial sample inputting the temperature dependent permittivity, electrical conductivity and changes in the dimensions of the SRRs due to thermal expansion. This result will be compared with the experimental data to verify if the observed change in resonance frequency agrees with the simulation thereby verifying our hypotheses.

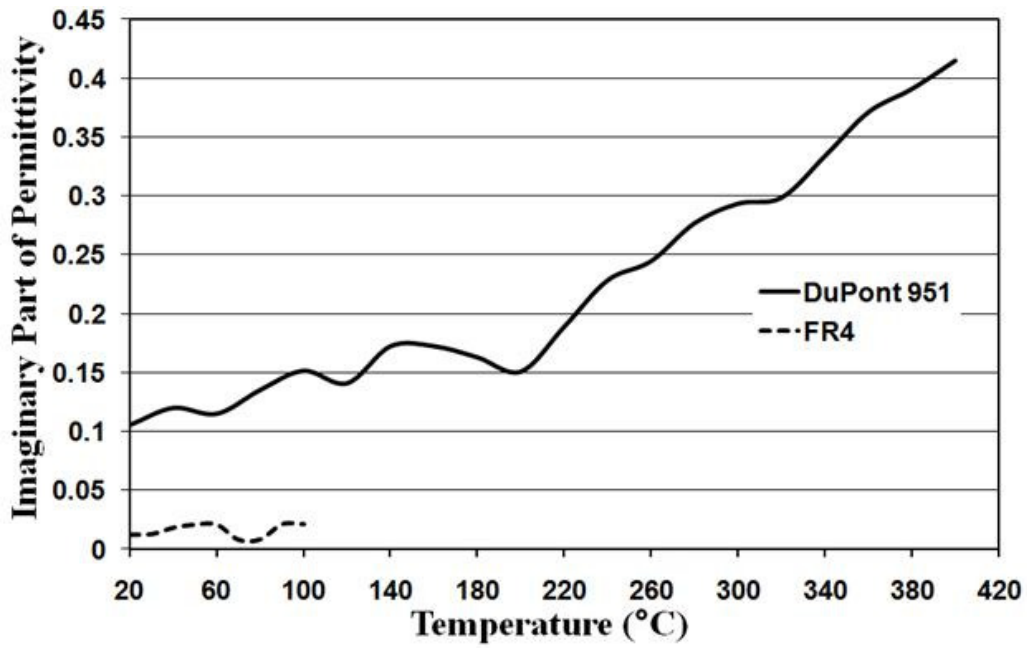
#### A. Temperature dependence of substrate permittivity

Since the FR4 samples could not be heated to high temperatures, we focused on the temperature behavior of the DuPont 951 substrate. A blank sample of the material of thickness 1.05 mm was fabricated using the LTCC process. The complex dielectric property of the blank LTCC and FR4 samples were measured as a function of temperature and plotted in Figure 6.12. The real part of the permittivity of LTCC averaged over X-band frequencies increases from 7.36 at room temperature to 7.88 at 400°C. The imaginary part of the permittivity increases with temperature. For FR4, the real part of permittivity changes from 4.33 to 4.51 from 20°C to 90°C. It has been shown [66] that lowering the dielectric permittivity of the substrate increases the resonance frequency of metamaterial since this corresponds to a decrease in the electrical size of the structure with increasing wavelength.





(a)



(b)

Figure 6.12 Measured temperature dependence of permittivity of DuPont 951 and FR4 averaged over X-band frequencies (8.2-12.4 GHz). (a) Real part; (b) Imaginary part.

B. Temperature dependence of the electrical conductivity of Cu and Ag

The conductivity of bulk metals has the following dependence on temperature:

$$\sigma_T = \frac{\sigma_{T_0}}{1 + \alpha(T - T_0)} \quad (6.1)$$

where  $T_0$  is the initial or room temperature at which the conductivity  $\sigma_{T_0}$  is known.  $\alpha$  is the coefficient of thermal expansion of the metal.

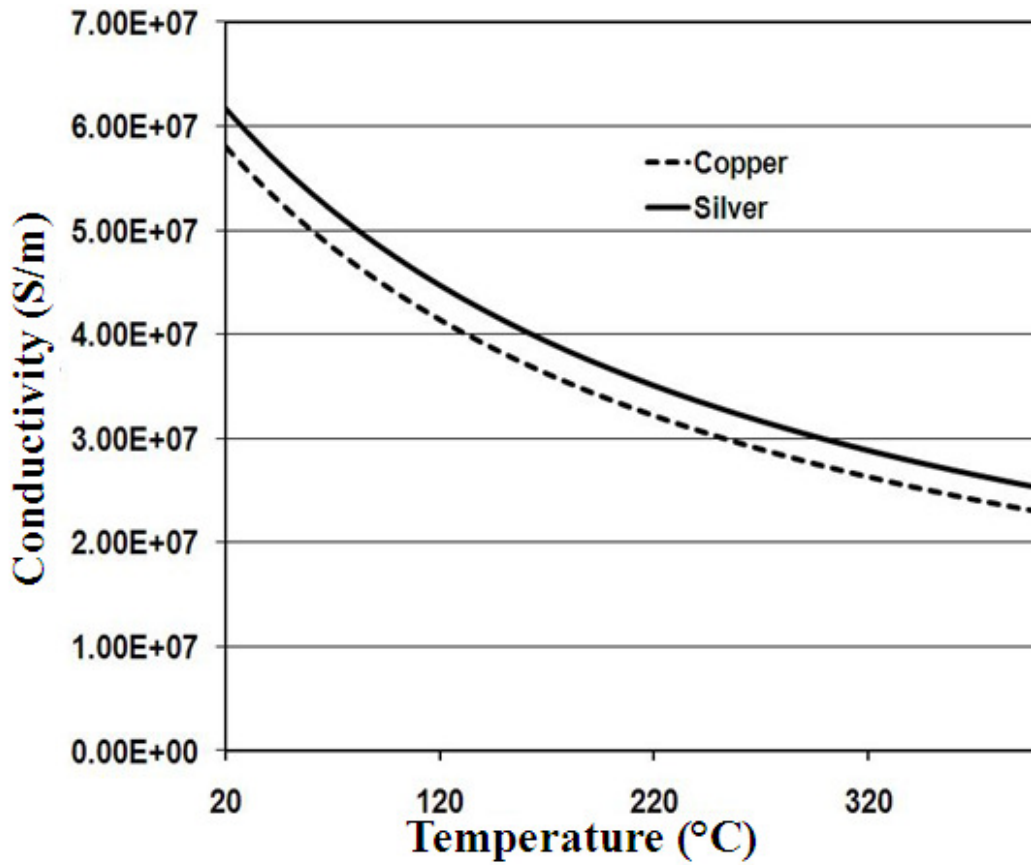


Figure 6.13 Temperature dependence of the conductivity of copper and silver calculated using Eq. 6.1.

The decreasing conductivity with rising temperature leads to a lower drift velocity for free electrons. As we know, free electrons in a conductor move randomly if no field is applied. An applied electric field results in an average drift velocity as given by the Drude free electron model. At high temperatures, the free electrons move faster but randomly, so the applied electric field cannot accelerate the electrons as effectively, resulting in a lower drift velocity. Therefore, more energy is dissipated in the other terms. We can explain the decreasing resonance strength of the permittivity and/or permeability with increasing temperature by looking at the effect of conductivity on a Lorentz model that describes very well the permittivity and permeability plots shown in Figs. 6.5-6.7. For example, the Lorentz model for the permeability as given in [67] may be written as

$$\mu_{eff} = 1 - \frac{F}{1 + j \frac{2\rho_S}{\omega r \mu_0} - \frac{3}{\pi^2 \mu_0 \omega^2 C r^3}} \quad (6.2)$$

where  $\rho_S$  is the surface resistivity of the metal,  $C$  is the capacitance between the inner and outer rings and  $r$  is the radius of the ring. The magnitude of  $\mu_{eff}$  and  $\varepsilon_{eff}$  will decrease with increasing resistivity or conversely decreasing electric conductivity. We can thus attribute the small drop in the resonance strength with increasing temperature on the drop in electrical conductivity. In Figure 6.13 below, we present the temperature dependence of the conductivity of Cu (used in the FR4 samples) and Ag (used in the LTCC samples).

### C. Thermal Expansion of the Substrate

The thermal expansion coefficients of DuPont 951 and FR4 are very small, 5.8 ppm and 11 ppm respectively. For example, this will result in a change in thickness for LTCC of only 2.32

$\mu\text{m}$  from  $20^\circ\text{C}$  to  $400^\circ\text{C}$  and for FR4 by  $0.5 \mu\text{m}$  from  $20^\circ\text{C}$  to  $90^\circ\text{C}$ . According to the results in [68], this would lead to a negligible shift in the resonance frequency.

#### D. Thermal expansion of SRRs

The dimensions of the SRRs are quite small, the largest dimension being 2.01 mm and the smallest being  $190 \mu\text{m}$ . These dimensions are very critical in determining the resonance frequency of the SRR. As temperature increases and the metal expands, and even small changes in dimensions can shift the resonance frequency. Since the metallization thickness is very small ( $17 \mu\text{m}$  for Cu and  $10 \mu\text{m}$  for Ag) and the thermal expansion of the substrate also plays a role, it is not accurate to estimate the increase in geometrical parameters using a linear thermal expansion model. Instead, we used the thermal expansion simulation tool in the ANSYS finite element code for mechanical structures, to compute the geometrical size of the SRR on the DuPont 951 substrate at  $400^\circ\text{C}$  starting with the known parameters at room temperature. The thermal and mechanical properties of DuPont 951 and Ag are given in Table 6.3.

Table 6.3 Mechanical and Thermal Properties of Silver and DuPont 951 [69, 70]

	Thermal Coefficient (ppm/ $^\circ\text{C}$ )	Young's Modulus (GPa)
DuPont 951	5.8	120
Silver	18	76

In Figure 6.14 we show the room temperature dimensions of an SRR deposited on DuPont 951 and the dimensions at  $400^\circ\text{C}$  calculated using ANSYS. We observe that the parameters increase by approximately 0.33% due to rise in temperature. It is very well known

that if the size and hence the electrical size of the SRR increases, its resonance frequency will be smaller.

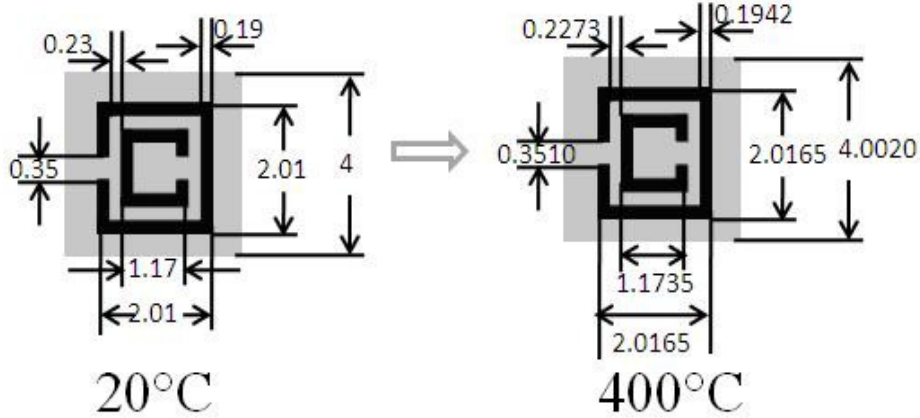


Figure 6.14 Change in dimensions of an SRR computed using ANSYS due to thermal expansion of silver and the substrate from 20°C to 400°. The unit is mm.

Thus, we may conclude that decreasing substrate permittivity and increasing size of the SRRs leads to a lower resonance frequency as temperature increases.

## 6.6 Comparison of Full Wave Simulation with Observed Data

Next we performed a full wave simulation using Ansoft HFSS and computed the S-parameters of the DuPont 951 sample with randomly oriented SRRs. First we included the temperature dependence of each of the three factors we studied separately to understand their relative importance in lowering the resonance frequency. In Table 6.4 below, we show the resonance frequencies at 20°C and 400°C respectively for: (i) experimental data; (ii) including only thermal changes in dielectric permittivity; (iii) including thermal changes in electric conductivity only; and (iv) effects of thermal expansion only. The % change of resonance

frequency is denoted for each case. We observe that the temperature dependence of the dielectric permittivity is the dominant contributor (90% of the observed resonance frequency change) followed by thermal expansion of the SRR (10% of the observed resonance frequency change). The effect of changes in the electrical conductivity is 5%.

Table 6.4 Shift in Resonance Frequency Due to Each Factor (20°C to 400°C)

	Resonance Frequency Shift (GHz)	Percentage Shift (%)
Thermal Expansion	0.037	10.36
Substrate Permittivity	0.3	84.03
Metal Conductivity	0.018	5.04

Finally, all effects were included in a HFSS simulation for the entire X-band and in Figure 6.15 we compare the frequency shift for the DuPont 951 sample between 20°C and 400°C obtained from simulation and measurement. It is seen that the comparison is quite good and the HFSS simulation predicts a shift of resonance frequency of 0.35 GHz compared to 0.36 GHz in the experimental data.

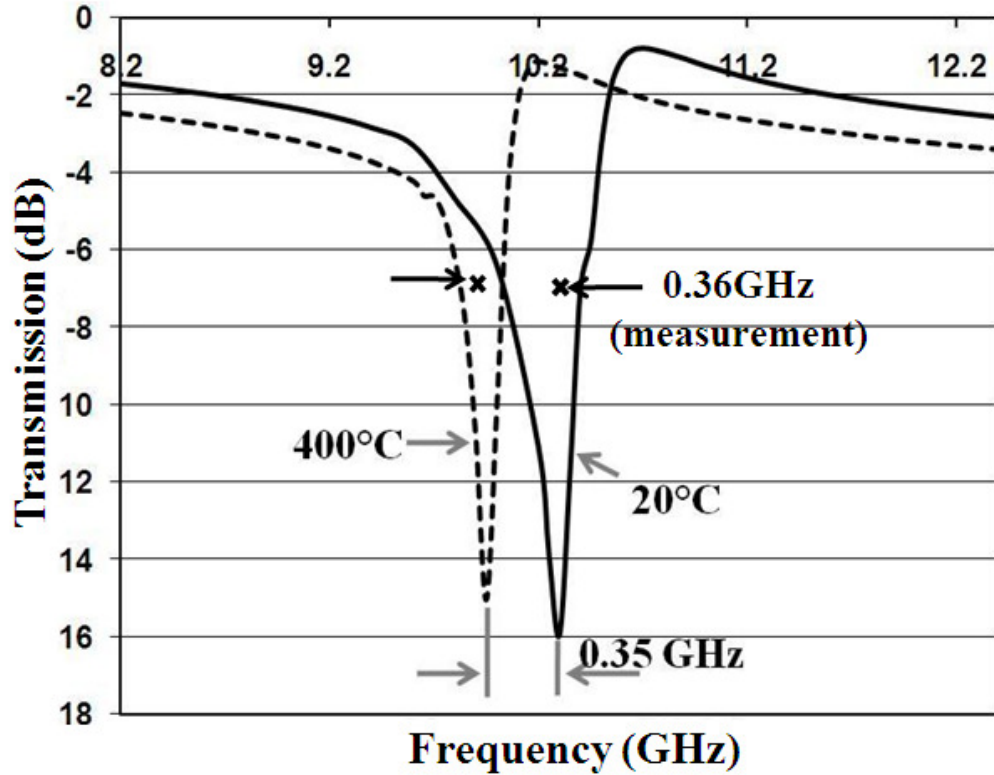


Figure 6.15 Numerically simulated (using Ansoft HFSS)  $|S_{21}|$  for random SRRs on an LTCC substrate at 20°C and 400°C. Material and size parameters at 400°C calculated using ANSYS.

## 6.7 Future Work

In summary, the temperature dependence of plasmonic resonances is majorly due to the changes in the optical constants of materials. The thermal expansion of metallic structures is negligible if noble metals are used. In order to compensate the changes of material properties and make plasmonic resonances stable at different temperatures, Shape Memory Alloys (SMA) can be employed to make plasmonic structures. The phase transition of SMAs is trained in a way that they will expand or shrink to the desired geometry. As a result, plasmonic structures are able to perform adaptive transitions with respect to the temperature of solar cells.

## VII. Light Trapping by Nanodome Geometry

### 7.1 Background

Nanodome geometries have been used to enhance light absorption in thin film solar cells. An efficient light trapping design should achieve the following two goals: (1) light management to minimize reflection and efficiently trap light in the absorber material and (2) effective carrier collection management to efficiently harvest photocarriers produced in the absorber. An efficient light and carrier collection management (LCCM) would result in a significant enhancement in a-Si:H thin film solar cells. Single junction cells with an efficient LCCM would result in a performance very similar to multijunction cells. The same approach for single junction cells can be used in multi-junction cells. However, manufacturing single junction a-Si:H solar cells with nanodome geometries would be simpler because multi-junction a-Si:H solar cells require more controls in randomly textured transparent conductive oxides (TCOs), complex active layer alloys, tunnel junctions between layers, and properly matched absorber layer thicknesses [71].

### 7.2 Design and Fabrication

People have reported the use of sub-wavelength features to enhance light absorption. All of the methods employed a-Si:H substrate configurations and have yielded power conversion efficiency (PCE) values of 5.9%, 8.1% (polarized light) and 6.6%. Here, we show our fabrication of an a-Si:H solar cells using a LCCM design. The fabricated cell yields a PCE of 8.2% for single junction p-i-n devices. This is, so far, the highest reported efficiency for an a-Si:H solar cell using sub-wavelength designs. In addition, we will show that the enhancement is due to the combined contribution from the volume of a-Si:H, photonic effects and plasmonic effects. The fabricated design is shown in Figure 7.1.



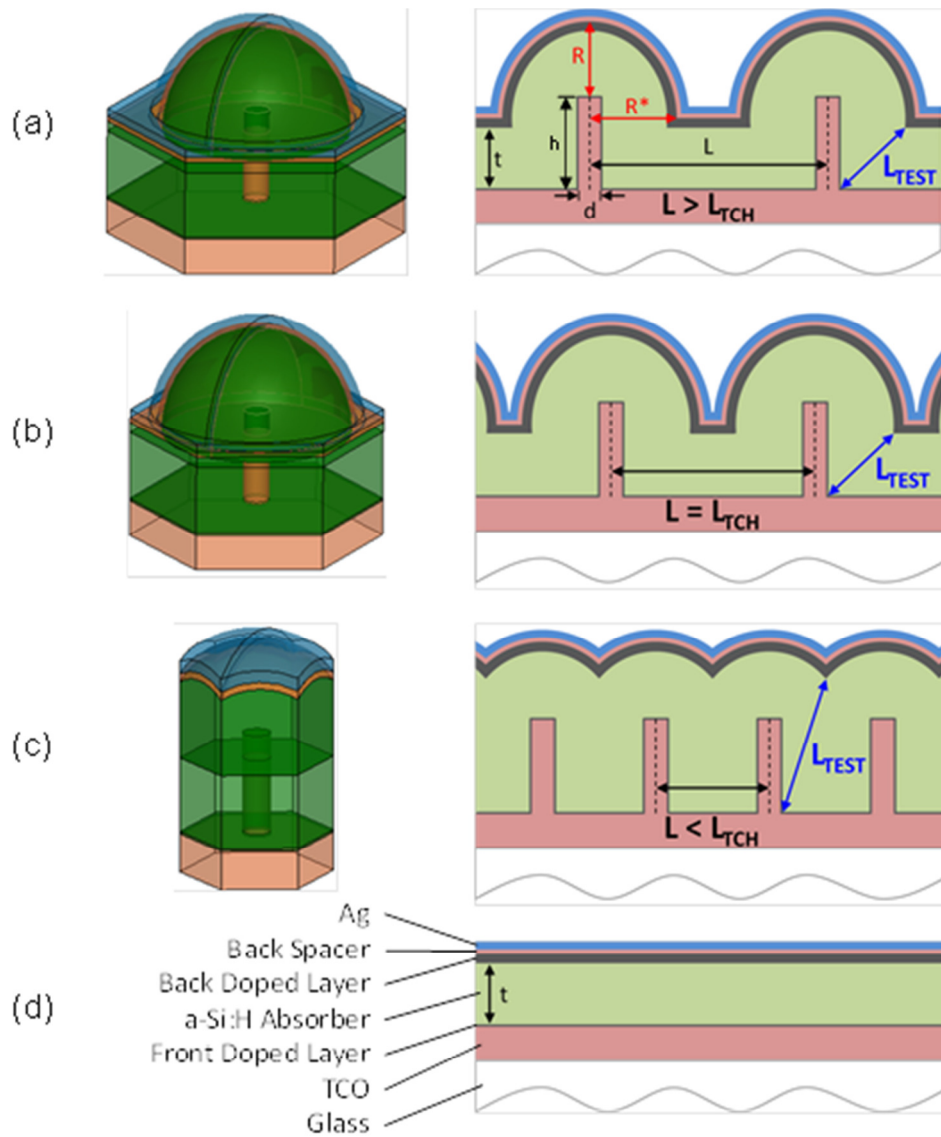


Figure 7.1. The unit cell of the LCCM design used in this study. Three possibilities are shown: (a) Non-overlapping undulations, (b) touching undulations, and (c) overlapping undulations. The control device is shown in (d). The parameter  $t$  is the thickness an a-Si:H deposition would give in the inter-dome regions. It is also the a-Si:H thickness in the control cell of (d).

In Figure 7.1, the cell has the nanodomains periodically located in a hexagonal pattern on glass. Each nanodome is a unit cell. The unit cell areas cover the surface of the glass. The nanocolumns (height  $h$ , diameter  $d$  and spacing  $L$ ) at the center of each unit cell generate periodic

features as layers are sequentially deposited. The resulting patterns of nanodomains may appear differently depending on the spacing  $L$ . As shown in Figure 7.1, the undulating features (domes) can be chosen to have spacings  $L$  in one of three regimes. (1)  $L > L_{TCH}$  where the domes do not touch (Figure 7.1a); (2)  $L = L_{TCH}$  where the domes just touch (Figure 7.1b); and (3)  $L < L_{TCH}$  where the domes overlap and are truncated (Figure 7.1c).

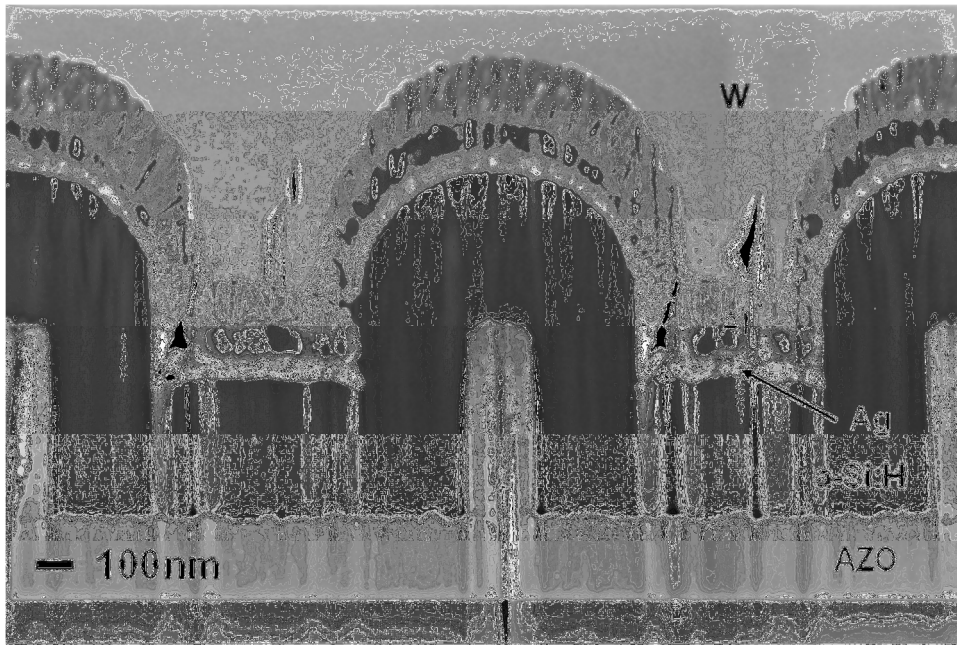


Figure 7.2. FESEM micrograph showing the cross-section of an actual LCCM device. The cross-section was prepared using focused ion beam milling. The AZO nano-columns had  $d = 150$  nm,  $h = 525$  nm, and  $L = 1290$  nm. This device contained an a-Si:H i-layer ( $t = 320$  nm), a  $p$ -type layer (13 nm) and an  $n$ -type layer (60 nm).

The nanodomains were fabricated on a planar base of a-Si:H, whose thickness is 400 nm. It is a typical thickness for a-Si:H thin film solar cells. A planar cell with 400 nm thick a-Si:H is defined as the control cell for our future study. We found out that  $t = 400$  nm resulted in an a-Si:H

coating on a nano-column of about 300nm in side-wall thickness (Figure 7.2). The choices for nano-column  $h$ ,  $d$ , and  $L$  of our superstrate design were then guided by the distances  $L_{TCH}$  and  $L_{TEST}$  of Figure 7.1. The quantity  $L_{TCH}$  is the center to center spacing of the case when the neighboring domes just touch. There is no planar region in between domes. The quantity  $L_{TEST}$ , defined for every  $L$ , measures the longest collection distance. As shown in Figure 7.1,  $L_{TEST}$  points from the bottom of a TCO column to the closest point at the back electrode surface at any  $L$ . An efficient carrier transport would require the length of carriers traveled from any location within the absorber to the electrodes less than the collection length of minority carriers within a-Si:H. In our convention, it is  $L_{TEST} < L_{COL}$  where  $L_{COL}$  is the collection length. Carrier collection in the a-Si:H  $p-i-n$  devices under consideration is by drift and the drift collection length  $L_{COL}$  is 400-500 nm. Therefore, our choice of  $L$  for fabrication must satisfy  $L \geq L_{TCH}$ .

In our fabrication work, we targeted the column diameter to be 150nm, AZO back spacer thickness to be 30nm, and the Ag cathode thickness to be 50nm. In Figure 7.1,  $L_{TCH} = 910$ nm and it requires  $L \geq 910$ nm to avoid any major problems in carrier collection. As a result, we select an  $L$  of  $\sim 1300$ nm for our device. The column height  $h$  was dictated by the column diameter used and the aspect ratio that could be readily tolerated by our process flow. Figure 7.2 shows the field emission scanning electron microscope (FESEM) micrograph of the cross-section of an actual LCCM solar cell structure resulting from these design criteria. It shows  $t \approx 400$ nm, an AZO column side a-Si:H coating thickness of  $\approx 300$ nm, and a spacing  $L \approx 1290$ nm were actually obtained. This particular device had no back AZO spacer layer. The W used in the focused ion beam milling process can be seen.

Although e-beam lithography was used to generate the sub-wavelength patterns shown in Figure 7.1 and Figure 7.2, we envision a manufacturing approach using nano-imprinting or

stamping. However, for the devices in this report, the processing began by defining a template of empty cylinders arranged in a hexagonal pattern with  $L = 1290$  nm on top of an e-beam resist coated planar AZO layer (210 nm thick on glass). Atomic layer deposition (ALD) was used to fill the template with AZO. A subsequent lift-off step removed the excess AZO and produced the free-standing nano-columns ( $d = 150$  nm,  $h = 525$  nm).  $p$ -doped (13nm), intrinsic, and  $n$ -doped (60nm) a-Si:H layers (totaling  $\sim 400$  nm) were then deposited via PECVD onto the array. Deposition of the back spacer layer (0 or 30 nm AZO) and the cathode (Ag 50 nm) completed the device.

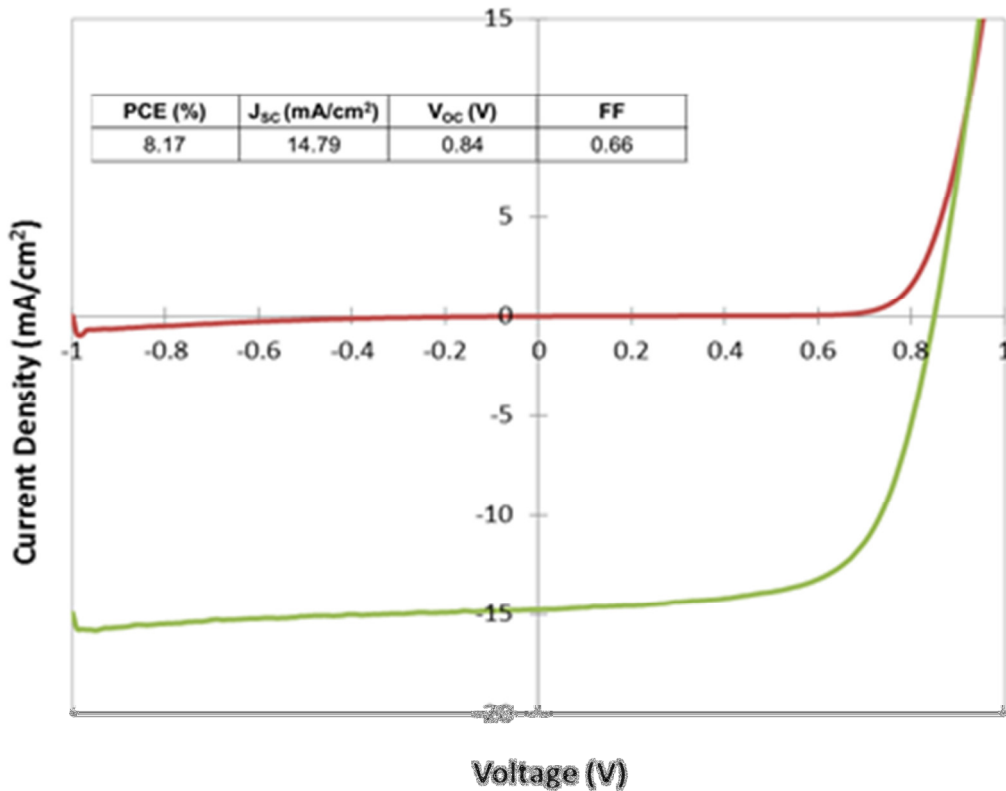


Figure 7.3. The light (AM 1.5,  $100 \text{ mW/cm}^2$ ) and dark J-V and performance characteristics of an LCCM device.

Figure 7.3 shows typical current density-voltage (J-V) behavior for a-Si:H LCCM solar cells with this architecture. This device has a PCE of 8.2%, which is the highest reported to date for a nanostructured a-Si:H solar cell. Unlike other experimental results for a-Si:H cells with sub-wavelength features, the fill factor and open circuit voltage under AM1.5 G are very good. It is important to realize this is accomplished in spite of the enhanced electrode area to absorber volume ratio of the LCCM architecture.

### 7.3 Numerical Study

The performance of our cell can be further improved by optimizing the spacing  $L$ . The quantity  $A(\lambda)$  was numerically calculated by the full wave commercial code Ansoft HFSS. It is a 3-D Maxwell's equations solver. The optical properties of AZO, a-Si:H, and Ag, as a function of wavelength, were imported into HFSS. In our designs, light is incident through a glass superstrate of 1100  $\mu\text{m}$  thick. For simplicity, the glass superstrate was treated as a semi-infinite slab in each simulation. The reflection of light from the top of the glass is calculated assuming no multiple reflections. We are able to calculate light absorption in the a-Si:H. However, results were inspected for consistency by summing the absorption in all layers and comparing to the total absorption obtained from  $1 - \text{reflectance} - \text{transmittance}$ . The  $A(\lambda)$  information was converted into  $J_{SC}$  by assuming  $\text{IQE} = 1$  and utilizing Eq.7.1 as shown below.  $\Phi(\lambda)$  is the impinging light spectrum (AM1.5G) ; i.e.,

$$J_{SC} = \int_{\text{spectrum}} A(\lambda)\Phi(\lambda)d\lambda \quad (7.1)$$

While our analysis of carrier collection showed that we are limited to  $L > 910 \text{ nm}$  due to our pre-design of the planar parts, we varied  $L$  down to a 400nm spacing in this optical analysis.

Figure 7.4 summarizes the  $J_{SC}$  results. As may be seen, this modeling matches the experimental  $J_{SC}$  result we obtained rather well. As also may be seen, the modeling indicates that  $J_{SC}$  of  $\sim 15.7$   $\text{mA}/\text{cm}^2$  should be obtainable if the nano-column spacing was reduced to  $L=910\text{nm}$ , the minimum spacing permitted for full carrier collection. This would result in a 30 % increase in  $J_{SC}$  over that of the corresponding planar control.

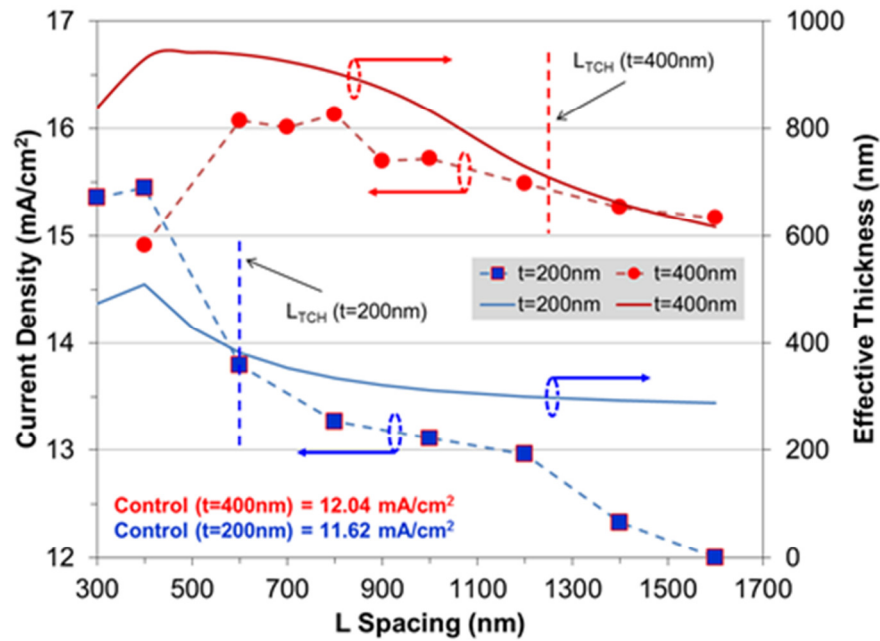


Figure 7.4. The computed short circuit current density  $J_{SC}$  as a function of  $L$  for structures with (1)  $t = 400$  nm,  $R = 473$  nm (Figure 7.1),  $R^* = 550$  nm (Figure 7.1), and  $h = 550$  nm and with (2)  $t = 200$  nm,  $R = 220$  nm,  $R^* = 220$  nm, and  $h = 500$  nm. Superimposed is the effective absorber thickness as a function of  $L$  for both thicknesses.

If the a-Si:H deposition was adjusted so that  $t$  was decreased to 200nm, the thickness of the a-Si:H conformal layer on the columns would then be about 150nm. This results in  $L_{COL} > L_{TEST}$  at  $L=L_{TCH}$ . As a consequence, truncated dome structures (Figure 7.1c) with  $L < L_{TCH}$  now become acceptable from a carrier collection perspective. In fact, a straightforward geometry

shows that the dome spacing can now be decreased until the lowest point of the domes is 500 nm above the AZO planar electrode. After a further assessment of the geometry, we found that it occurs when  $L=390$  nm and  $h=500$ nm. The  $J_{SC}$  was obtained based on the HFSS simulations for each variation of  $L$ . The result was plotted in Figure 7.4 for  $h=500$ nm. In Figure 7.4, the largest  $J_{SC}$  consistent with full carrier collection is observed to be  $\sim 15.5$  mA/cm<sup>2</sup>. This is a 33 % increase in  $J_{SC}$  over that of the corresponding planar control.

In order to have an insight into how much of the variation in  $J_{SC}$  shown in Figure 7.4 is due to photonic and plasmonic scatterings and how much is due to the variation in the volume of the absorber as demonstrated in Figure 7.1, an effective absorber thickness was calculated for the  $t=200$ nm and 400nm thickness cases and superimposed onto Figure 7.4. The effective thickness was defined by dividing the volume of the absorber by the base area. Surprisingly, the analysis of the effective absorber thickness shows that the variation of the absorber volume is playing the major role in the variation of the cell performance. This is different from our expectation that the photonic or plasmonic effects are the major factors. The enhancement increases with decreasing  $L$  for this superstrate design.

#### **7.4 Nanodomes for Thin Film Solar Cells on Substrate**

The periodic nanodomes in the superstrate cells were placed at the back end of the solar cells to provide diffuse reflections. As a result of the nanodome geometry at the back end, the conformal back electrode is also a periodic curvy structure that may cause plasmonic effects. The additional plasmonic effects can further increase light absorption in the absorber layer but may also introduce undesirable ohmic loss. As an alternate design, the nanodome structure can also be placed at the front end of solar cells. The design is shown in Figure 7.5.

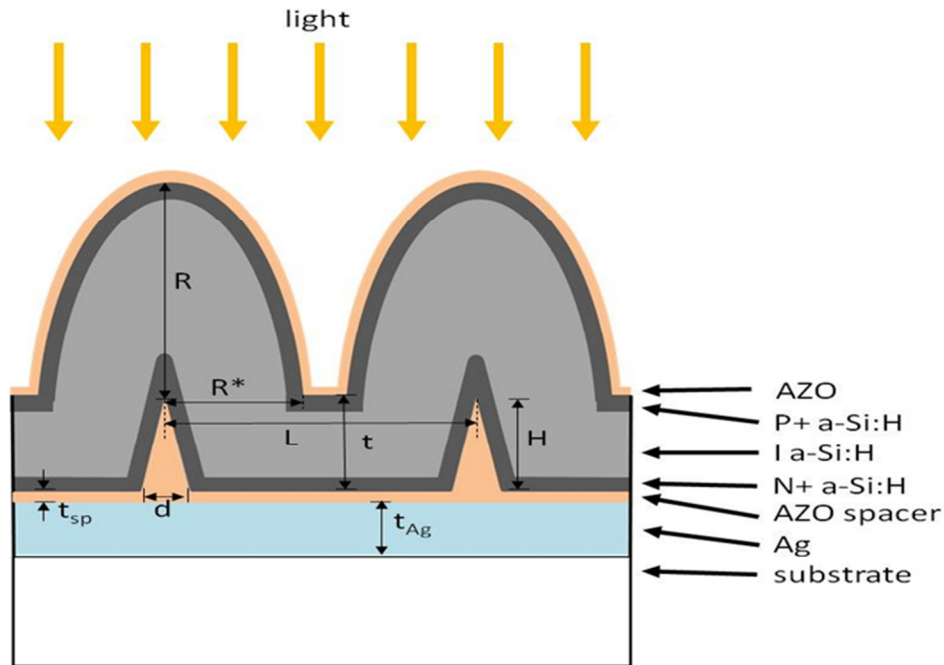
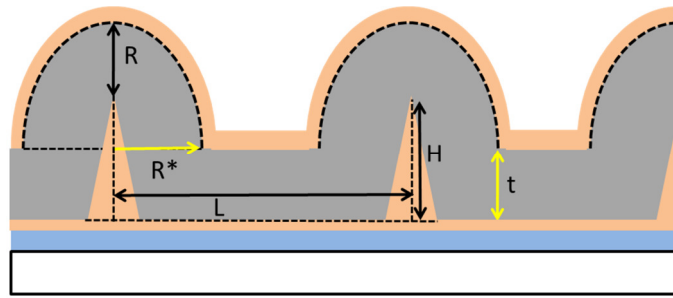


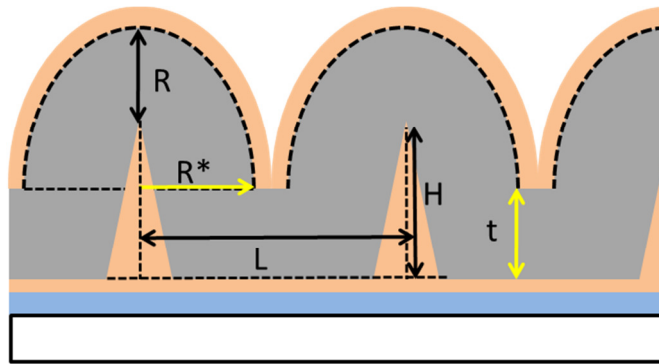
Figure 7.5 The schematic of the substrate nanodome solar cell.

The Si layer is shaped into periodic nanodomies, sitting on a flat Ag back electrode. The front spacer is conformal to the a-Si layer. The periodic AZO cones are sitting on the back spacer to improve carrier transport, just like the AZO columns in the superstrate cells. The cones are expected to introduce more scatterings than columns. The dimensions of the nanodomies and cones are configured based on our experience with the superstrate cells. These dimensions are also able to be fabricated. The periodic spacing between each neighboring domies is optimized by numerical simulations. The two parameters that change with the varying spacing are the effective thickness of a-Si and the curvature height of domies. In Figure 7.6, we show the schematics of the nanodome substrate cell at three different spacings.

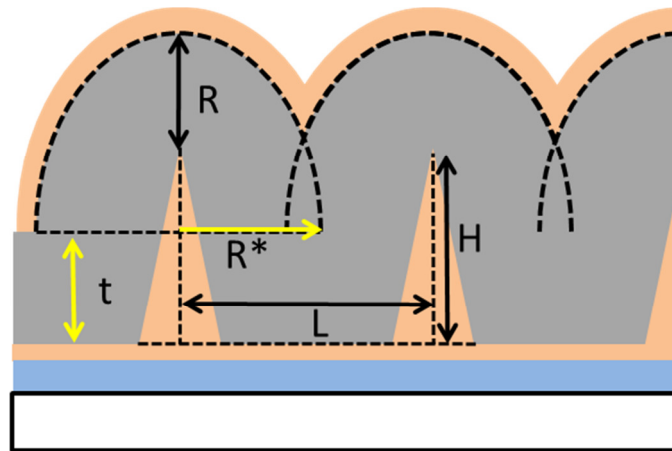




(a)



(b)

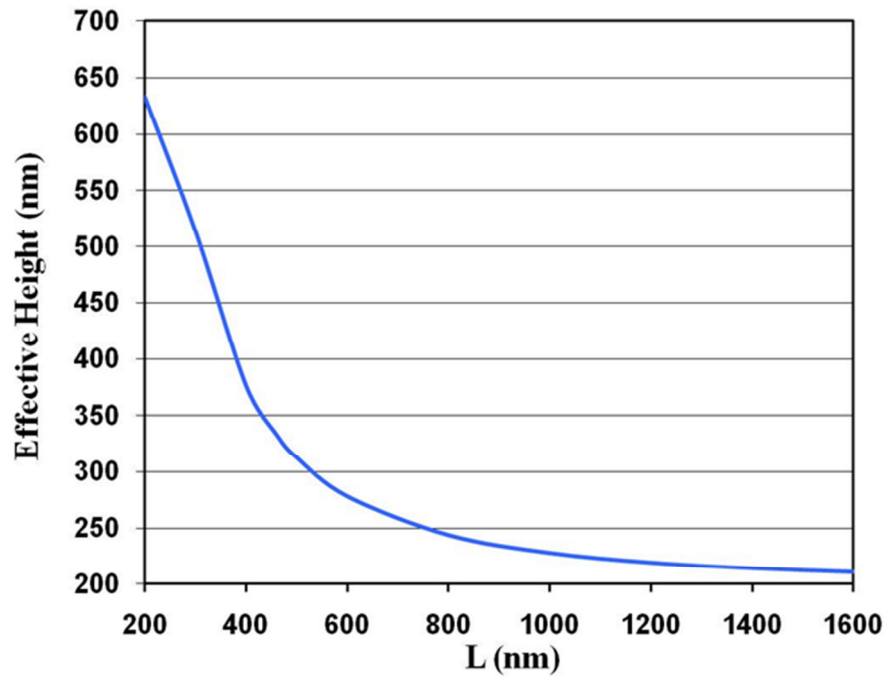


(c)

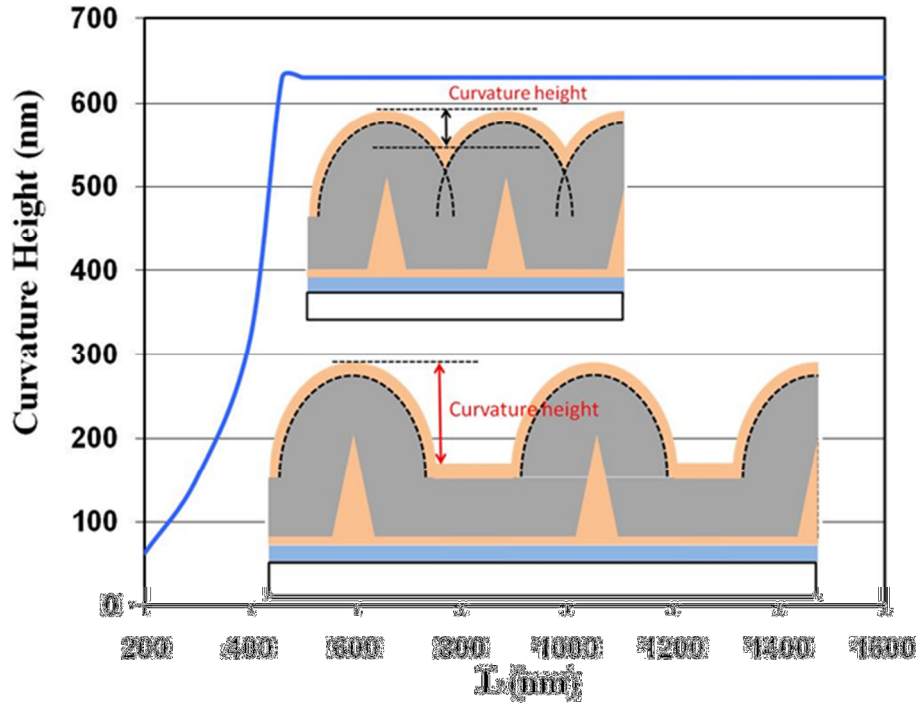
Figure 7.6 The schematics of the nanodome cells on a substrate for (a)  $L > L_{touch}$ ; (b)  $L = L_{touch}$ ; (c)

$L < L_{touch}$ .

In Figure 7.6b, the spacing  $L=L_{touch}$  and the domes are just touching each other. When  $L < L_{touch}$ , the domes are merging into each other. As a result, the effective a-Si thickness will be greater than the  $L=L_{touch}$  case. However, the domes become flatter and the curvature height is smaller. When  $L > L_{touch}$ , the curvature height is the same as the  $L=L_{touch}$  case but the effective a-Si thickness is smaller. The detailed effective a-Si thickness and curvature are shown in Figure 7.7 with respect to the spacing “ $L$ ”.



(a)



(b)

Figure 7.7 (a) The effective thickness of a-Si:H with respect to the dome-to-dome spacing  $L$ . (b) The curvature height of the nanodome cell with respect to  $L$ . Insets are the schematics showing the definition of curvature height.

In Figure 7.7, the effective a-Si thickness drops very quickly when  $L$  increases from 200 nm to 800 nm. The curvature height of domes is constant when  $L$  is greater than  $L_{touch}$  (460 nm). The planar region between each two domes increases with the increasing  $L$ . As a result, the effective a-Si thickness decreases with the increasing  $L$ . When  $L < L_{touch}$ , the curvature height drops quickly with the decreasing  $L$ . The absorption of the nanodome solar cell is the combined effect of the effective a-Si thickness, the curvature height of the domes and the photonic effect adjusted by the periodic spacing of domes.

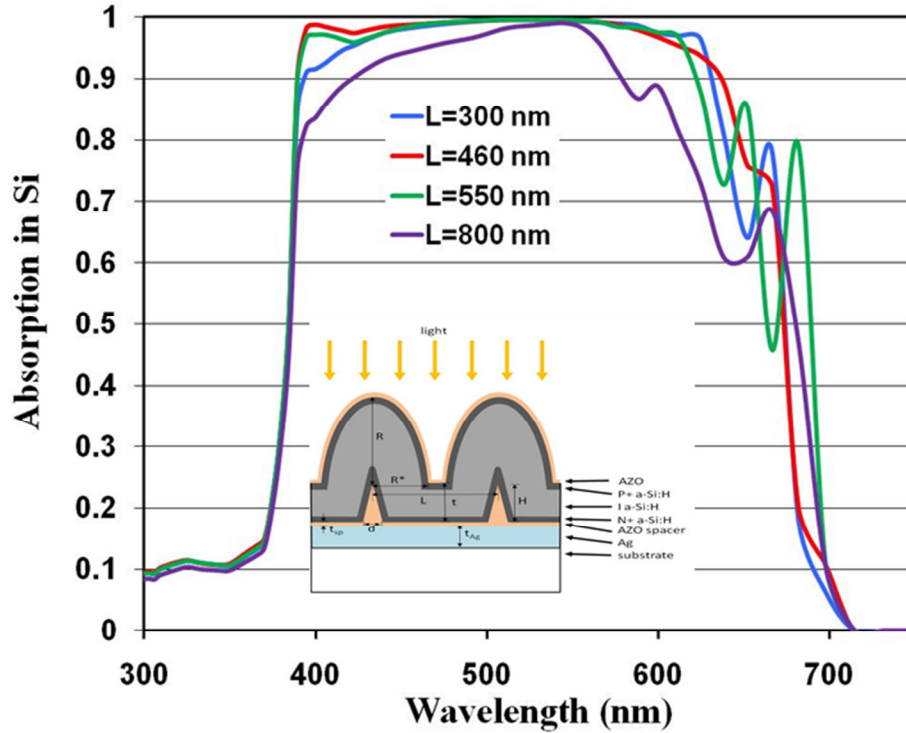


Figure 7.8 The absorption in the a-Si:H layer for the nanodome cell with different spacings.

In Figure 7.8, we show the absorption spectrum for the nanodome solar cells with selected  $L$  values.  $L=300$  nm is the smallest spacing we have tried in simulations.  $L=460$  nm results in the fact that the domes touch each other.  $L=800$  nm is the cells with the largest spacing in our study. Each cell exhibits absorption peaks in the band gap region (600 nm to 700 nm). The locations of these peaks vary from cell to cell. The absorption of  $L=800$  nm cell at wavelengths shorter than 600 nm is worse than the other cells. This is due to the fact that its effective a-Si thickness is smaller than the cells with smaller spacings. In Figure 9.3a, the effective a-Si thickness of the  $L=800$  nm cell is only 250 nm while the effective a-Si thickness of the  $L=400$  nm cell is 350 nm. The short wavelength absorption is not sensitive to the effective thickness when  $L$  is less than 600 nm. The curvature height plays a more important role in determining the  $J_{sc}$  of the solar cell. The cell with  $L=500$  nm exhibits two peaks within the

spectrum between 600 nm and 700 nm while other cells exhibit only one peak. As a result, the  $J_{sc}$  of the cell with  $L=500$  nm is higher than other cells as shown in Figure 7.9.

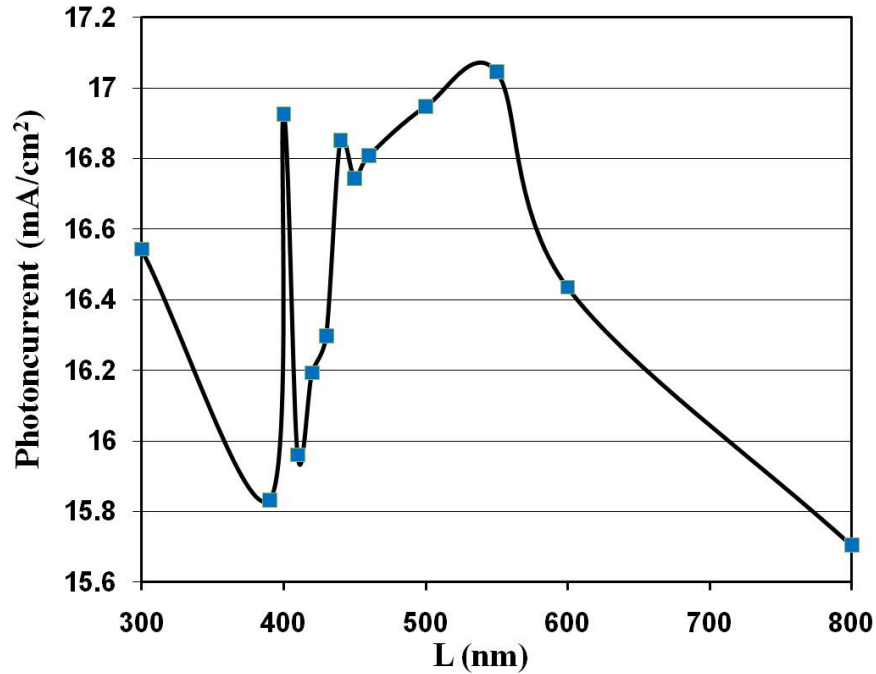


Figure 7.9 The calculated  $J_{sc}$  with respect to spacings.

The maximal  $J_{sc}$  of 17.09 mA/cm<sup>2</sup> is obtained when  $L=550$  nm. The  $J_{sc}$  goes down with the decreasing  $L$  down to  $L=390$  nm except the spike at  $L=400$  nm where the  $J_{sc}=16.92$  mA/cm<sup>2</sup>. When  $L=400$  nm, the absorption of the cell exhibits a peak at  $\lambda=700$  nm where the number of incoming photons from sunlight are more than the other wavelengths beyond the bandgap (300 nm to 700 nm). When  $L<390$  nm, the  $J_{sc}$  increases with the decreasing  $L$  due to the increasing effective thickness of a-Si. As shown in Figure 11.3a, the effective a-Si thickness increases from 350 nm ( $L=400$  nm) to 625 nm ( $L=300$  nm), an increase of 78.6%. When  $L>600$  nm, the  $J_{sc}$  decreases with the increasing  $L$  because the insufficient a-Si thickness.

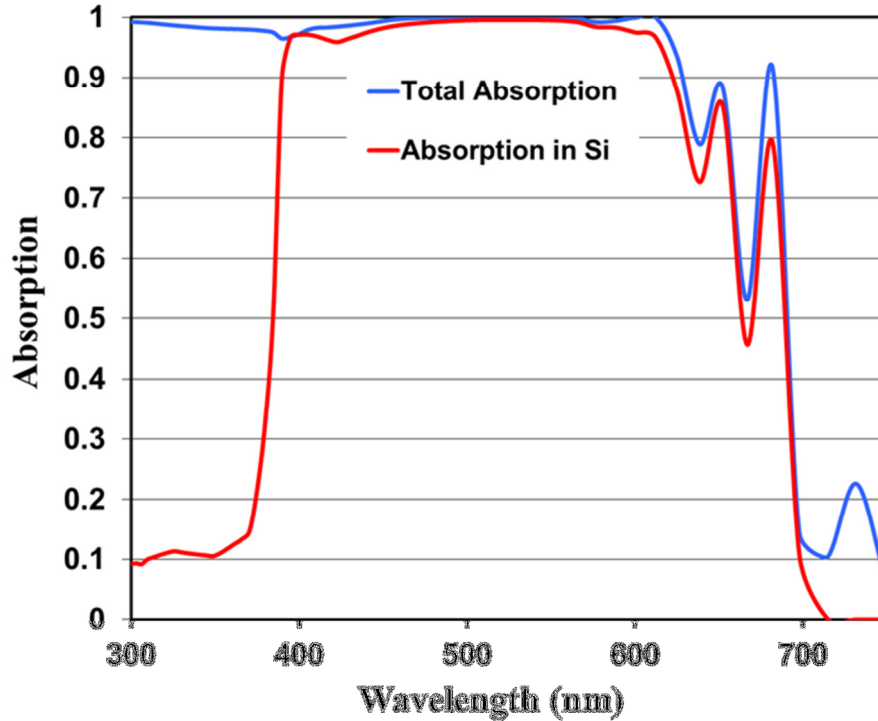


Figure 7.10 The absorption of the optimized nanodome cell with  $L=550$  nm. The total absorption is the absorption of the cell. The absorption in Si accounts for the energy only absorbed by the a-Si:H layer.

The absorption spectrum of the optimized cell with  $L=550$  nm is shown in Figure 7.10. The two peaks at  $\lambda=652$  nm and  $\lambda=681$  nm are due to the nanodomains. Comparing the total absorption with the absorption in the a-Si, we find over 90% of the enhanced absorption contributes to the useful absorption in the a-Si. There is a peak at  $\lambda=731$  nm where the absorption coefficient of a-Si is 0. The enhanced cell absorption at this wavelength does not contribute to the absorption in the a-Si layer. Instead, it is present in terms of heated loss in other layers.

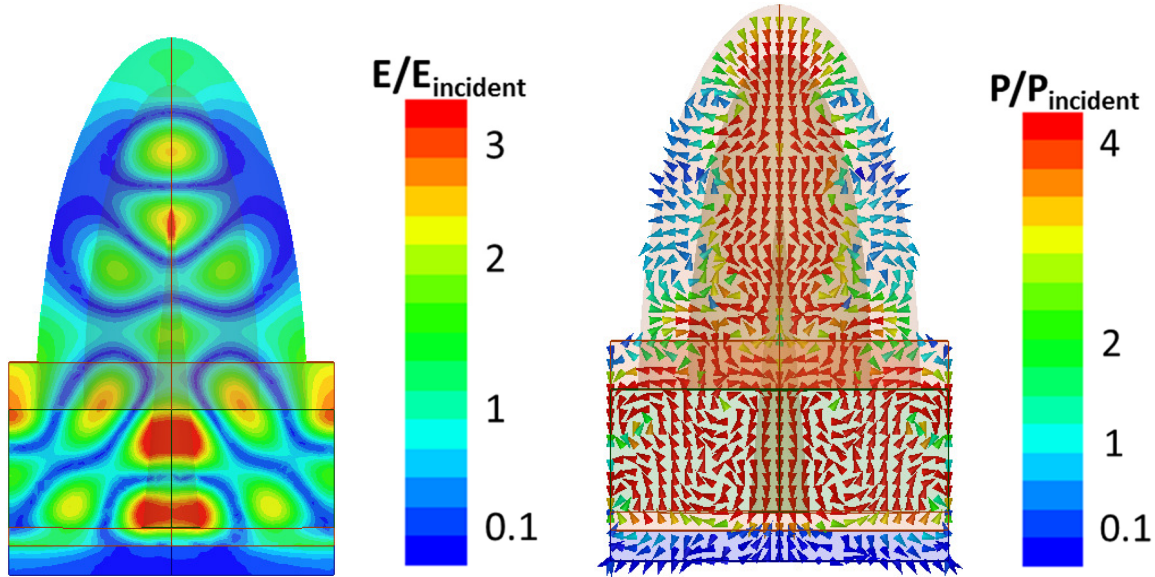


Figure 7.11 (a) The localized electric field and (b) the Poynting vectors of the optimized cell at  $\lambda=681$  nm.

We show in Figure 7.11 the localized electric field and Poynting vectors within the cell at  $\lambda=681$  nm. The localized electric field exhibits a symmetrical distribution within the cell because the nanodomes are symmetric. The intensity of electric field at the tip of the AZO cones is high compared to its neighboring region. The Poynting vectors exhibit enhanced intensity compared to the incident Poynting vectors. The incoming photons are refracted into the cell and undergo high reflections at the boundary between a-Si and AZO. As a result, most of the photons are trapped within the a-Si part and are finally absorbed.

The  $J_{sc}$  of the above mentioned a-Si nanodome solar cells is limited by the bandgap of a-Si:H ( $\sim 700$  nm). The record  $J_{sc}$  for a-Si single junction solar cells is  $18 \text{ mA/cm}^2$  while commercial c-Si single junction solar cells achieve  $30 \text{ mA/cm}^2$  of  $J_{sc}$ . Due to the cost per watt of a-Si:H thin film solar cells does not show obvious advantages over conventional wafer cells. The

18 mA/cm<sup>2</sup> record is achieved with advanced light trapping designs in lab conditions. The issues with cost and large scale fabrication of such cells are still unsolved. In order to further increase the  $J_{sc}$  of thin film solar cells, we should go for thin film materials that have lower energy levels for band gaps. nc-Si is such a material. Unlike a-Si whose bandgap is  $\sim 700$  nm, nc-Si exhibits its bandgap at  $\sim 1000$  nm. Hence, the infrared absorption of nc-Si is better than a-Si.

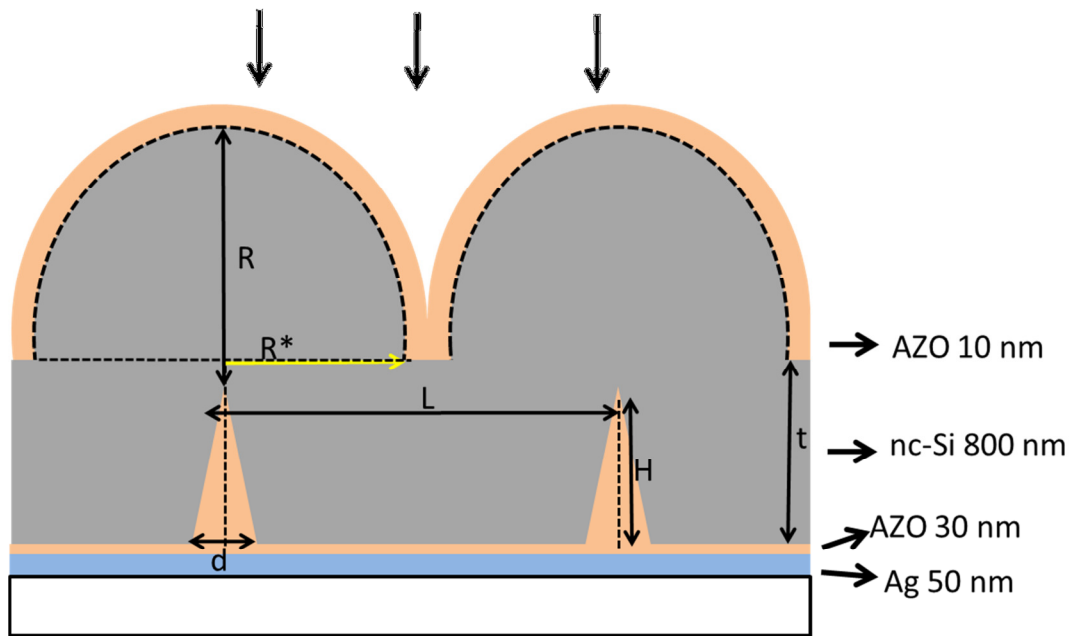


Figure 7.12 The schematic of the nc-Si nanodome cell on a substrate.

The design of the nc-Si nanodome solar cell is shown in Figure 7.12. The substrate designs are used here. The nc-Si domes are on the front end of the cells. The planar nc-Si layer is 600 nm or 800 nm. The periodic spacing  $L$  is studied to optimize the  $J_{sc}$  of the cells.



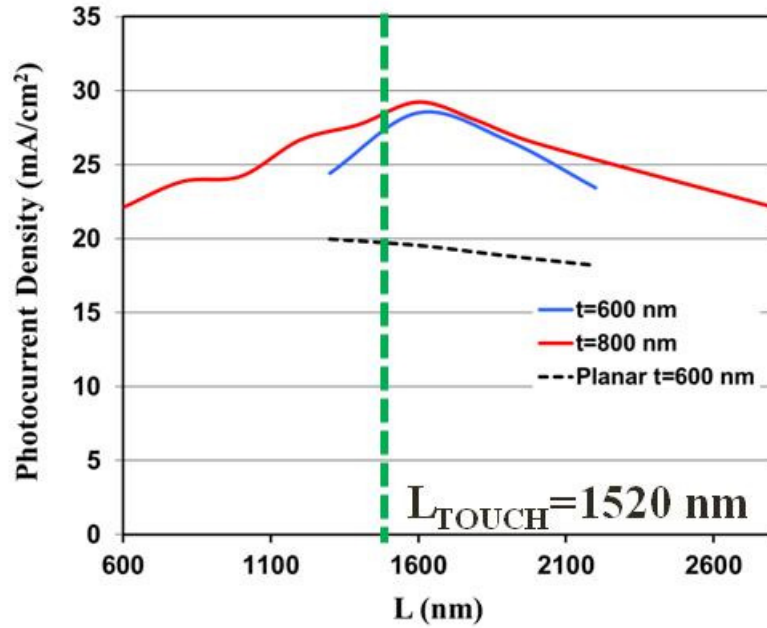


Figure 7.13 The calculated  $J_{sc}$  of the nc-Si nanodome substrate cell with respect to spacings.

In Figure 7.13, the  $J_{sc}$  is shown with respect to  $L$ . The maximal  $J_{sc}$  for  $t=600$  nm and  $t=800$  nm is obtained when  $L$  is slightly greater than  $L_{touch}$ . The maximal  $J_{sc}$  for  $t=600$  nm and  $t=800$  nm is  $28.51 \text{ mA/cm}^2$  and  $J_{sc}=29.23 \text{ mA/cm}^2$ , respectively. The cells with  $t=800$  nm exhibit the maximal  $J_{sc}$  that is only 2.5% higher than the cells with  $t=600$  nm, although the effective thickness of the  $t=800$  nm cells is 200 nm more than the  $t=600$  nm cells. Hence, the thickness of the planar region is not critical to achieve a high  $J_{sc}$ .

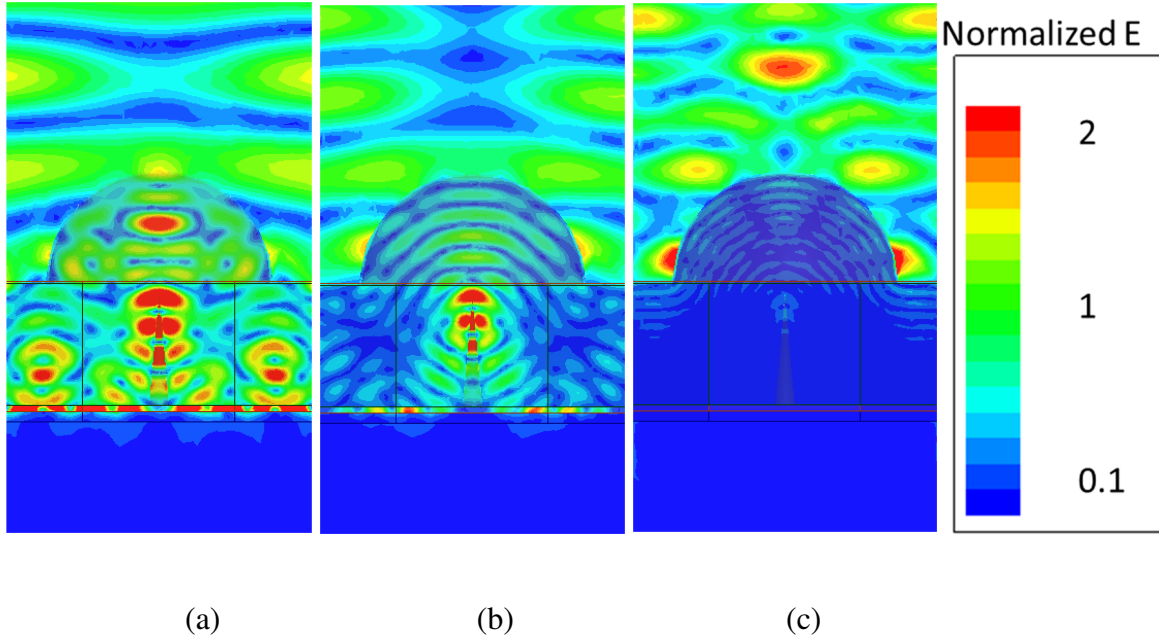


Figure 7.14 The localized electric field in the optimized cell at (a)  $\lambda=882$  nm; (b)  $\lambda=750$  nm; (c)  $\lambda=500$  nm.

Figure 7.14 shows the localized electric field in the  $t=600$  nm cell when  $L=1600$  nm. The incident light is bent into the active layer for a larger light path. Since the absorption coefficient of nc-Si is much higher at short wavelengths than long wavelengths, the attenuation of light in nc-Si at short wavelengths is much higher than long wavelengths. Hence, the light path at long wavelengths has to be much greater than short wavelengths in order to achieve comparable absorption. In Figure 7.14, the AZO cone acts as a scatterer for the bent incident light. The localized field at the tip of the AZO cone is always strong at all wavelengths. Due to the multiple passes of light within the active layer at short wavelengths, the resulting field shows irregular distributions of constructive interferences. The irregular field pattern, however, is symmetric due to the symmetric geometry of domes. The light path at long wavelengths is much easier to trace because the high attenuation allows the light travels within a limited amount of passes.

## VIII. Blazed Grating for Light Trapping in Thin Film Solar Cells

### 8.1 Background

Light absorption in TFSCs can be enhanced by using a randomly textured rough surface that scatters light in random directions [72]. This design can be implemented by the Asahi U-type process at a low cost, but the absorption enhancement is limited by the second law of thermodynamics. Grating designs have been proposed to overcome the limit of random texturing designs. Light incident on a grating will be directed to particular angles unlike diffuse scattering by a random rough surface. Therefore, the enhancement of the light path can be controlled by adjusting the scattering pattern of a grating. The grating designs have periodic arrangements of regular geometries and can enhance absorption in TFSCs [73-77]. Heine and Morf [74] experimentally demonstrated that a blazed grating increases the effective Si thickness by a factor of 5 for a solar cell more than 5  $\mu\text{m}$ . Gjessing *et. al.* [73] did a numerical study of advanced grating designs to find the best geometry for light trapping in a 20  $\mu\text{m}$  Si solar cell. Fourier optics was employed to design the scattering pattern in the far field Fraunhofer region [78]. Light trapping by grating structures have also been studied in microcrystalline Si solar cells whose absorber thickness varies from 1 $\mu\text{m}$  to 3 $\mu\text{m}$ . Madzharov *et.al.* studied the groove grating in the front and back end of a solar cell [76]. Haase and Stiebig [77] predicted asymmetric geometries would result in better light trapping. This idea was then proved by the numerical study in [75] and the best design yielded a  $J_{sc}$  close to the Lambertian limit. The Fourier optics study of gratings, however, does not apply to the near field Fresnel region. For a-Si:H TFSCs with absorber layer thickness less than 500nm as studied here, the absorber layer is in the near field Fresnel region of the grating. This problem has not been well studied in the current literature.

In this section, we propose using the AZO blazed gratings as the back spacer layer for a-Si:H and nc-Si TFSCs. Full wave, finite element simulations were employed for an accurate computation of light absorption in the semiconductor layer. We have demonstrated a great enhancement of  $J_{sc}$  compared to planar cells containing the same volume of a-Si:H. The optimized designs were studied for different polarization states and at different angles of incidence.

## 8.2 Design of 1D Gratings in Thin Film Solar Cells

The refractive index of a-Si:H is approximately 4 and the longest wavelength in a-Si is  $700 \text{ nm}/4 = 175 \text{ nm}$ . The typical ratio between the thickness of the a-Si:H absorber layer and the longest wavelength in a-Si below its bandgap is  $\sim 1 - 3$ . Hence, light absorption within the a-Si:H layer is dependent on the near field pattern of the waves scattered by the blazed grating. It is desirable to have more light scattered at angles that are higher than the critical angle at the upper a-Si – AZO interface, so that all such light will undergo total internal reflection back into the absorber layer. The near field scattering pattern is dependent on both the magnitude and phase of the scattered waves from each wedge of the blazed grating. The Fresnel diffraction pattern of a general rough surface in Cartesian coordinates ( $x, y, z$  system) is represented by [78]:

$$\Psi = \frac{ik_0 A}{2\pi z} \iint_R f(x, y) e^{\frac{ik_0}{2z}(x^2 + y^2)} dx dy \quad (8.1)$$

Where  $A$  is the amplitude coefficient,  $R$  is the rough surface and  $f(x, y)$  is the profile function of the rough surface.  $\psi$  is the amplitude of the scattered light at the observation point and  $k_0$  is the wavenumber in the scattering medium. The profile of the rough surface is described by its profile function  $f(x, y)$  and it is the determinant of the scattering pattern. There is no analytical solution for Eq. 8.1 and it can be solved only by numerical methods.

We selected the asymmetric wedge - shaped geometry for each element of the grating in order to scatter light at large angles. An asymmetric geometry has been proved to have a higher efficiency for light scattering at large angles [73]. We first study from a 1D grating as shown in Figure 8.1 in which the periodic elements are repeated in only one direction. The AZO grating stands on top of the Ag back electrode and the a-Si:H fills the space left by the AZO grating. An additional 50 nm a-Si:H thin film is deposited on top of the grating. An AZO thin film serves as the top passivation layer and as the top transparent conducting electrode (TCO). The volume of a-Si:H increases with increasing angle of each wedge, as well as the increasing period of the grating.

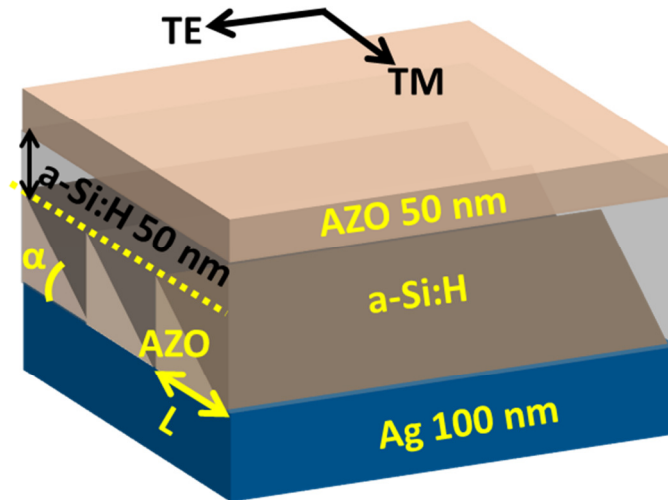


Figure 8.1. The schematic of the 1D grating design. The plane wave is normally incident on the cell with TE or TM polarization.

### 8.3 Fabrication of the Grating Structure

The fabrication of grating structures becomes difficult when the space between the grating elements is less than  $1\mu\text{m}$ . The nanoimprinting technique combined with the standard

KOH etching process can be employed to fabricate grating patterns on crystalline silicon with very high surface quality [79]. The grating elements can be grooves or wedges. This technique, however, does not apply to our case because AZO is not a crystalline material.

AZO nanogroove gratings have been fabricated by Isabella *et. al.* using both the patterning technique and the hot embossing technique [80]. Silicon dioxide ( $\text{SiO}_2$ ) was deposited on a glass substrate and the grating pattern was stamped onto the  $\text{SiO}_2$  by raising the temperature to the point where it is just above the glass transition temperature. A wedge shaped grating can also be fabricated by depositing AZO patterned areas at a glancing angle [81]. In Figure 8.2, the process starts with a flat glass substrate. The substrate is coated with a thin layer of Ti and followed by photoresist. The photoresist is developed using a mask with periodic nanoholes of the appropriate shape (square, rectangle, circular). The AZO film is then deposited onto this patterned photoresist by DC sputtering or Atomic Layer Deposition. In order to implement a thickness gradient and form the wedge shape, the substrate is tilted so that the incoming AZO flux is obliquely incident on it. The AZO flux is partly blocked by the height of the photoresist. Hence, a thin AZO film with thickness gradient is formed.

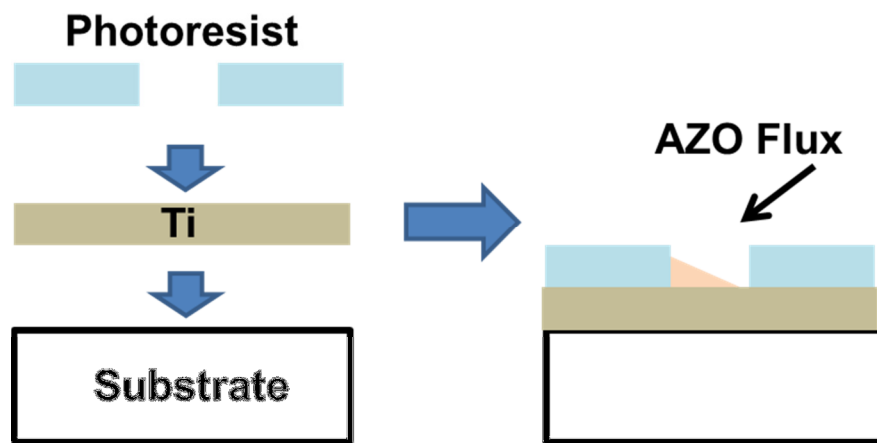


Figure 8.2. The schematic for the glancing angle deposition process to fabricate the AZO grating.

## 8.4 Results and Discussions

In order to study the light trapping effectiveness of the blazed grating structure, we performed full wave simulations using the finite element commercial code HFSS. It is a 3D electromagnetic solver well recognized among researchers. The finite element method (FEM) is very accurate when the feature size is subwavelength. A plane wave is normally incident on the solar cell with the TE or TM polarization states as shown in Figure 8.1. A practical a-Si:H thin film solar cell is made up of a *p-i-n* junction. Typically, the intrinsic layer thickness is about 90% of the total thickness. The difference in the optical properties of the doped and undoped regions is negligible when the doping levels are less than  $10^{18} \text{ cm}^{-3}$  [82]. Thus, it is customary to model the optical response assuming the entire Si region with the wavelength dependent complex refractive index of the intrinsic layer. We performed a parametric study to find the optimal wedge angle  $\alpha$  and period or spacing  $L$  in Figure 8.2 to achieve the highest  $J_{sc}$  for TE polarization while maintaining the effective Si thickness of the intrinsic region to be less than 300 nm. The carrier collection length of an a-Si:H *p-i-n* junction is around 300 nm [19], which means that the probability for carrier recombination in a-Si:H is low when the effective thickness ( $h_{eff}$ ) is less than 300 nm.

We calculated the absorption  $A_{Si}$  in the a-Si:H layer according to Poynting's theorem:

$$A_{Si} = \frac{1}{2} \int_{Si} \frac{2\pi c}{\sqrt{\epsilon'}\lambda} \epsilon'' |E|^2 dV \quad (8.2)$$

$c$  is the velocity of light in free space,  $\lambda$  is the free space wavelength,  $\epsilon'$  and  $\epsilon''$  are the real and imaginary part of the permittivity of a-Si:H.  $|E|$  is the magnitude of the local electric field in the a-Si:H. We obtained the local field from the simulations and then integrated this value over the volume of the a-Si:H. The  $J_{sc}$  can then be calculated using the following well known equation:

$$J_{sc} = \int_{\lambda} eA(\lambda)\Phi_0(\lambda)d\lambda \quad (8.3)$$

$A(\lambda)$  and  $\Phi_0(\lambda)$  are the wavelength dependent light absorption in a-Si:H and the number of incident photons, respectively. We assumed 100% internal quantum efficiency and used the AM 1.5G standard as the incident solar spectrum to calculate  $J_{sc}$ .

In Figure 8.3, we show the calculated  $J_{sc}$  with respect to the varying  $\alpha$  and  $L$ . The enhancement is not prominent until  $\alpha$  is greater than  $20^\circ$  and  $L$  is greater than 400 nm. In general, we obtain a higher  $J_{sc}$  with a set of higher  $\alpha$  and  $L$ , which leads to a large volume of the a-Si:H absorber. However, the geometry of the grating also plays a role as we have the local maxima at point 1, 2 and 3. The dimensions of the grating at point 1, 2 and 3 have been tailored to: 1) scatter more light at angles greater than the critical angle at the top surface; 2) produce stronger constructive interferences within the a-Si:H.

The dimensions at the three points are: 1) point 1:  $L=400$  nm,  $\alpha=30^\circ$ ,  $h_{eff}=165$  nm; 2)  $L=500$  nm,  $\alpha=25^\circ$ ,  $h_{eff} =167$  nm; 3)  $L=650$  nm,  $\alpha=35^\circ$ ,  $h_{eff} =277$  nm. The effective a-Si:H thickness for point 1,2 and 3 are 165 nm, 167 nm and 277 nm, respectively. The  $J_{sc}$  enhancement at 1 and 2 is high but it is due to the small  $J_{sc}$  from the 165 nm thick planar cells. Moreover, the enhancement is also very sensitive to the geometry of the grating. Point 3 is preferred due to a finite area with the same  $J_{sc}$  that results in a higher fabrication tolerance for  $\alpha$  and  $L$ . The  $J_{sc}$  varies by only 8% when  $\alpha$  is changed by  $\pm 5^\circ$  and  $L$  is changed by  $\pm 50$  nm from point 3.



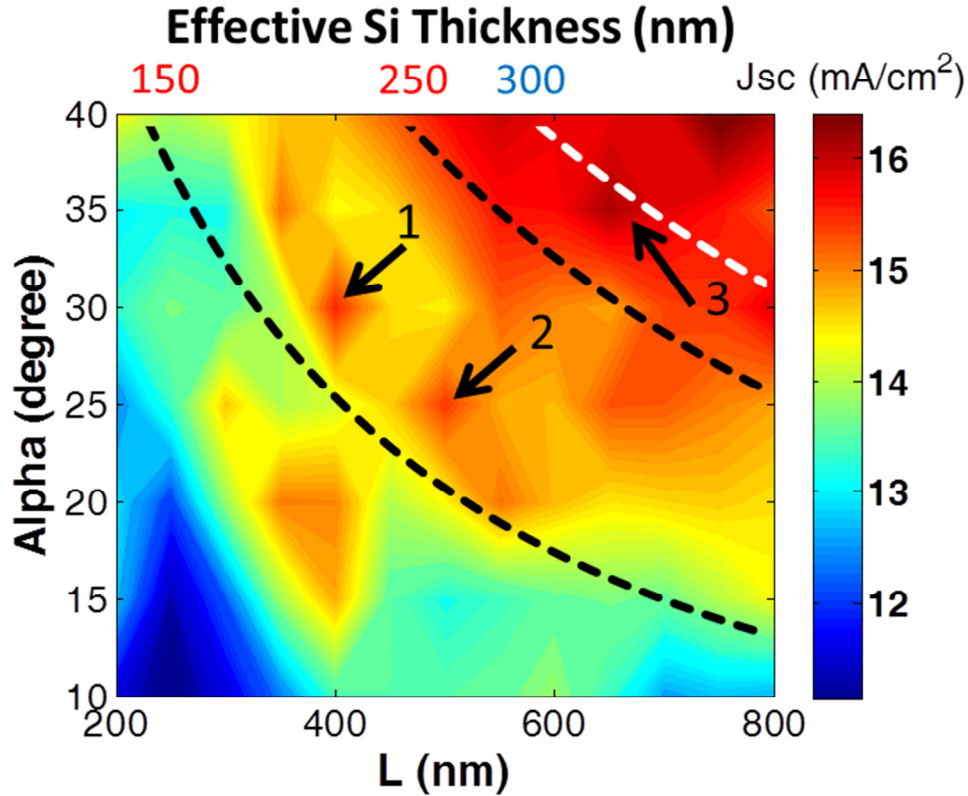


Figure 8.3. The color map showing the parametric study of  $J_{sc}$  with respect to  $\alpha$  and  $L$ . Three local maxima of  $J_{sc}$  are marked as points 1, 2 and 3. The dashed lines represent an effective thickness of 150 nm, 250 nm and 300 nm respectively. The minority carrier collection length is  $\sim 300$  nm and at this effective thickness (top right corner),  $J_{sc}$  is  $>15.5$  mA/cm<sup>2</sup>.

The absorption spectrum of the three local maxima is shown in Figure 8.4. The short wavelength absorption at points 1 and 2 is slightly lower than point 3 due to the lower volume of a-Si:H. The absorption at points 1 and 2, however, does not show disadvantages over point 3 for wavelengths longer than 600 nm, although the effective a-Si:H thicknesses of points 1 and 2 are only 60% of point 3. It seems the light absorption at the working wavelengths of a grating is less sensitive to the volume of the absorber. We observe from the parametric study that all the numerical full wave simulations are in the Fresnel region of the grating, we, nevertheless, obtain

trapping of light in the a-Si region for wedge angles that are greater than the critical angle at the upper a-Si –AZO interface.

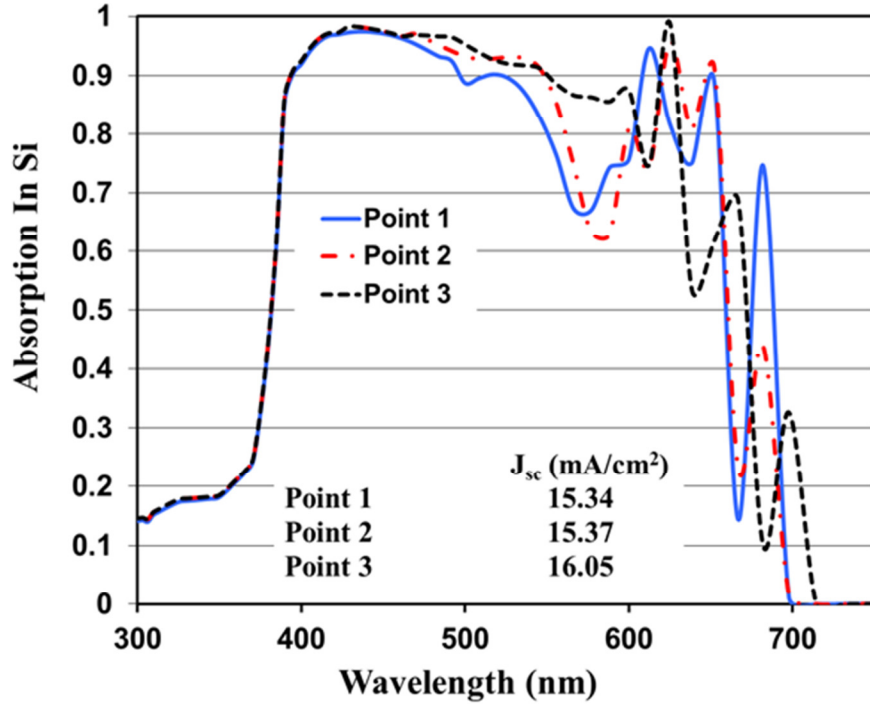


Figure 8.4. The absorption spectrum of the three local maxima points identified in Figure 8.3. Inset is the calculated  $J_{sc}$  of each case assuming ideal carrier transport.

We select the design at point 3 as our optimized design because it yields the highest  $J_{sc}$  with an effective a-Si:H thickness less than 300 nm. Simulations were run for TE and TM polarization of the incident light, in order to study the polarization dependence of the optimized blazed grating design. We note that the planar solar cell is independent of polarization, but the blazed grating TFSC is nominally dependent on the incident polarization. We note that sunlight is unpolarized.

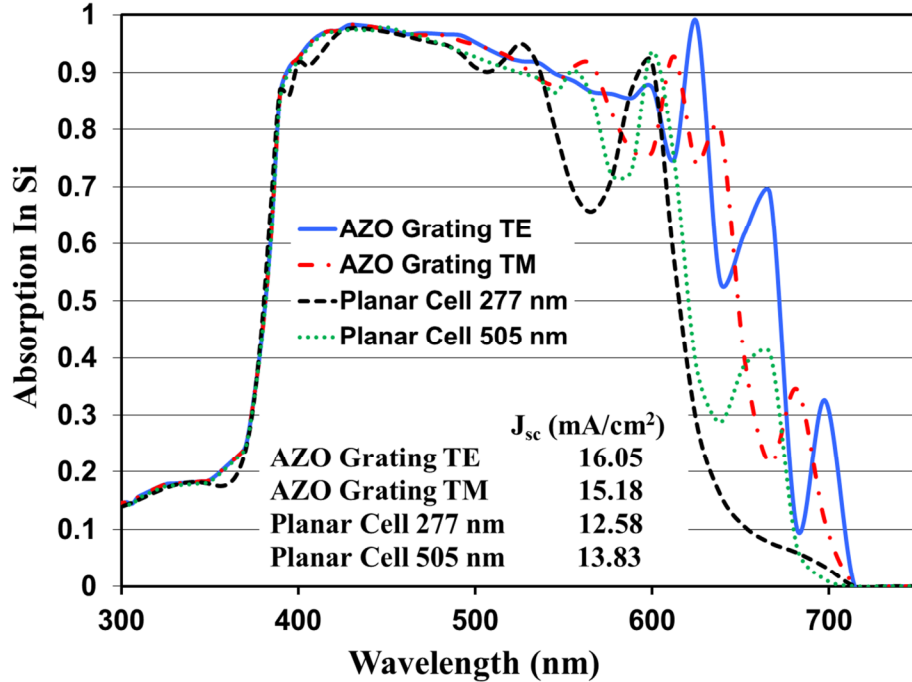


Figure 8.5. The absorption spectrum of the optimized design ( $L=650$  nm,  $\alpha=35^\circ$ ) at normal incidence for TE and TM polarizations and comparison to a planar cell with 277 nm and 505 nm a-Si:H. The effective thickness of the cell is 277 nm and the resulting a-Si:H thickness is 505 nm if the AZO grating region is filled with a-Si:H. Inset is the calculated  $J_{sc}$  for each case. The enhancement of the  $J_{sc}$  for TFSC with grating is 27.6%.

In Figure 8.5, the grating design shows an enhancement of light absorption at wavelengths longer than 540 nm for both TE and TM polarization. The absorption for the TM polarization is slightly lower than the TE polarization, resulting in a 4.8% reduction in  $J_{sc}$ . The planar cell we used for comparison has the same front spacer thickness as the grating cell. The thickness of the a-Si:H layer and the back spacer layer of the planar cell is the same as the effective thickness of their counter parts in the grating cell. In figure 5, the thickness for the a-Si:H layer and the back spacer layer of the planar cell is 277 nm and 114 nm, respectively.

Compared to a 277 nm thick planar cell, the optimized 1D grating enhances  $J_{sc}$  by 27.6% for the TE polarization and 20.7% for the TM polarization, respectively. If the AZO grating region is filled with a-Si:H, the resulting cell will be planar with an active layer of 505 nm thick. It is easier to fabricate a planar cell with a 505 nm-thick active layer than inserting a grating design. The AZO grating design is preferable only when its resulting performance is better than a planar cell with a 505 nm-thick active layer. In Figure 8.5, the grating design enhances the  $J_{sc}$  by 16.05% compared to a planar cell with a 505 nm-thick active layer, although the AZO grating accounts for a volume loss of 45.15%. The surface area of the active layer with the AZO grating increases by only 11%. This amount of increase in surface area is very small compared to other designs that have been proposed and the resulting increase in surface recombination is expected to be much smaller. We also observe that the grating structure does not cause any deterioration in the absorption below 540 nm and the absorption at shorter wavelengths mimics the planar solar cell for both polarizations.

In Figure 8.6, we show the distribution of energy density within the a-Si:H layer at  $\lambda=697$  nm,  $\lambda=667$  nm and  $\lambda=625$  nm, respectively. The three wavelengths correspond to the three peaks in the absorption curve (TE polarization). The energy density is calculated by the integrand in equation 2. We assume the incident electric field intensity is 1V/m. The plots of energy density are directly related to the absorption and are more straightforward than the plots of electric field. The localized “hot spots” are due to the constructive interferences among the scattered waves. The energy density at  $\lambda=697$  nm is much smaller than  $\lambda=667$  nm and  $\lambda=625$  nm because the absorption coefficient of a-Si:H at  $\lambda=697$  nm is much smaller than the other two wavelengths. This observation agrees with the absorption spectrum shown in Figure 8.5. The calculated absorption in a-Si:H at  $\lambda=697$  nm is much smaller than  $\lambda=667$  nm and  $\lambda=625$  nm. The locations

of the hot spots vary at different wavelengths due to the variation of the scattered patterns. Some hot spots are in the vicinity of the top and bottom of the a-Si:H layer but these spots are in the doped  $p$  and  $n$  regions and any electron-hole pairs generated in these regions have a higher probability of recombination. The thickness of the doped layers varies with different manufacturers. The typical thickness for the  $p$  region (on top) is from 10 nm to 20 nm and the typical thickness for the  $n$  region (at the bottom) is from 20 nm to 50 nm. In Figure 8.6, most of the hot spots are in the middle of the a-Si:H layer.

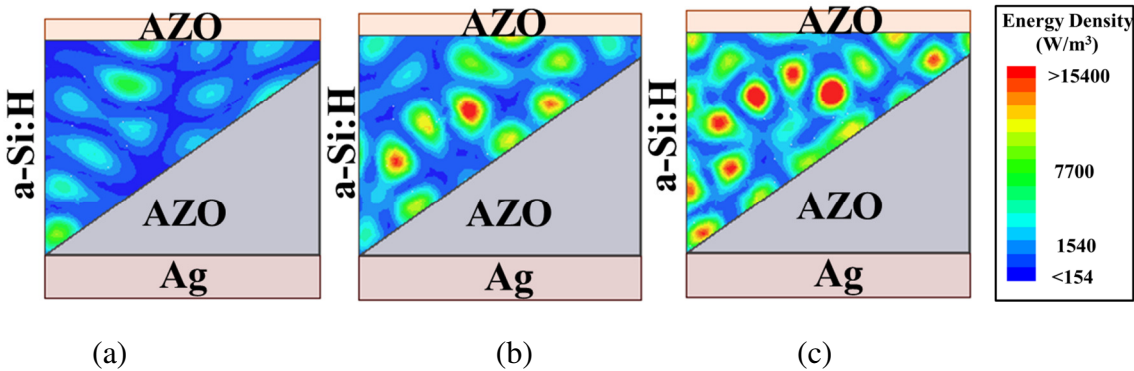


Figure 8.6. The plots of the calculated energy density across the a-Si:H region at wavelengths (a)  $\lambda=697$  nm, (b)  $\lambda=667$  nm and (c)  $\lambda=625$  nm. The incident electric field is 1 V/m.

We studied the  $J_{sc}$  of the optimized 1D grating design by scanning the angle of incidence from  $-45^\circ$  to  $45^\circ$  according to the definition in the inset of Figure 8.6. Because we use asymmetric wedge geometry for each grating element, it is necessary to study the angle of incidence from both sides of the normal. Only TE polarization is studied here.

In Figure 8.7, the calculated  $J_{sc}$  is very stable when the incidence angle is within  $\pm 30^\circ$  off the normal line. Compared to the  $J_{sc}$  at normal incidence, the  $J_{sc}$  at  $30^\circ$  incidence is degraded by

only 2% mainly due to the increasing front surface reflection at oblique incidence. Hence the grating design is very stable with the varying angles of the incidence.

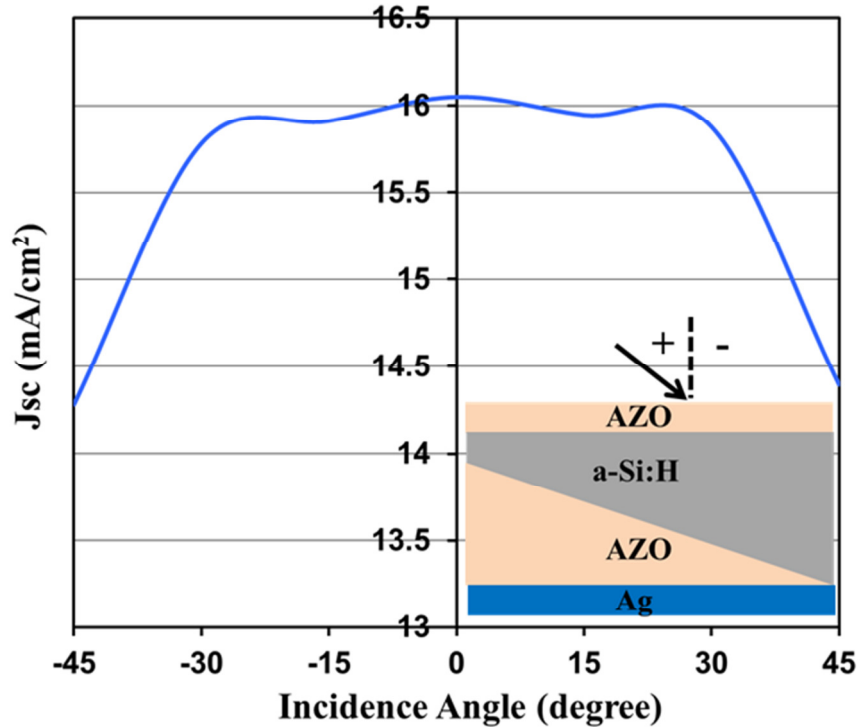


Figure 8.7. The calculated  $J_{sc}$  of the optimized design ( $L=650\text{nm}$ ,  $\alpha =35^\circ$ ,  $h_{eff}=277\text{nm}$ ) at varying angles of incidence. Inset is the schematic showing the definition of incident angles. We define positive and negative angles for light incident on the left side of the normal line and right side of the normal line, respectively.

### 8.5 2D Blazed Grating

We further improved the design by extending the 1D periodicity of the grating design to 2D periodicity. The schematic of the 2D grating design is shown in Figure 8.8a. Due to its geometry, the 2D grating design is expected to exhibit the same absorption for TE and TM polarization states. The 2D grating design has been called the “Rose” geometry by some

researchers [73]. We performed simulations for the 2D grating structure in which each wedge has the same dimensions as the wedges in the optimized 1D grating design. The absorption spectrum is shown in Figure 8.8b. The fabrication of this design, however, is questionable.

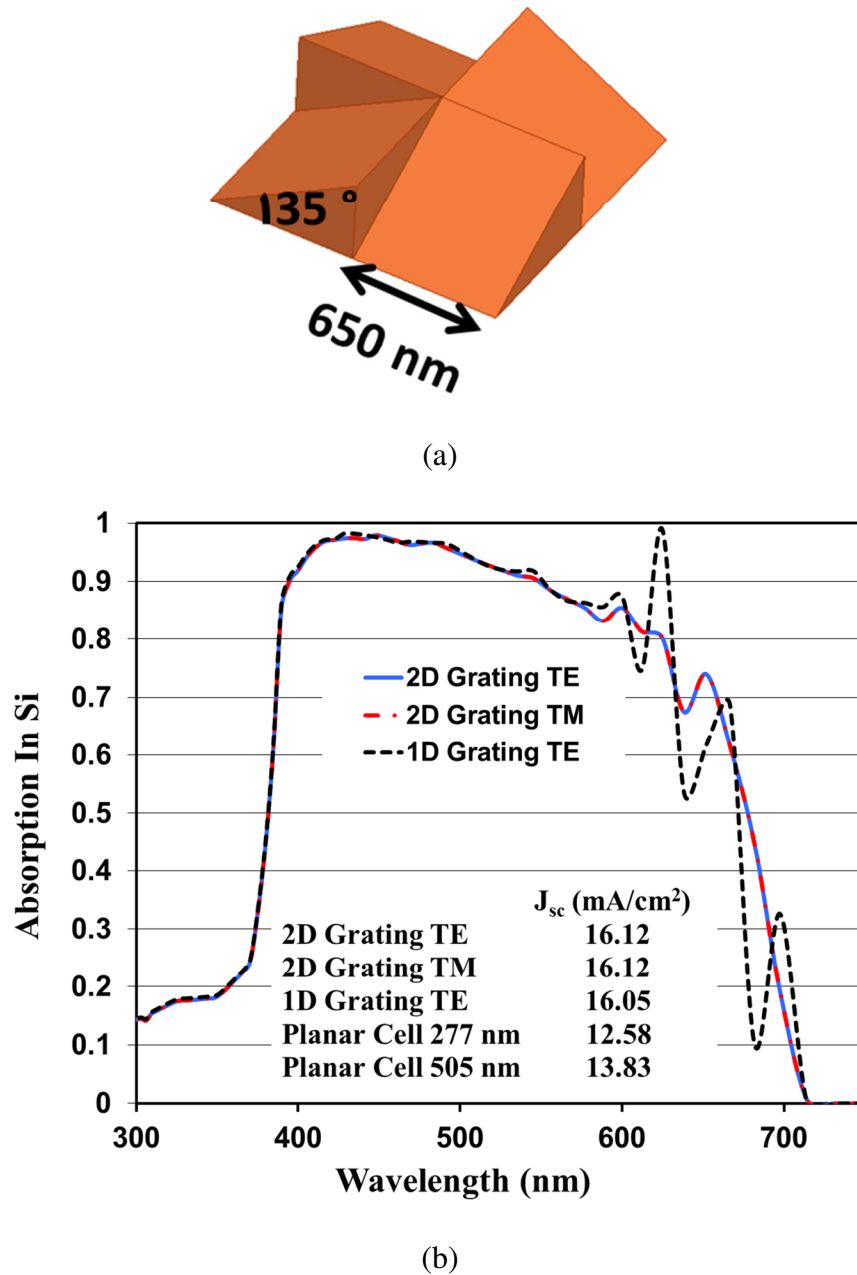


Figure 8.8. (a)The schematic of the optimized 2D grating design; (b)The absorption spectrum of the optimized 2D design compared to a planar cell with 322 nm a-Si:H.

Light absorption in the a-Si:H layer of the 2D grating integrated cell does not change when switching from TE polarization to TM polarization. The resulting  $J_{sc}$  of the cell with the 2D grating is  $16.12 \text{ mA/cm}^2$ , which is slightly higher (0.44%) than the cell with the 1D grating design at TE polarization. Instead of a drop in  $J_{sc}$  when switching from TE to TM polarization, the cell with the 2D grating design exhibits constant  $J_{sc}$  at both polarization states. The effective a-Si:H thickness of the cell with the 2D grating is 277 nm, which is the same as the cell with the 1D grating design. Compared to the planar cell with the same volume of a-Si:H, the 2D grating results in a 28.14% enhancement of  $J_{sc}$ .



## IX. Conclusions

In this dissertation, we proposed to use plasmonic and photonic approaches for light trapping designs in thin film solar cells. Light trapping in thin film solar cells requires a significant enhancement of light path within the active layers of solar cells while the physical thickness of semiconductor layers is limited. The key point is being able to manipulate incident light in a way that light can travel toward desired directions. Non-specular reflections (or transmissions) are desired. Existing light trapping designs include surface texturing, plasmonic designs and photonic designs. The disadvantages of existing designs include insufficient enhancement, undesired optical loss and undesired loss in carrier transport. A proper light trapping design should be able to enhance light absorption without hurting carrier transport in solar cells. We proposed the fishnet structure, the nanodome structure and the grating structure for advanced management of optical path within thin film solar cells.

- (1) The plasmonic fishnet structure is able to enhance short circuit current by over 13%. The fishnet structure was placed in the back end of a cell so that it does not degrade light absorption at short wavelengths. The resonance of fishnet is designed so that: 1) it resonates in the bandgap region of a-Si and 2) the resulting surface charge distribution on fishnet is able to radiate photons. Compared to plasmonic particles, it is a planar structure. The tuning of resonance frequency can be done without messing up with the thickness of transparent spacers. The resonance of fishnet is expected to shift when the solar cell is heated during operation. This conclusion derives from the study on microwave metamaterials that rely on very similar principles to excite resonances. Fishnet made of pre-trained shape memory alloys is expected to perform adaptive changes at different temperatures. The resulting plasmonic resonance will be very stable with respect

to temperature.

- (2) Light absorption can be enhanced by shaping solar cells into the nanodome structure. The nanodomains can be in the front end or back end of solar cells. Periodic dielectric cones or cylinders made of conductive materials were added in order to have additional scattering effects and improve carrier collection. Experimental results show that the domes, although come with additional volume of a-Si that might increase carrier recombination, do not result in a worse fill factor.
- (3) The periodic AZO grating structure has been able to enhance light absorption by over 20%. The grating structure was placed in the back end of solar cells. Light incident on the grating structure is reflected toward desired directions and hence result in more total internal reflections at the top surface of the absorber. Compared to nanodome and nanowire structures that might increase surface recombination due to the increased surface area, the increased surface area of the absorber by the optimized grating structure is less than 15%.

Future work will be focused on the further improvement of cell performance and a lower cost of fabrication. The work on improving cell performance will be focused on:

- (1) Reducing the loss due to light trapping designs. At first, a higher percentage of absorbed light should be within the active layer. A high total absorption associated with a high percentage of useful absorption within the active layer of a solar cell is very difficult to achieve in the wavelength region very close to the bandgap of semiconductor. Secondly, the negative impact from light trapping designs on carrier transport should be as small as possible.
- (2) Implementing broadband enhancement. The designs reported in this dissertation are all

wavelength dependent. A solar cell, however, is required to absorb photons over a broad spectrum as much as possible. Hence, light trapping designs are expected to enhance absorption over a broad spectrum instead of a narrow band.

(3) Designing structures that are cheap and fast to fabricate. So far, all the reported designs in this dissertation require high resolution electron beam lithography for fabrication. This process, although very accurate, is expensive and slow. Light trapping designs that accommodate cheap and fast process are necessary to meet the requirement for mass production and commercialization. The designs studied in this dissertation, however, can serve as prototypes. Future designs can be based on these prototypes but require less for the accuracy in fabrication.

## List of References

- [1] Mints, P. and Donnelly, J., “Photovoltaic Manufacturer Shipments, Capacity and Competitive Analysis 2010/2011,” Navigant Solar Services Program. Palo Alto, CA, 2011.
- [2] Goodrich, A., James, T. and Woodhouse, M., “Solar PV Manufacturing Cost Analysis: U.S. Competitiveness in a Global Industry,” available on NREL website: <http://www.nrel.gov/docs/fy12osti/53938.pdf>
- [3] Green, M. A., Emery, K., Hishikawa, Y. and Warta, W., “Solar cell efficiency tables (version 37),” *Prog. Photovolt: Res. Appl.*, vol. 19, 84-92, 2011.
- [4] Green, M. A., “Thin-film solar cells: review of materials, technologies and commercial status,” *J Mater Sci: Mater Electron*, vol. 18, S15-S19, 2007
- [5] Yang, L., Xuan, Y. and Tan, J., “Efficient optical absorption in thin-film solar cells,” *Opt. Express*, vol. 19, no. S5, A1165-A1174, 2011.
- [6] Schmela, M., Kruitmann, A., *Photon Int.*, vol. 4, 38, 2002.
- [7] NREL, Cadmium Use in Photovoltaics 2005, [www.nrel.gov/cdte/perspective.html](http://www.nrel.gov/cdte/perspective.html)
- [8] Schmela, M., *Photon Int. January issue*, vol. 1, 22–24, 2003.
- [9] Andersson, B.A., “Materials availability for large-scale thin-film photovoltaics,” *Prog. Photovoltaics*, vol. 13, 61–76, 2000.
- [10] “Tellurium” in “Mineral Commodity Summaries” by United States Geological Survey, 2008.
- [11] Tool, C.J.J., Burgers, A.R., Manshanden, P. and Weeber, A.W., “Effect Of Wafer Thickness On The Performance Of mc-Si Solar Cells,” *17th European Photovoltaic Solar Energy Conference*, Munich, 2001.
- [12] Ferlauto, A. S. *et. al.*, “Analytical model for the optical functions of amorphous semiconductors from the near-infrared to ultraviolet: Applications in thin film photovoltaics,” *J. Appl. Phys.*, vol. 92, no. 5, 2424-2436, 2002.
- [13] Lumerical FDTD Database <http://www.lumerical.com/>
- [14] Bandgap of Semiconductor Material, [http://en.wikipedia.org/wiki/Band\\_gap](http://en.wikipedia.org/wiki/Band_gap)
- [15] Pearce, J. M., Podraza, N. and Collins, R. W., Al-Jassim, M. M., Jones, K. M., Deng, J. and Wronski, C. R., “Optimization of open circuit voltage in amorphous silicon solar cells with mixed-phase (amorphous+nanocrystalline) p-type contacts of low nanocrystalline content,” *J. Appl. Phys.*, vol. 101, no. 114301, 2007.
- [16] Flewitt, A. J. and Milne, W. J., “Low-Temperature Deposition of Hydrogenated Amorphous Silicon in an Electron Cyclotron Resonance Reactor for Flexible Displays,” *Proceedings of the IEEE*, vol. 93, no. 7, 1364-1373, 2005.

- [17] Amorphous Silicon [http://en.wikipedia.org/wiki/Amorphous\\_silicon](http://en.wikipedia.org/wiki/Amorphous_silicon)
- [18] Rapaport, R., Lubianiker, Y., Balberg, I. and Fonseca, L., "Sensitization of the minority carrier lifetime in hydrogenated amorphous silicon," *Appl. Phys. Lett.*, vol. 72, 103-105, 1998.
- [19] Beaucarne, G., "Silicon Thin-Film Solar Cells," *Adv. OptoElectronics*, vol. 10, 1155-1166, 2007.
- [20] Fonash, S.J., "Solar cell device physics, 2nd ed.," Academic Press, 2010.
- [21] PV Education <http://www.pveducation.org/pvcdrom>
- [22] Yablonovitch, E., "Statistical Ray Optics," *J. Opt. Soc. Am.*, vol. 72, no. 7, pp. 899-907, 1982.
- [23] Yablonovitch, E. and Cody, G. D., "Intensity Enhancement in Textured Optical Sheets for Solar Cells," *IEEE. Trans. Electron Dev.*, vol. E-29, no. 2, 300-305, 1982.
- [24] Campbell, P. and Green, M. A., "High performance light trapping textures for monocrystalline silicon solar cells," *Solar Energy Materials & Solar Cells*, vol. 65, 369-375, 2001.
- [25] Papet, P., Nichiporuk, O., Kaminski, A., Rozier, Y., Kraiem, J., Lelievre, J. F., Chaumartin, A., Fave, A. and Lemiti, M., "Pyramidal texturing of silicon solar cell with TMAH chemical anisotropic etching," *Solar Energy Materials & Solar Cells*, vol. 90, 2319-2328, 2006.
- [26] Loffler, J., Groenen, R., Linden, J. L., van de Sanden, M. C. M., Schropp, R. E. I., "Amorphous silicon solar cells on natively textured ZnO grown by PECVD," *Thin Solid Films*, vol. 392, 315-319, 2001.
- [27] Zeman, M., van Swaaij, R. A. C. M. M., Metselaar, J. W. and Schropp, R. E. I., "Optical modeling of a-Si:H solar cells with rough interfaces: Effect of back contact and interface roughness," *J. Appl. Phys.*, vol. 88, no. 11, 6426-6443, 2000.
- [28] Groenen, R., Loffler, J., Sommeling, P.M., Linden, J. L., Hamers, E. A. G., Schropp, R. E. I. and van de Sanden, M.C.M., "Surface textured ZnO films for thin film solar cell applications by expanding thermal plasma CVD," *Thin Solid Films*, vol. 392, 226-230, 2001.
- [29] Haze factor <http://www.photonics.com/edu/Term.aspx?TermID=4520>
- [30] Asahi glass company  
[http://www.agc.com/english/csr/environment/products/positive\\_seihin1.html](http://www.agc.com/english/csr/environment/products/positive_seihin1.html)
- [31] Schaadt, D. M. and Yu, E. T., "Enhanced semiconductor optical absorption via surface plasmon excitation in metal nanoparticles," *Appl. Phys. Lett.*, vol. 86, no. 063106, 2005.
- [32] Nakayama, K., Tanabe, K. and Atwater, H. A., "Plasmonic nanoparticle enhanced light absorption in GaAs solar cells," *Appl. Phys. Lett.*, vol. 93, no. 121904, 2008.

- [33] Pillai, S., Catchpole, K. R., Trupke, T. and Green, M. A., "Surface plasmon enhanced silicon solar cells," *J. Appl. Phys.*, Vol. 101, no. 093105, 2007.
- [34] Hummel, R. E., "Electronic Properties of Materials, 3<sup>rd</sup> ed," Springer, 2000.
- [35] Johnson, P. B. and Christy, R. W. "Optical constants of the noble metals," *Phys. Rev. B*, vol. 6 4370-4379, 1972.
- [36] Sihvola, A., "Electromagnetic mixing formulas and applications," The Institution of Electrical Engineers, 1999.
- [37] <http://www.cerac.com/pubs/proddata/AZO.pdf>.
- [38] Schiff, E. A., "Thermodynamic limit to photonic-plasmonic light-trapping in thin films on metals," *J. Appl. Phys.*, vol. 110, no. 104501, 2011.
- [39] Zhu, J., Hsu, C. M., Yu, Z., Fan, S. and Cui, Y., "Nanodome Solar Cells with Efficient Light Management and Self-Cleaning," *Nano Lett.*, vol. 10, 1979-1984, 2010.
- [40] Nam, W. J., Ji, L., Benanti, T. L., Varadan, V. V., Wagner, S., Wang, Q., Nemeth, W., Neidich, D., and Fonash, S. J., "Incorporation of a light and carrier collection management nano-element array into superstrate a-Si:H solar cells," *Appl. Phys. Lett.*, vol. 99, no. 073113, 2011.
- [41] Garnett, E. C. and Yang, P., "Silicon Nanowire Radial p-n Junction Solar Cells," *J. Am. Chem. Soc.*, vol. 130, 9224-9225, 2008.
- [42] Kelzenberg, M. D., Boettcher, S. W., Petykiewicz, J. A., Turner-Evans, D. B., Putnam, M. C., Warren, E. L., Spurgeon, J. M., Briggs, R. M., Lewis, N. S. and Atwater, H. A., "Enhanced absorption and carrier collection in Si wire arrays for photovoltaic applications," *Nature Mater.*, vol. 9, 239-244, 2010.
- [43] Garnett, E. C., Peters, C., Brongersma, M., Cui, Y., McGehee, M. D., "Silicon nanowire hybrid photovoltaics," *35<sup>th</sup> IEEE Photovoltaic Specialists Conference*, Honolulu, HI, 2010.
- [44] Pozar, D. M., "Microwave Engineering, 3<sup>rd</sup> ed.," Wiley, 2004.
- [45] Krishnakumar, K. and Goldberg, D. E., "Control System Optimization Using Genetic Algorithms", *Journal of Guidance, Control and Dynamics*, Vol. 15, No. 3, 735-740, 1992.
- [46] Schaadt, D. M. and Yu, E. T., "Enhanced semiconductor optical absorption via surface plasmon excitation in metal nanoparticles," *Appl. Phys. Lett.*, vol. 86, no. 063106, 2005.
- [47] Ji, L. and Varadan V. V., "Fishnet Metastructure for Efficiency Enhancement of a Thin Film Solar Cell," *J. Appl. Phys.*, vol. 110, no. 043114, 2011.
- [48] Pillai, S., Catchpole, K. R., Trupke, T. and Green, M. A., "Surface plasmon enhanced silicon solar cells," *J. Appl. Phys.*, Vol. 101, no. 093105, 2007.
- [49] Jarvis, J. B., Janezic, M. D., Grosvenor, J. H., Jr, and Geyer, R. J., "Transmission/ reflection and short circuit line methods for measuring permittivity and permeability," *NIST, Boulder, CO, Tech. Note 1335-R*, 1993.

- [50] Pala, R. A., White, J., Barnard, E., Liu, J. and Brongersma, M. L., "Design of Plasmonic Thin-Film Solar Cells with Broadband Absorption Enhancements," *Adv. Mater.*, vol. 21, 3504-3509, 2009.
- [51] Sheng, P., Bloch, A. N. and Stepleman, R. S., "Wavelength-selective absorption enhancement in thin-film solar cells," *Appl. Phys. Lett.*, vol. 43, 579-581, 1983.
- [52] Mutitu, J. G., Shi, S., Chen, C., Creazzo, T., Barnett, A., Honsberg, C. and Prather, D. W., "Thin film solar cell design based on photonic crystal and diffractive grating structures," *Optics Express*, 16, 15238-15248, 2008.
- [53] Bermel, P., Luo, C., Zeng, L., Kimerling, L. C. and Joannopolous, J. D., "Improving thin-film crystalline silicon solar cell efficiencies with photonic crystals," *Optics Express*, vol. 15, 16986-17000, 2007.
- [54] Catrysse, P. B. and Fan, S., "Nanopatterned Metallic Films for Use As Transparent Conductive Electrodes in Optoelectronic Devices," *Nano Lett.*, vol. 10, 2944-2949, 2010.
- [55] Zhang, S. *et. al.*, "Near-infrared double negative metamaterials," *Opt. Express*, vol. 13, 4922-4930, 2005.
- [56] Valentine, J., Zhang, S., Zentgraf, T., Ulin-Avila, E., Genov, D.A., Bartal, G. and Zhang, X., "Three-dimensional optical metamaterial with a negative refractive index," *Nature*, vol. 455, 376-379, 2008.
- [57] Kafesaki, M. *et. al.*, "Left-handed metamaterials: The fishnet structure and its variations," *Phys. Rev. B*, vol. 75, no. 235114, 1-9, 2007.
- [58] Sondergaard, T. and Bozhevolnyi, S., "Slow-plasmon resonant nanostructures: Scattering and field enhancements," *Phys. Rev. B*, vol. 75, no. 073402, 1-4, 2007.
- [59] Landy, N. I., Sajuyigbe, S., Mock, J. J., Smith, D. R. and Padilla, W. J., "Perfect Metamaterial Absorber," *Phys. Rev. Lett.*, vol. 100, no. 207402, 1-4, 2008.
- [60] Varadan, V. V., and Tellakula, A. R., "Effective properties of split-ring resonator metamaterials using measured scattering parameters: effect of gap orientation," *J. Appl. Phys.*, vol. 100, no. 034910, 1-8, 2006.
- [61] Kim, I. K., and Varadan, V. V., "Electric and magnetic resonances in symmetric pairs of split ring resonators," *J. Appl. Phys.*, vol. 106, no. 074504, 2009.
- [62] Ghodgaonkar, D. K., Varadan, V. V., and Varadan, V. K., "Free-space measurement of complex permittivity and complex permeability of materials at microwave frequencies," *IEEE Trans. Instrum. Meas.*, vol. 39, no. 2, 387-394, 1990.
- [63] Varadan, V. V., Hollinger, R. D., Ghodgaonkar, D. K., and Varadan, V. K., "Free-space, broadband measurements of high-temperature, complex dielectric properties at microwave frequencies," *IEEE Trans. Instrum. Meas.*, vo. 40, no. 5, 842-846, 1991.

- [64] Varadan, V. V. and Ji, L., "Temperature dependence of resonances in metamaterials," *IEEE Trans. Microw. Theory Tech.*, vol. 58, no. 10, 2673-2681, 2010.
- [65] Pendry, J. B., Holden, A. J., Stewart, W. J., and Youngs, I., "Extremely low frequency plasmons in metallic mesostructures," *Phys. Rev. Lett.*, vol. 76, no. 25, 4773-4776, Jun. 1996.
- [66] Sheng, Z. and Varadan, V. V., "Tuning the effective properties of metamaterials by changing the substrate properties", *J. Appl. Phys.*, vol. 101, no. 014909, 2007.
- [67] Pendry, J. B., Holden, A. J., Robbins, D. J., and Stewart, W. J., "Magnetism from conductors and enhanced nonlinear phenomena," *IEEE Trans. Microw. Theory Tech.*, vol. 47, no. 11, 2075-2084, 1999.
- [68] Kafesaki, M., Koschny, T., Penciu, R. S., Gundogdu, T. F., Economou, E. N. and Soukoulis, C. M., "Left-handed metamaterials: detailed numerical studies of the transmission properties," *J. Opt. A: Pure Appl. Opt.*, vol. 7, S12-S22, 2002.
- [69] Imanaka, Y., "Multilayered Low Temperature Cofired Ceramics (LTCC) Technology", Springer, 2004.
- [70] Walker, C. A., Uribe, F., Monroe, S. L., Stephens, J. J., Goeke, R. S., and Hodges, V. C., "High-temperature joining of low temperature cofired ceramics," *Proceedings of the 3rd International Brazing and Soldering Conference*, 54-59, 2006.
- [71] Meier, J., Kroll, U., Vallat-Sauvain, E., Spitznagel, J., Graf, U., and Shah, A., "Amorphous solar cells, the micromorph concept and the role of VHF-GD deposition technique," *Sol. Energy*, vol. 77, 983-993, 2004.
- [72] Nam, W. J., Ji, L., Varadan, V. V. and Fonash, S. J., "Exploration of nano-element array architectures for substrate solar cells using an a-Si: H absorber" *J. Appl. Phys.*, vol. 111, no. 123103, 2012.
- [73] Gjessing, J., Sudbom A. S., and Marstein, E. S., "Comparison of periodic light-trapping structures in thin crystalline silicon solar cells," *J. Appl. Phys.*, Vol. 110, no. 033104, 1-8, 2011.
- [74] Heine, C. and Morf, R. H., "Submicrometer gratings for solar energy applications," *Appl. Opt.*, vol. 34, 2476-2482, 1995.
- [75] Chong, T. K., Wilson, J., Mokkaapati, S. and Catchpole. K. R., "Optimal wavelength scale diffraction gratings for light trapping in solar cells," *J. Opt.*, vol. 14, no. 024102, 1-9, 2012.
- [76] Madzharov, D., Dewan, R., and Knipp, D., "Influence of front and back grating on light trapping in microcrystalline thin-film silicon solar cells," *Opt. Express*, vol. 19 A95-A107, 2011.
- [77] Haase, C. and Stiebig, H., "Optical properties of thin-film silicon solar cells with grating couplers," *Prog. Photovolt: Res. Appl.*, vol. 14 629-641, 2006.
- [78] Lipson, A., Lipson, S. G. and Lipson, H., "Optical physics, 4<sup>th</sup> ed.," Cambridge University Press, 2011.



- [79] Chang, C. H., *et. al.*, “High fidelity blazed grating replication using nanoimprint lithography,” *J. Vac. Sci. Technol. B*, vol. 22 3260-3264, 2004.
- [80] Isabella, O., Campa, A., Heijna, M. C. R., Soppe, W., van Erven, R., Franken, R. H., Borg, H. and Zeman, M., “Diffraction gratings for light trapping in thin-film silicon solar cells,” *23rd European Photovoltaic Solar Energy Conference*, Valencia, Spain, 2008.
- [81] Patzig, C., Karabacak, T., Fuhrmann, B., and Rauschenbach, B., “Glancing angle sputter deposited nanostructures on rotating substrates: Experiments and simulations,” *J. Appl. Phys.*, vol. 104, no. 094318, 1-9, 2008.
- [82] Jellison, G. E. Jr., Modine, F. A., White, C. W., Wood, R. F. and Young, R. T. “Optical properties of heavily doped silicon between 1.5 and 4.1 eV,” *Phys. Rev. Lett.*, vol. 46 1414-1417, 1981.
- [83] Ji, L. and Varadan V. V., “Blazed Grating For Light Trapping In a-Si Thin Film Solar Cells,” *J. of Opt.*, vol. 14, no. 095001, 2012.

## Appendix

The content in this dissertation is in part from the following publications with reprint permissions from publishers.

© 2010 IEEE. Reprinted, with permission, from V. V. Varadan and L. Ji, Temperature Dependence of Resonances in Metamaterials, IEEE Transactions on Microwave Theory and Techniques, October 2010.

Reprinted with permission from L. Ji and V. V. Varadan, Journal of Applied Physics, Vol. 110, 043114, 2011. Copyright 2011, American Institute of Physics.

Reprinted with permission from W. J. Nam, L. Ji, T. L. Benanti, V. V. Varadan, S. Wagner, Q. Wang, W. Nemeth, D. Neidich, and S. J. Fonash, Applied Physics Letters, Vol. 99, 073113, 2011. Copyright 2011, American Institute of Physics.

Reprinted with permission from L. Ji and V. V. Varadan, Journal of Optics, Vol. 14, 095001, 2012. Copyright 2012, IOP Science.

Permission Letters are attached below:

### 1. IEEE Transactions on Microwave Theory and Techniques

Dear Liming:

Yes you may have permission to use the content of this paper for your dissertation as long as you reference the paper.

Sincerely,

Ms. Kim Tanger. Editorial Assistant

IEEE Transactions on Microwave Theory and Techniques Editorial Office

Ohio Aerospace Institute

22800 Cedar Point Road

Cleveland, Oh 44142

Phone: 440-962-3023

Fax: 440-962-3057

E-mail: TransactionsAssistant@oai.org

## 2. Journal of Applied Physics

Dear Dr. Ji:

Thank you for requesting permission to reproduce material from American Institute of Physics publications.

Permission is granted – subject to the conditions outlined below – for the following:

L. Ji and V. V. Varadan, "Fishnet metastructure for efficiency enhancement of a thin film solar cell," J. Appl. Phys. vol. 110, no. 043114, 2011.

To be used in the following manner:

Reproduced in your dissertation.

1. The American Institute of Physics grants you non-exclusive world rights in all languages and media.
2. This permission extends to all subsequent and future editions of the new work.
3. The following copyright notice must appear with the material (please fill in the information indicated by capital letters): "Reprinted with permission from [FULL CITATION]. Copyright [PUBLICATION YEAR], American Institute of Physics."

Full citation format is as follows: Author names, journal title, Vol. #, Page #, (Year of publication).

For an article, the copyright notice must be printed on the first page of the article or book chapter. For figures, photographs, covers, or tables, the notice may appear with the material, in a footnote, or in the reference list.

4. This permission does not apply to any materials credited to sources other than the copyright holder.

Please let us know if you have any questions.

Sincerely,

Susann Brailey

Manager, Rights and Permissions

American Institute of Physics

Suite 1NO1

2 Huntington Quadrangle

Melville, NY 11747-4502

Phone: 1-516-576-2268

Fax: 1-516-576-2450

Email: sbrailey@aip.org

### 3. Applied Physics Letters

Dear Dr. Ji:

Thank you for requesting permission to reproduce material from American Institute of Physics publications.

Permission is granted – subject to the conditions outlined below – for the following:

W. J. Nam, Ji, L., T. L. Benanti, V. V. Varadan, S. Wagner, Q. Wang, W. Nemeth, D. Neidich, and S. J. Fonash, “Incorporation of a light and carrier collection management nano-element array into superstrate a-Si:H solar cells,” Appl. Phys. Lett., vol. 99, no. 073113, 2011.

To be used in the following manner:

Reproduced in your dissertation.

1. The American Institute of Physics grants you non-exclusive world rights in all languages and media.
2. This permission extends to all subsequent and future editions of the new work.
3. The following copyright notice must appear with the material (please fill in the information indicated by capital letters): "Reprinted with permission from [FULL CITATION]. Copyright [PUBLICATION YEAR], American Institute of Physics."

Full citation format is as follows: Author names, journal title, Vol. #, Page #, (Year of publication).

For an article, the copyright notice must be printed on the first page of the article or book chapter. For figures, photographs, covers, or tables, the notice may appear with the material, in a footnote, or in the reference list.

4. This permission does not apply to any materials credited to sources other than the copyright holder.

Please let us know if you have any questions.

Sincerely,

Susann Brailey

Manager, Rights and Permissions

American Institute of Physics

Suite 1NO1

2 Huntington Quadrangle

Melville, NY 11747-4502

Phone: 1-516-576-2268

Fax: 1-516-576-2450

Email: [sbrailey@aip.org](mailto:sbrailey@aip.org)